ISBN 978-82-326-1098-3 (printed version)
ISBN 978-82-326-1099-0 (electronic version)
ISSN 1503-8181

Andrey Volynkin

Doctoral Thesis

Doctoral theses at NTNU, 2015:221

Andrey Volynkin

The role of carbon supports in platinum catalyzed hydrogenation/dehydrogenation model reactions

NTNU
Norwegian University of
Science and Technology
Faculty of Natural
Sciences and Technology
Department of Chemical Engineering

Doctoral theses at NTNU, 2015:221

NTNU

NTNU – Trondheim
Norwegian University of
Science and Technology

NTNU – Trondheim
Norwegian University of
Science and Technology

Andrey Volynkin

The role of carbon supports in platinum catalyzed hydrogenation/ dehydrogenation model reactions

Thesis for the degree of Philosophiae Doctor

Trondheim, September 2015

Norwegian University of Science and Technology

NTNU – Trondheim
Norwegian University of
Science and Technology

NTNU
Norwegian University of Science and Technology

Thesis for the degree of Philosophiae Doctor

ISBN 978-82-326-1098-3 (printed version)
ISBN 978-82-326-1099-0 (electronic version)
ISSN 1503-8181

Doctoral theses at NTNU, 2015:221

Printed by Skipnes Kommunikasjon as

Acknowledgements

First and foremost, I am very grateful to my main supervisor, Professor Edd A. Blekkan and my co-supervisor, Professor Magnus Rønning for giving me opportunity to work at Norwegian University of Science and Technology (NTNU), Department of Chemical Engineering. I would like to express my gratitude and sincere appreciation for their guidance, assistance, and encouragement throughout my PhD studies.

I thank all the members of the Catalysis group and SINTEF for a nice working environment and for giving me inspiration. It has been a pleasure to be a part of Department of Chemical Engineering.

This work would not be possible without help from my friends and colleges, especially, Navaneethan Muthuswamy, Ilya Gorelkin, Eirik Østbye Pedersen, Alexey Voronov, P. V. Daham S. Gunawardana, Nikolaos E. Tsakoumis, and Nicla Vicinanza, and I am very grateful for their help and support.

My special thanks go to Department of Chemical Engineering executive officer Lisbeth Roel for help concerning paperwork and access, department engineers Harry Brun for help concerning gases and gas detectors, Arne Fossum for ordering chemicals, Karin Dragsten and May Grete Sætran for help with various instruments, workshop engineers Jan Morten and Odd Hovin and glass workshop engineer Astrid Salvesen for helping me with catalytic rigs and reactors.

I am grateful to Dr. James McGregor and members of Department of Chemical Engineering and Biotechnology at Cambridge University, especially Dr. Liam McMillan and Professor Lynn Gladden for valuable discussion concerning my

work, assistance and for giving me opportunity to work at University of Cambridge during my stay in UK from October 2012 to April 2013.

The financial support from the Research Council of Norway through The Gas Technology Centre NTNU- SINTEF (GTS) is gratefully acknowledged.

Finally and most importantly, I would like to thank my wife, parents, and parents in law for their immense support, understanding and patience.

Abstract

The diversity of carbon materials provides many opportunities for the use of those materials in catalysis, including as support materials for metal catalysts. However, this diversity of carbon structures and properties also introduces a challenge, as different carbon supports can influence the catalytic properties in ways that can be difficult to predict.

In this thesis, five carbon materials with different structure and properties, carbon black, multiwalled carbon nanotubes, platelet carbon nanofibers, conical platelet carbon nanofibers, and graphite, have been characterized and used as support for platinum nanoparticles produced by the polyol method. The relation between the carbon structure and the dispersion of platinum has been investigated and the effect of carbon on the catalytic properties of platinum has been studied with two model reactions, dehydrogenation of propane and hydrogenation of ethene.

The results show that transmission electron microscopy (TEM) and CO stripping by cyclic voltammetry (CV) gave consistent values for platinum dispersion for platinum catalysts supported by carbon nanofibers and carbon nanotubes. There were some discrepancies between the techniques for Pt/graphite and Pt/carbon black, possibly due to issues with mass transfer limitations, the particle size distributions, and TEM resolution. The results from the hydrogenation of ethene were consistent with the results from TEM and CV.

It was found that the metal dispersion is important, but not the only parameter influencing the catalytic activity of carbon-supported catalysts. In catalytic dehydrogenation of propane, the Pt supported on carbon black showed a higher conversion and turnover frequency (TOF) value than catalysts prepared using carbon nanofibers, carbon nanotubes, and graphite as support. In addition to

giving a higher turnover frequency, the propane dehydrogenation reaction over Pt supported on carbon black was less susceptible to deactivation in experiments without co-fed hydrogen, indicating that the carbon black support either reduces the rate of coke formation or the toxicity of the coke formed.

This high conversion observed for Pt supported on carbon black when used for propane dehydrogenation has not been observed when structure insensitive ethene hydrogenation was used as a model reaction, confirming that the high conversion and longer lifetime compared to other tested catalysts was not caused by a higher dispersion. It is suggested that other effects, such as metal-support interaction, can play an important role in influencing the properties of carbon-supported catalysts.

List of publications and presentations

Journal paper:

- Andrey Volynkin, Magnus Rønning, Edd Anders Blekkan, "The role of carbon support for propane dehydrogenation over platinum catalysts" Accepted for publication in Topics in Catalysis.

Additional papers, not included in the thesis:

- Morten Bjørgen, Anlaug Haukvik Grave, Saepurahman, Andrey Volynkin, Karina Mathisen, Karl Petter Lillerud, Unni Olsbye, Stian Svelle, "Spectroscopic and catalytic characterization of extra large pore zeotype H-ITQ-33", 2012. Microporous and Mesoporous Materials, Vol. 151, (Issue 15), pp.424–433

Presentations:

- Andrey Volynkin: Propane dehydrogenation over carbon-supported Pt catalysts, Presentation, 16th Nordic Symposium on Catalysis, Oslo 15-17th June 2014

- Andrey Volynkin: Propane dehydrogenation over carbon-supported Pt catalysts, Presentation, NKS Catalysis symposium, Trondheim 3th December 2013

List of symbols and abbreviations

Abbreviations	Description
AC	Activated carbon
BET	Brunauer-Emmet-Teller (method)
BJH	Barrett-Joyner-Halenda (method)
C/H	Carbon/hydrogen
CB	Carbon black
CPCNF	Conical platelet carbon nanofiber
CNF	Carbon nanofiber
CNT	Carbon nanotube
CVD	Chemical vapor deposition
DRIFTS	Diffuse reflectance infrared Fourier transform spectroscopy
EB	Ethylbenzene
EG	Ethylene glycol
FBCNF	Fishbone carbon nanofiber
FT-IR	Fourier transform infrared
ICP-MS	Inductively coupled plasma mass spectrometry
IEP	Isoelectric point
MD	Molecular dynamics
MFC	Mass flow controller
MOR	Methanol oxidation reaction
MSI	Metal-support interaction
MWCNT	Multiwalled carbon nanotube
ODH	Oxidative dehydrogenation
ORR	Oxygen reduction reaction
PGM	Platinum group metals
PlCNF	Platelet carbon nanofiber
PM	Pressure meter
RHE	Reversible hydrogen electrode
SCA	Synthetic carbon allotropes
SD	Standard deviation

SHE	Standard hydrogen electrode
SE	Scattered electrons
SEM	Scanning electron microscopy
SMSI	Strong metal-support interaction
SV	Safety (pressure release) valve
SWCNT	Single-walled carbon nanotube
TCD	Thermal conductivity detector
TG	Thermogravimetry
TGA	Thermogravimetric analysis
TOS	Time on stream
TEM	Transmission electron microscopy

Symbol (Greek alphabet)	**Description**	**Unit**
v_{CH_4}	Methane outlet flow	ml/min
$v_{C_2H_4}$	Ethene outlet flow	ml/min
$v_{C_2H_6}$	Ethane outlet flow	ml/min
$v_{C_3H_6}$	Propene outlet flow	ml/min
$v_{C_3H_{8\_in}}$	Propane inlet flow	ml/min
$v_{C_3H_{8\_out}}$	Propane outlet flow	ml/min
v_{i_out}	Outlet flow of component i	ml/min
ρ_{Pt}	Atom density on the Pt surface	atoms/cm^2
χ	Conversion	%

Symbol (latin alphabet)	**Description**	**Unit**
a	Carbon selectivity factor, 1/3 for CH_4, 2/3 for C_2H_4 and C_2H_6, and 1 for C_3H_6	-
A_{Pt}	Area of one platinum atom, 8.06×10^{-16}	cm^2/atom
CBN	Carbon balance number	%
d_m	Particle size of the catalytic metal (platinum)	nm
$Disp$	Dispersion of platinum (fraction)	-
m_{Cat}	Catalyst mass	gram

M_{Pt}	Molar mass of platinum, 195.08	gram/mol
N_A	Avogadro`s number	-
$N_{activePt}$	Number of surface Pt-atoms	-
$Q_{CO\_oxidation}$	Stripping area (current × potential) from CO stripping	volt×ampere
$Q_{CO\_stripping\_total}$	Total stripping area (current × potential)	volt×ampere
$Q_{Pt\_oxidation}$	Stripping area (current × potential) from Platinum oxidation and reduction	volt×ampere
$Q_{CO\_adsorp\_initial}$	Stripping area (current × potential) from CO stripping of initially adsorbed CO	volt×ampere
Q	CO monolayer stripping charge, 0.420	mC/cm^2
P	Pressure	atm
R	Stripping scan rate	volt/second
$R_{C_3H_6mol}$	Molar propene production rate	$mol/(g_{cat}\times s)$
$R_{C_3H_8mol}$	Molar propane consumption rate	$mol/(g_{cat}\times s)$
S_{CO}	Platinum surface area available for CO adsorption	cm^2
S_i	Carbon based selectivity	%
T	Temperature	°C
$T_{m(1/2)}$	Temperature for gasification of 50% of the sample	°C
TOF	Turnover frequency	s^{-1}
V_{mol}	Molar volume at 20 °C and 1 atm, 24044	ml/mol
V_{Pt}	Pt atom volume, 1.51×10^{-23}	cm^3/atom
X_{Pt}	Catalyst loading (fraction)	-

Table of Contents

1. Introduction

1.1 Carbon materials

The diversity of carbon materials is impressive, almost one thousand different carbon materials are known [1] and it is likely that many more are to be discovered. Carbon materials show a wide range of interesting mechanical, electrical, optical, and other properties. Therefore, they are very promising structural and functional materials for future applications. The reason for this diversity of carbon materials is the ability of carbon to form stable sp^2 and sp^3 hybridized structures. Although syntheses of stable sp materials, such as carbyne, consisting of linear acetylenic carbon have been reported [2] they are beyond the scope of this discussion. Some of the sp^2 and sp^3 structures of synthetic carbon allotropes (SCA) are presented in Figure 1.1. They can have different degrees of order on nano-, meso-, and macro-level and contain different defects. The name "allotrope", meaning a structural modification of a single element, should be used with care as a majority of carbon materials do not have a defined structure, but instead have a complex and insufficiently described composition [3]. In addition, the highly diverse world of the carbon materials is further complicated by the presence of heteroatoms and other impurities, which further expand the range of their chemical and physical properties.

There is no universal classification that can be applied to the whole range of carbon materials. The carbon materials that can be related to graphite by being composed of graphene layers can be classified by the orientation of those layers, as shown in Figure 1.2. This classification is frequently applied for nanostructured carbons such as carbon nanofibers (CNFs) and carbon nanotubes (CNTs). By this classification, we can distinguish single and multiwalled CNTs

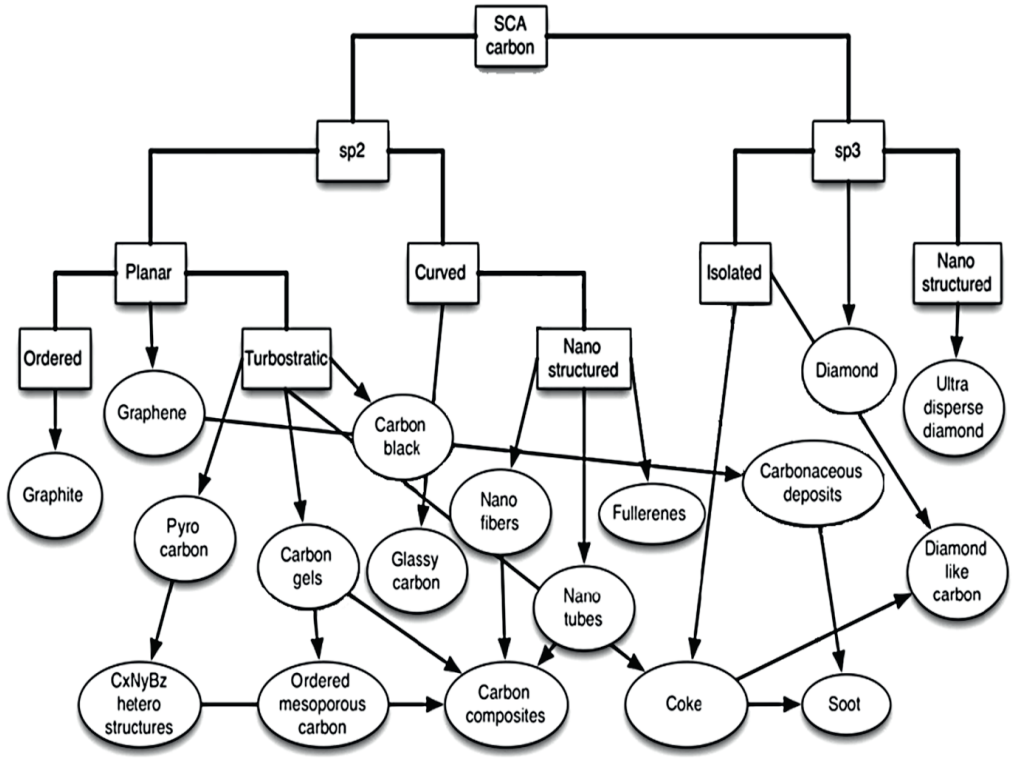

Figure 1.1 Some of the properties of carbon structures are presented in rectangular boxes, and families of carbon structures are presented in ovals [3].

as consisting of one or many tubular graphene layers with their surfaces parallel to each other and to the tube direction. Likewise we have different CNFs with graphene surfaces stacked in perpendicularly to the fiber direction as in platelet fibers or are tilted at a sharp angle relative to the fiber direction as in fishbone (also known as herringbone) or stacked cone fibers [4]. Some of the fibers can have a hollow space inside. Other kinds of CNFs can similarly be described by this classification, for example, ribbon and cone-helix nanofibers [5]. However, this classification cannot be extended to describe more complex carbon structures [1].

Some of the first transmission electron microscopy (TEM) evidence of the carbon nanotubes was presented in 1952 by Radushkevich et al. [6; 7]. They have reported that carbon produced by a thermal decomposition of CO on iron powder contains seemingly hollow wormlike structures with iron carbide particles on their tips. At that time, the discovery did not make an impact on the scientific literature. The research community gained interest in multiwalled carbon nanotubes (MWCNTs) and their potential applications in 1991 when Iijima reported the observation of tubular carbon structures [8]. This publication was readily discussed, as it was only six years after another new allotrope of carbon, spherical fullerenes, was discovered. In 1993, the discovery of single-walled carbon nanotubes (SWCNTs) was reported by Iijima and Ichihashi [9], and independently by Bethuene et al. [10]. This has reasserted nanostructured carbon materials as a hot topic in the scientific community ever since.

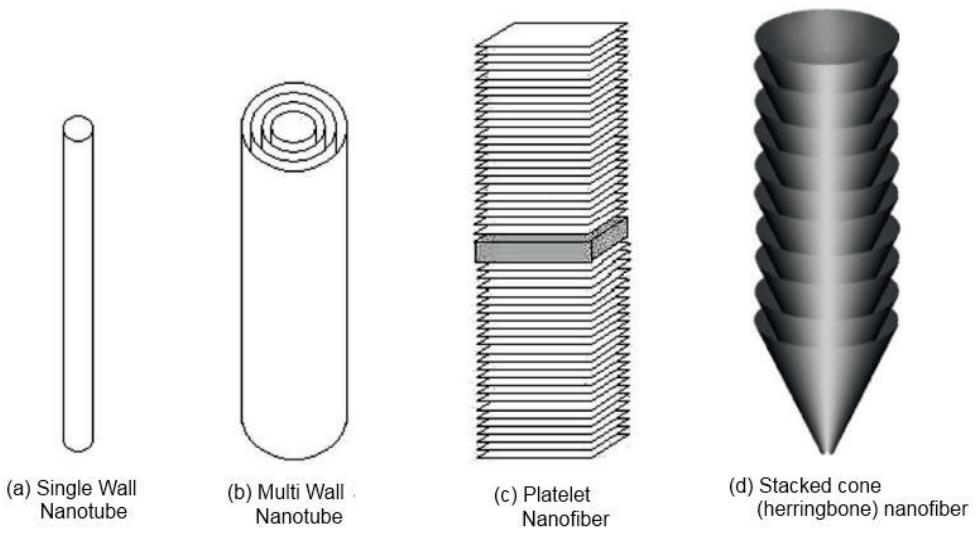

Figure 1.2 Examples of the common carbon nanofilament structures [11; 12].

In contrast to CNTs, other types of filamentous carbon have been well known before the 20th century. Already in 1889 a process of forming carbon filaments

by thermal decomposition of hydrocarbons was patented [13]. Filamentous carbons have also been known for many years as undesired byproducts in the catalytic steam reforming and methanization processes. The formation mechanism of those fibers has been described in order to understand and limit the carbon fiber formation because it can lead to the deactivation of the catalysts by disintegration and occlusion of catalytic metal by carbon. Formation of the carbon fibers can even lead to rupturing of the reactor walls [14]. However, as with CNTs, the discovery of nanostructured carbon fibers was not possible before the transmission electron microscope (TEM) became readily available. One of the first studies of the microstructure of CNFs has been published by Hillert and Lange in 1959 [15].

The carbon nanomaterials can be produced using several different methods including arc discharge, laser ablation, and chemical vapor deposition. While the first MWCNTs were produced using the arc discharge, this method today together with laser ablation of graphite is more commonly used to produce SWCNTs, and the latter method has allowed mass production of MWCNTs and CNFs [16]. A simplified model for the catalytic formation of CNFs and CNTs by the catalytic chemical vapor deposition (CVD) involves dissociation of the carbon-containing gas at the catalyst metal surface, followed by either dissolution of carbon into the bulk of the metal particle and diffusion of carbon trough the metal or by carbon diffusion along the surface of the particle. Then the carbon is precipitated as graphitic layers on another surface of that particle [17; 18; 19; 20]. The structure of CNFs and CNTs is strongly dependent on growth catalyst properties (catalytic metal or metals, metal dispersion, catalyst support, etc.), carbon source (CO, CH_4, C_2H_6, etc.) and reaction conditions (H_2/hydrocarbon ratio, temperature, and pressure).

The marked for the carbon nanomaterials has grown dramatically for the last few years, and it is expected to grow further as the carbon nanomaterials find new applications, and the mass production pushes the price down. Per 2011 the MWCNTs were the most important nanomaterials, accounting for 28% of the market share of the overall nanomaterial demand, with plastics and composite producers being the largest CNT consumers [21]. Applications of nanostructured carbons are becoming more numerous but are still in their infancy and often limited by the high cost of high-quality materials. As new high-quality nanostructured materials will become more available, future applications might utilize advanced properties of those materials for more specialized uses such as in the electronic industry, energy storage, and photovoltaic cells [21]. This can impact the use of nanostructured carbons in catalysis and possibly lead to the first large-scale commercial use of catalysts based on nanostructured carbons.

For applications in catalysis, the carbon materials are interesting both as catalyst supports and catalysts on their own. At the same time, it is important to minimize the formation of catalyst deactivating carbons when dealing with carbon-containing reactants and products. Carbon formed as a byproduct is usually described by the word “coke”. However, there are many different carbon materials with different C/H ratios that can be described with this term [22]. Deactivation of catalysts by coking is one of the most important technological and economic problems in the petrochemical industry. Usual countermeasures against the coke formation in gas phase reactions are an application of a more coke resistant catalyst and changing reaction conditions (temperature, hydrogen or steam partial pressure, etc.). When the catalyst activity becomes unacceptably low, the catalyst is often regenerated by coke combustion. A coke resistant catalyst can still have high activity of coke formation, but this coke does not have a detrimental effect on the activity.

Some carbon materials, such as active carbons, have been used commercially as catalyst supports for decades due to their high surface area, low cost of production, stability at non-oxidizing conditions in both acidic and basic media, possibility of tuning the graphitic structure and hydrophobicity by adding functional groups [23], and easy recovery of the supported metals by support combustion. In addition, the electrical conductivity of carbons is important for electrocatalysis, for example, when carbons are used as electrode materials. Nevertheless, active carbons are mainly derived from natural sources and are not designed to have a specific structure at nano-level. Therefore, those materials do not offer the same possibilities as CNTs and CNFs. The potential advantages given by use of nanostructured materials in catalysis as compared to other types of carbon materials are summarized by Ampelli et al. [23]. Some of those advantages are:

- Better control over micro- and mesoporosity. Mesoporosity in CNTs and CNFs is primarily voids between tubes or fibers, while microporosity is associated with fiber or tube structure. Most CNTs and CNFs do not have any significant amount of micropores and this can be an advantage as it gives improved diffusion and gives better utilization of the catalyst.
- Nanostructured carbons can have more uniform characteristics than carbons produced from a natural feedstock (nutshells, peat, etc.).
- Nanostructured carbons can be produced with fewer structural defects, or controlled types and densities of defects.
- Nanostructured carbons are usually more resistant to oxidizing conditions than activated carbons.
- Better electron and heat transport.
- Possibility to utilize effects caused by the surface curvature of CNTs for making the active sites more effective.

- Possibility for nano-engineering of catalytic sites.

1.2 Functionalization of and metal loading on carbon supports

Carbon materials produced by the CVD method usually contain remains of growth catalyst. Those remains can still be catalytically active and sometimes they have to be removed. This is commonly done using acid treatment, for example with hydrochloric acid (HCl) [24] or oxidizing acids as nitric acid (HNO_3) [3; 24; 25; 26; 27]. The treatment with HCl does not significantly damage the carbon structure while the treatments with oxidizing acids will introduce oxygen-containing functional groups and severe treatments with those acids can damage the carbon structure. Both methods can be done with different acid concentrations, different temperatures, and different time periods. In some cases to remove growth catalyst metal is not sufficient, and growth catalyst support has to be removed as well. For this purpose the carbon material can be treated with hydrofluoric acid (HF) [28]. However, this procedure is not commonly practiced due to technical and safety issues regarding work with this acid [29]. Some authors have reported removal of growth catalyst with sodium hydroxide (NaOH) [24; 30] or potassium hydroxide (KOH) [25] solution. In recent years, reports of meticulous purification of the carbon supports became less frequent, due to more availability of carbon materials with high purity. This can be explained by developments in CVD synthesis techniques, giving a higher yield of carbon materials for each gram of growth catalyst. In addition, many commercial carbon material producers do their own purification before selling their product.

Often, but not always [30; 31; 32], the carbon supports are functionalized before deposition of catalytic metal. Functionalization is an introduction of heteroatoms, or groups containing heteroatoms to the carbon structure. This can

be done during production, such as doping of CNFs and CNTs [33; 34], or by secondary treatments by large number of different methods. The introduced heteroatoms can change hydrophobic, electronic or other properties, anchor metal nano-particles or even be catalytically active by themselves [26; 35; 36]. One of the most common procedures for the carbon functionalization is the introduction of the oxygen-containing groups by an oxidative treatment, for example with an oxidizing acid. Such treatments can sometimes replace or supplement the purification treatment [27]. In addition to removal of growth catalyst, the oxidative treatments can remove amorphous carbon impurities because of their higher susceptibility to oxidation. However, other methods to remove amorphous carbon, such as ultrasonic treatment followed by washing with a NaOH solution and Soxhlet extraction, can in some cases be more effective and gentle to the carbon surface structure [37].

The oxidative treatments can damage the carbon structure, and such treatments can be used to open CNT ends and make the hollow space and internal surface accessible. Other functionalization methods include solvent impregnation followed by melt-coat treatment with sulfur [38], incipient wetness impregnation with phosphoric oxide [39], treatment with ethanolamine [34], and many more. Besides introducing anchoring sites for catalytic particles, oxidative treatments can also make carbon surface more hydrophilic and improve support behavior towards wetting with aquatic solutions [40]. This is important both for the preparation of catalysts when the metal precursor is in an aquatic solution and for the use of the catalyst in liquid-phase reactions.

Deposition of catalytic metal on carbon supports can be done by different methods such as incipient wetness impregnation [31; 41], metal-oxide colloid method [32; 42], homogeneous deposition precipitation [42], electrochemical deposition [43], and ion exchange [25]. In addition, there are a long range of

different methods where compounds containing a precursor of catalytic metal (e.g. H_2PtCl_6 or Na_2PdCl_4) are reduced by a reducing agent (paraformaldehyde, sodium borohydride, ethylene glycol, hydrogen, formaldehyde, etc.) to produce metal nanoparticles (colloids) in a solution [24; 44; 45; 46], that can be deposited on the support. There are also some techniques that do not require a liquid phase such as thermal evaporation and deposition of catalytic metal [47], atomic layer deposition [48], and sputtering deposition [49]. It is important to choose the right metal deposition method by considering properties of the carbon support. The functionalization of carbon supports by introducing oxygen-containing groups can have a negative effect on the metal dispersion if there are unfavorable electrostatic interactions between the surface of the supports and metal precursor during preparation of carbon-supported catalyst [46].

When the carbon-supported catalysts are prepared by the use of a platinum precursor in a solvent, the following factors should be considered [50]:

- Polarity of the solvent
- The pH of the solution
- Cationic or anionic charge of the metal precursor
- Surface charge of the carbon support in the solution

Those factors can be dependent on each other, for example, a change of pH can affect the charge of both the metal precursor and the carbon support surface.

It is important to avoid the electrostatic repulsion between the catalyst support and the metal precursor. Therefore, the cationic precursors such as $Pt(NH_3)_4^{2+}$ should be deposited on negatively charged surfaces in basic media. On the other hand, the anionic precursors such as $PtCl_6^{2-}$ should be deposited in an acidic solution on positively charged surfaces [50]. In other words, when the anionic precursors are used, to remove the net negative electric charge of the support

and the resulting repulsion between the support and the negatively charged metal precursor, the pH of the solution has to be lowered [51]. Control of the pH is especially important if the carbon surface is functionalized with groups that can be protonated. The oxidative treatments of carbon can lead to a formation of acidic functional groups, and this lowers the isoelectric point (IEP) of the carbon support, i.e. the pH value at which the support carries no net electrical charge [24; 52].

The polarity of the solvent is important, as a good solvent-support interaction is necessary for an effective deposition of the active metal on the support. Therefore, hydrophilic functional groups on oxidized carbon supports are advantageous when a polar solvent, such as water, is used [53].

However, the high dispersion of the metal catalyst on a functionalized carbon support does not necessarily lead to high dispersion when the catalyst is applied. Oxygen-containing functional groups can be removed by heating in an inert or reducing atmosphere. Since most common catalyst preparation procedures involve catalyst reduction with H_2 at elevated temperatures, this will reduce the amount of surface functional groups and can lead to a completely different metal distribution on the surface of the support [53; 54]. This can be explained by proposing that metal-carbon interaction occurs on π-sites when other anchoring sites are not available. Hydrogen treatment removes the most unstable oxygen surface groups; however, the most stable surface groups will remain. Their density or anchoring ability may not be sufficient to anchor the metal particles, and the electron withdrawing groups will affect the electron delocalization in the π-sites and hence weakening metal-support interaction [53; 54; 55]. This can in turn cause sintering of the metal particles.

1.3 Platinum as catalyst

Platinum has a remarkable resistance to corrosion, being one of the least reactive metals. Yet its catalytic properties were known since the 19th century [56]. Today platinum is the preferred catalyst in catalytic converters in automobiles, which is the most important marked for platinum [57]. This metal is also commonly used as catalyst in e.g. hydrogenation, dehydrogenation, isomerization, and oxidation reactions. Platinum is not an abundant metal, with only about 0.005 ppm present in the earth's crust [58]. This makes it expensive and the research on less expensive and more abundant catalysts to replace platinum in the most critical applications is ongoing. However, so far metal-free alternatives to platinum are many years away from large-scale commercialization [59]. Therefore, it is important to maximize the efficiency of the applications of platinum to reduce the loss of this precious metal and recycle it whenever possible.

Any heterogeneous catalytic reaction requires adsorption of the reactant on the catalyst surface. The interaction between the reactant and the catalyst should not be too weak or too strong. Too weak interaction will cause desorption of the reactant before a reaction can occur, while too strong interaction will poison the catalyst. This is known as the Sabatier principle. Many transition metals have an ability to interact with reactants, such as hydrocarbons or hydrogen, "just right", catalyzing a chemical reaction. The origin of this interaction can be described by the d-band model which has been confirmed by experiments [60]. Shortly, the s- and d-orbitals in each metal atom overlap due to the metallic bonding and become s- and d-bands on the metal surface. In transition metals, the d-band is partially filled and, therefore, can accept electrons from the valence levels of adsorbates. If the anti-bonding level is not filled while there are electrons in the bonding level, then a chemical bond is created. The difference between metals

or even different crystallographic surfaces of the same metal is explained not only by the number of electrons, but also by the width of the d-band and its center. A high d-band center will give fewer elections in the anti-bonding orbitals and, therefore, stronger bonds. Platinum is one of those metals having the right electronic structure to catalyze a long range of chemical reactions. However, platinum's electronic structure is dependent on many factors, including the crystallographic structure of the metal surface, interaction with other elements or interaction with the catalyst support. Therefore, platinum's catalytic properties can be modified to better suit the different catalytic processes.

1.4 Metal interaction with carbon supports

The main purpose of the catalyst support is to provide a high dispersion of metal particles to maximize the metal surface area that can come in contact with the reactants and hence use the active metal effectively [61]. In addition, the catalyst support should have some metal-support interaction (MSI) when the catalyst is applied at high temperatures to make the metal particles less mobile on the support surface and prevent sintering [62]. For example, a study by Ratkovic et al. [63] of Fe/Al_2O_3 and $Fe\text{-}Ni/Al_2O_3$ catalysts for CNT production has reported that a stronger MSI in the bimetallic catalyst prevents sintering and deactivation of the catalyst during carbon deposition. On the other hand, if the metal-support interaction is too strong, then this can cause too weak interaction between the catalytic metal and the reactants leading to a low catalytic activity. For example, strong metal-support interaction (SMSI) has been described by Tauster et al. [64] for platinum group metals (PGM) on TiO_2 supports. After the reduction at 500 °C, the interaction between PGMs and TiO_2 has become so strong that the metal's ability to chemisorb hydrogen or carbon monoxide was

significantly reduced or even vanished entirely. This phenomenon is not exclusive for TiO_2 and has later been observed with other supports such as Nb_2O_5 [65] and CeO_2 [66].

The metal-support interaction plays an important role also when carbon is used as a catalyst support. One of the early studies of CNFs as catalyst support by Rodrigues et al. [67] have shown that Fe-Cu particles supported on CNFs are more active for the catalytic hydrogenation of ethene than Fe-Cu supported on active carbon or on γ-alumina. It was proposed that strong metal-support interaction, causing an exposure of more favorable crystallographic surface faces of the metal or a metal-support electron transfer, changing the metals interaction with gas. A study by Planeix et al. [68] has also attributed better selectivity for cinnamaldehyde hydrogenation over Ru/CNT catalyst, as compared to Ru/Al_2O_3 to the metal-support interaction. This metal-carbon interaction was reported to be "of a different kind" compared to metal alumina interaction. However, no details were given.

The large variety of different carbon support materials with different properties makes them suitable for studying the effects of the metal-support interaction. The metal-support interaction between transition metal clusters and carbon supports is dependent on several factors including the type of the metal, the cluster size and orientation of the cluster, graphitization degree, the presence of heteroatoms or other defects, and orientation of the graphite planes.

An example of the effect of metal type on the metal-support interaction was found by a theoretical molecular dynamics (MD) simulation by Sanz-Navarro et al. [69]. Their calculation have shown that the curvature of the fishbone carbon nanofiber support does not influence on the d-band and, therefore, catalytic

properties of the Pt_{100} clusters, while a significant influence on the Ni_{100} clusters can be expected. This is a result of a difference in metal-metal binding energy, nickel clusters get more deformed than platinum clusters when adsorbed on carbon supports, due to weaker metal-metal bond and the difference in the preferential binding sites.

Size and orientation of the metal clusters are important because small metal clusters are not symmetrical and have different surfaces with different crystallographic planes. The number and the type of surfaces in the cluster are dependent on the number of atoms, and consequently on the size of the cluster [70]. The influence of the metal cluster size on the metal-support interaction with MWCNTs has been studied by Bittencourt et al. [47]. Their XPS measurements have shown an increase in the binding energy of 4f core level with decreasing platinum cluster size. Similar effects have been observed in the binding energy of 3d level of palladium clusters deposited on amorphous carbon, as reported by Kuhrt et al. [71]. This means that smaller particles interact more strongly with the support than larger metal clusters.

Also, the graphitization degree of the support affects the metal-support interaction. The interaction between the catalytic metal and the amorphous or semi-crystalline carbons, such as carbon blacks or active carbons, is weaker than the interaction with more graphitic samples. Coloma et al. [53] have observed an increase in the resistance to sintering for platinum catalysts prepared with heat treated carbon black supports as compared to catalysts with untreated carbon black. A similar effect was observed on MWCNTs by Wang et al. [72]. They have compared as prepared MWCNTs and MWCNTs graphitized by thermal treatment as platinum support in electrocatalysis. The results have shown that the catalyst with graphitized MWCNTs as support is less prone to sintering

under electrochemical oxidation conditions. The increased resistance to sintering in both studies was attributed to increased strength of π-sites (sp^2-hybridized carbon) resulting an increase of metal-support interaction.

The heteroatoms in the carbon support can either increase the metal-support interaction (anchoring) or weaken it, dependent on the preparation method. The weakening effects can be observed when the electron drawing functional groups are weakening π-sites, making them less capable of interaction with the metal particles [53; 54; 55].

The orientation of the graphite planes affects the metal-support interaction because it affects the sites where metal clusters can be deposited. The surface of carbon can be either flat or curved basal planes such as for example on graphite or CNTs. Metal clusters can also be deposited on the edge of graphite planes which can be tilted as in FBCNFs or perpendicular to the CNFs direction, as in PlCNFs. Each orientation of the graphite planes can have several sites where the metal cluster can be deposited and those sites have different metal-support interaction. Sanz-Navarro et al. used molecular dynamics simulations to identify several different sites on PlCNFs, where Pt clusters can be deposited [73]. The simulation showed that at some of these sites the metal-support interaction can be strong enough to flatten the metal clusters, while on other sites the geometry of the metal clusters is not affected. Such strain effect causing deformations of the metal clusters can also be observed by electron microscopy [74].

Adsorption on the defects in the carbon structure is also very important. Kvande et al. [75] suggested that the high concentration of A-type defects (disordered carbon) on carbon black (Vulcan XC-72R) is responsible for the absence of the negative effect of oxygen-containing functional groups on the dispersion of

platinum, as compared to functionalized CNT and CNF supports without those defects.

Different chemical reactions require different catalyst properties. There is no theory that can predict the property of a catalyst by taking into account all the effects including the metal-support interaction and tailor a catalyst for a specific chemical process without extensive experimental work. Therefore, more fundamental experimental studies have to be done to understand how different support materials influence the properties of catalysts in different chemical processes.

1.5 Carbon nanotubes and carbon nanofibers in catalytic dehydrogenation

A large number of studies of different catalytic dehydrogenation reactions where nanostructured carbons have a significant role have been published. This includes dehydrogenation of ammonia-borane, cyclic alkanes, ethylbenzene, and straight chain hydrocarbons.

Dehydrogenation of ammonia-borane

Dehydrogenation of ammonia-borane is one of many promising approaches to storing and producing hydrogen. Chen et al. [76] have demonstrated that Pt/MWCNT catalysts can be used to catalyze this reaction. Before the reaction, MWCNTs were oxidized by an acid treatment and subsequently temperature treated in an Ar atmosphere at 800 °C. This treatment introduced electron deficient defects. It was reported that those defects transferred electrons from the platinum nanoparticles and thus promoted the ammonia-borane hydrolysis reaction.

Dehydrogenation of cyclic alkanes

Another promising route for hydrogen storage and production is dehydrogenation of cyclohexane and decalin. Lazaro et al. [77] have studied dehydrogenation of decalin over platinum catalysts with CNFs and activated carbon (AC) as a catalyst support. Platinum supported on HNO_3 oxidized CNFs exhibited approximately fourfold higher hydrogen production and less deactivation than Pt/AC catalysts. The CNF-supported catalysts had a higher metal dispersion (76.7%) than the AC-supported catalyst (54.6%). However, dispersion alone cannot explain the difference in the catalyst activity. It was proposed that Pt/AC catalyst was deactivated faster due to the plugging of micropores, which are absent in the Pt/CNF catalyst, demonstrating an advantage of the nanostructured catalyst support over conventional catalyst support. Jian-ping et al. [78] have compared different platinum catalysis on nanostructured carbon supports for dehydrogenation of cyclohexane. In this study, platinum deposited on carbon nanoparticles exhibited a better activity and stability than platinum on MWCNT, AC, and carbon black. This was attributed to a better resistance of the nanoparticle-supported catalyst to coke poisoning, due to a favorable diffusion of benzene in the short pore channels of the carbon nanoparticles. This is another demonstration of how the structure of the catalyst support can influence the reaction.

Oxidative Dehydrogenation of ethylbenzene to styrene

Carbon materials can be used as a catalyst for the oxidative dehydrogenation of ethylbenzene (EB) by themselves. Pereira et al. [26] have demonstrated that oxidized MWCNTs are less active than AC; however, the MWCNT catalyst is more stable due to a higher resistance to gasification. Comparison of oxidized and unoxidized MWCNTs shows than the oxygen-containing functional groups play a critical role in this reaction. Delgado et al. [35] have reached similar

conclusion after comparing MWCNT catalysts that have undergone different thermal treatments in an inert atmosphere to remove the oxygen-containing functional groups. MWCNTs that have undergone thermal treatment at high temperature have decreased catalytic performance. The same observation has been reported by Zhao et al. [79]. They have compared different carbon nanofibers as catalyst for the oxidative dehydrogenation of ethylbenzene and have reported that removing the surface oxygen and graphitizing the nanofibers with angle between graphite platelets and the longitudinal axis of 20-30° and 30-45° by high-temperature treatment reduced the conversion, without any significant change in the selectivity. In addition, an induction period of about 1-3 hours or an oxidative pretreatment was necessary to obtain a stable conversion. Low EB conversion (2%) was observed in the absence of oxygen in the feed, indicating that surface groups formed in the presence of oxygen are necessary for the reaction. Fishbone fibers with an angle between graphite platelets and the longitudinal axis of 20-30° were more active than CNFs with other angles (0-5°, 30-45°, and 90°). The authors reported that the difference in the catalytic activity of different CNFs was a result of a ratio of prismatic and basal plane areas. Basal planes are necessary for adsorption of the phenyl ring via π-electron interaction. On the other hand, adsorption of ethyl groups takes place via a bond between the H-atoms in the ethyl group and the O-atoms at prismatic edges. The low activity of tubular carbon with low angles (0-5°) was explained by a difficulty of formation of the oxygen-containing surface groups on inert basal planes. Furthermore, platelet carbon nanofibers (90°) expose the edge sites partially covered with oxygen-containing groups and this resulted lower activity and a higher selectivity to CO_2. Fishbone fibers with angle 20-30° had a higher activity than fishbone fibers with angle 30-45°. The latter had a lower surface area and a higher concentration of oxygen-containing groups. The

authors concluded that god performance of Fishbone fibers with angle 20-30° is due to an optimum ratio between prismatic and basal plane sites on the surface.

The oxidative dehydrogenation of EB can also be used as a model reaction to study carbon-supported metal catalysts. Guo et al. [80] have compared cobalt and nickel catalysts deposited on MWCNTs and AC. The MWCNT-supported catalysts exhibited a higher EB conversion, higher styrene selectivity, and higher styrene yield. This was attributed to structural differences between MWCNTs and activated carbon-supported catalysts, however, no further details were given. The cobalt catalysts (9.5 wt% and 12.6 wt% metal loading) have shown a better performance than nickel catalysts (9.3 wt% and 13.1 wt% loading). In this study, an unusual method of catalyst preparation was used. The catalytic metal was originated from a growth catalyst (Ni or Co on SBA-15) and the support of this growth catalyst was removed by a NaOH solution. This is important since the deposition sites of the active metal particles were different (on the tips of the nanotubes) than if the active metal would be deposited on the purified MWCNTs.

Dehydrogenation of straight chain hydrocarbons

The oxidative dehydrogenation of straight chain hydrocarbon is an important topic where the effect of nanostructured carbons has been studied, while the non-oxidative dehydrogenation over carbon-supported catalysts has been studied to a lesser extent. Liu et al. [81] have done a study on the oxidative dehydrogenation of 1-butene at 400 °C over MWCNTs, two different activated carbons, and α-Fe_2O_3. After 20 hours induction period, MWCNTs exhibited better conversion (45%) and yield (29%) towards butadiene than other tested catalysts. As with the oxidative dehydrogenation of EB the catalytic activity of metal-free MWCNT is related to the oxygen functional groups, especially quinone groups that are created during the induction period. A better catalytic

activity of MWCNT than active carbons is caused by a higher resistance to coking and to gasification (combustion). Zhang et al. [82] has reported that the selectivity to alkene products (1-butene, 2-butene, and butadiene) in the oxidative dehydrogenation of n-butane can be improved by an addition of a small amount of phosphorus (phosphate) to a MWCNT catalyst. This addition passivates defects and suppresses combustion of hydrocarbons.

Sui et al. [39] studied phosphate impregnated CNFs for the oxidative dehydrogenation of propane. They have reported that impregnation of CNFs with phosphate can reduce both propane over-oxidation and the gasification of the catalyst by decreasing the availability of the sites where oxidation takes place.

1.6 Carbon nanotubes and carbon nanofibers in electrochemistry

Use of carbon in electrochemistry dates back to Sir Humphrey Davy`s application of graphite electrodes for the electrochemical production of alkali metals. “Classical” carbon materials, such as graphite, glassy carbon, and carbon black, are indispensable for use as electrodes in both analytical and industrial electrochemistry due to their low cost, electrical conductivity, and chemical stability.

One of the most important research topics in electrochemistry today is the development of cost-effective fuel cells. A fuel cell converts the chemical energy of fuel oxidation in the presence of a catalyst into electricity. The main issue of fuel cells today, is a low durability and high intrinsic cost. To make fuel cells more attractive, new materials, especially catalysts, should be developed. A commonly used catalyst in fuel cells is platinum on a carbon support, typically on carbon black. However, the carbon black-supported platinum catalyst is

vulnerable to poisoning (CO, S, etc.), is thermo-chemically unstable, and contains inaccessible micropores and impurities [83]. Therefore, alternative platinum supports have been studied and this includes nanostructured carbon materials such as CNTs and CNFs. Those new materials have better-defined porosity and a potential for better metal-support interaction, leading to better Pt utilization and more durability [23].

Carbon nanotubes as catalyst supports in electrocatalysis

Carbon nanotubes are the most studied nanostructured carbon material for application as a catalyst support in fuel cells. Both SWCNTs and MWCNTs have been studied and MWCNTs have been found to be more conductive, while SWCNTs provide larger surface areas [83]. Due to higher availability of MWCNTs than SWCNTs, MWCNT-supported catalysts are studied more frequently.

Park et al. [84] have compared the electrochemical stability of Pt supported on MWCNT and Pt supported on carbon black when used for oxygen reduction reaction (ORR). Pt/MWCNT catalyst has demonstrated a higher retention of the electrochemical area, a smaller increment of interfacial charge transfer resistance, and a slower degradation of the fuel cell performance. This was explained by a higher corrosion resistance of MWCNTs in oxidizing conditions and stronger metal-support interaction preventing sintering of platinum particles. A higher electrochemical stability of MWCNTs to oxidation compared to carbon black has also been reported by Shao et al. [85]. They have electrochemically oxidized MWCNTs and carbon black and measured the oxygen content by X-ray photoelectron spectroscopy. It was found that carbon black acquired oxygen heteroatoms at a higher rate than MWCNTs at the same conditions. This can be explained by a lower concentration of susceptible to oxidation defects and dangling bonds in MWCNTs than in carbon black. This was in spite of

MWCNTs having higher initial oxygen content than carbon black, probably due to the oxidizing purification pretreatment of as synthesized MWCNTs. Similar observations were reported by Li et al. [86]. Wang et al. [72] have compared the oxidation resistance of MWCNTs with and without pretreatment at high temperature in an argon atmosphere. They have reported that graphitized MWCNTs are more resistant to oxidation. Graphitized MWCNTs used as platinum support led to a more durable catalyst in electrochemical durability test, as compared to the catalyst with untreated MWCNT support. This was explained not only by a higher resistance to oxidation of graphitized MWCNT support, but also stronger metal-support interaction due to increasing strength of anchoring π-sites on the graphitized MWCNTs.

Many authors have also reported high activity for ORR of nitrogen doped CNTs (and other carbons) without platinum [87]. Geng et al. [88] and Alexeyeva et al. [89] have compared platinum-free nitrogen doped and undoped CNTs for ORR in both acidic and alkaline solutions. They have reported that nitrogen doping improves the electrocatalytic activity of carbon nanotubes in both acidic and alkaline electrolytes, with alkaline electrolyte system giving more promising results and having potential to replace the costly Pt/C catalyst in fuel cells in the future. The mechanism for ORR over nitrogen doped CNTs still debated and it is not yet clear if pyridinic nitrogen or quarternary nitrogen in the carbon matrix is responsible for the ORR activity [87].

Carbon nanofibers as catalyst supports in electrocatalysis

Also, CNFs have been extensively researched as fuel cell supports. Zheng et al. [90] have studied the effect of CNF structure for application as palladium support in ORR. The CNF-supported catalysts were also compared to activeted carbon-supported catalysts, all prepared by the incipient wetness impregnation method. It was reported that the catalyst dispersion was best in PlCNFs, due to

the highest density of edge atoms to basal atoms. The activated carbon-supported catalyst had the lowest dispersion with a wide range of particle size distributions because of weak MSI. The PlCNF-supported catalyst was the most active for ORR as seen from the position of the peak potential and Pd/AC catalyst was the least active. In addition, compared to Pd/FBCNF, Pd/PlCNF catalyst had better diffusion properties due to a larger mesopore volume. Li et al. [91] have reported that oxidized stacked-cup CNFs displayed better performance in a PEMFC than commercial carbon black. This was attributed to a high aspect ratio of CNFs providing a continuous conducting network in the Nafion® matrix, and this can result in better utilization of the catalyst metal. Kang et al. [92] have demonstrated that herringbone CNFs (FBCNFs) supported Pt-Ru catalysts are less prone to metal leaching in 1M H_2SO_4 at 70°C than commercial activated carbon-supported catalyst. This was confirmed by a better durability of the CNF-supported catalysts in electrochemical durability tests in membrane-electrode assembly. The CNF-supported catalyst with loading 40 wt% Pt-Ru was more active for MOR (methanol oxidation reaction) than the commercial AC-supported catalyst with the same loading. However, when the catalysts with 70 wt% loadings were compared, the commercial AC-supported catalyst was slightly more active. This demonstrated that in spite of many advantages of CNF-supported catalysts over AC and carbon black-supported catalysts, the metal catalyst utilization on CNFs when high loadings are used can still be difficult due to lower surface area.

Bessel et al. [93] have compared platinum supported on carbon black with platinum supported on three different types of CNFs: platelet, ribbon, and herringbone (fishbone) for MOR. While the herringbone-supported catalyst exhibited a poor catalytic activity, both PlCNF and ribbon CNF-supported catalyst exhibited a significantly higher activity than the carbon black-supported catalyst. It was suggested that the low activity of herringbone-supported fiber

was related to the high hydrophilicity (functionalization) of the CNF surface. In addition to higher activity, PlCNF and ribbon CNF-supported catalysts were less susceptible to CO poisoning than carbon black-supported catalysts. Several different explanations has been offered, including different mechanism for the removal of adsorbed species, different electrical conductance, poisoning impurities in the carbon black support, and favorable metal-support interaction with CNFs causing the attainment of a preferred crystallographic orientation of the platinum particles. The latter explanation for Pt/PlCNF was confirmed by TEM images showing more spherical and less crystalline particles on carbon black compared to particles on PlCNFs, indicating stronger metal-support interaction on PlCNFs. Similar results were reported by Muthuswamy et al. [74]. They have compared PlCNFs and carbon black as a catalyst support for MOR. Also in this case the PlCNF-supported catalyst was more active than the carbon black-supported catalyst. This was attributed to a strong metal-support interaction between platinum particles and the PlCNF support causing a significant reconstruction of the metal particles. This reconstruction led to a formation of more faceted particle surfaces, which were more beneficial for the reaction.

1.7 Dehydrogenation of light alkanes

Light alkenes have become essential for the industrial production of many chemicals and materials, especially for the production of polymers and synthetic rubber. More than half of the global demand for ethene is created by the production of the world's most widely used plastic, polyethene [94]. Likewise, more than half of global demand of propene is created by the polypropene production [95], [96]. The high demand for plastics made ethene and propene the first and the second most important intermediates in the petrochemical

industry. Crude oil and natural gas mainly consist of saturated or aromatic hydrocarbons and do not contain alkenes. Therefore, ethene, propene, and other alkenes have to be produced by expensive and energy demanding processes. Today the main commercial processes for light alkenes production are steam cracking of naphtha and fluid catalytic cracking of heavier oil fractions. Those processes coproduce ethene and propene. For example, about 57% of produced propylene come from cracking processes, 33% as a byproduct of the refinery processes, and only 10% from other sources [97]. However, in both the cracking and the refinery processes propene is a byproduct. Hence, neither of those processes can be optimized to meet the increasing global demand for propene. Recently, the exploration of shale gas reserves in the USA has reduced the ethane prices considerably, giving the lighter steam crackers (ethane fed) a feedstock advantage over the competing naphtha-fed steam crackers. Since the lighter steam crackers do not produce any significant amounts of propene, this shift in technology makes on-purpose propene production processes (for example catalytic dehydrogenation) more competitive [98; 99]. It is forecasted that the on-purpose alkene production methods, such as propane dehydrogenation and methanol to alkene processes, where the methanol can be produced from coal or natural gas, can become more important in the near future [100; 95].

One of the first commercial dehydrogenation processes was the dehydrogenation of butanes over a chromia-alumina catalyst [101]. This process was widely used during WWII to produce butenes, which were subsequently dimerized to produce fuel. In the late 1980s, this process was expanded to dehydrogenation of propane and isobutane and called Catofin^{TM} [102]. The development of catalytic reforming with platinum catalyst in 1940s has demonstrated that the Pt catalysts have a potential for the dehydrogenation of alkanes [103]. Platinum is a very important dehydrogenation catalyst because it has god ability for activating the

C-H bond and has a low activity for C-C bond breaking. The C-H bond breaking occurs at all platinum sites, while the C-C breaking occurs primarily on sites with low coordination number, for example, a surface with steps [104]. In the 1960s a process for the selective dehydrogenation of long chained alkanes over a Pt catalyst was commercialized [105] and later the UOP Oleflex™ process for dehydrogenation of propane and isobutane over continuously regenerated noble metal catalysts was commercialized. As of 2014 this process is the main process for direct dehydrogenation of light hydrocarbons over noble metal catalysts.

The equilibrium constant for the dehydrogenation reaction increases with increasing carbon number. Therefore, selective dehydrogenation of light hydrocarbons requires much more severe conditions than dehydrogenation of heavier hydrocarbons [106]. This is the reason why a commercialization of the selective ethane dehydrogenation process is more difficult than the propane dehydrogenation. The dehydrogenation reactions involve an increase in the number of molecules (equation 1) since saturated hydrocarbon molecules are converted to unsaturated hydrocarbon molecules and hydrogen molecules. Therefore, the reaction is pressure-dependent and a high alkane conversion is favored by a low partial pressure of hydrocarbons according to Le Chatelier's principle.

$$C_3H_8 \xleftrightarrow{Catalyst,heat} C_3H_6 + H_2 \qquad \Delta H^o_{298} = +124 kj/mol \qquad (1)$$

The dehydrogenation of propane is endothermic with $\Delta H^o_{298} = +124$ kj/mol [104], [107]. Hence, to achieve an acceptable conversion, the reaction has to be done at high temperature, as seen in Figure 1.3. The same conditions favor coke formation that leads to catalyst deactivation and makes frequent regeneration necessary. This gives higher operation costs and can also induce structural changes in the catalyst, reducing its activity [108].

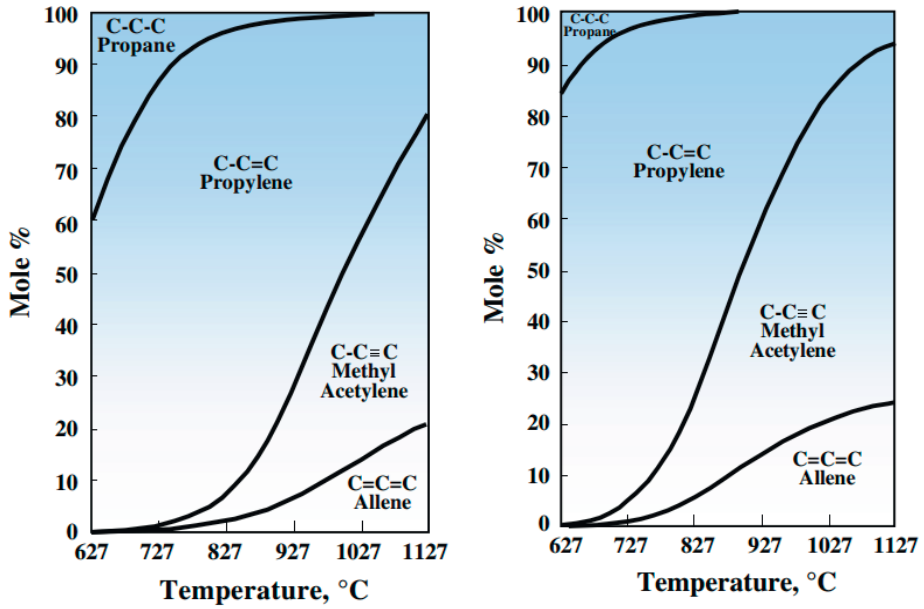

Figure 1.3 Dependence of propane dehydrogenation equilibrium product composition on temperature and pressure [106]. Mole fraction of dehydrogenated products increases with increasing temperature and decreasing pressure. Left: composition at 1 atm absolute pressure. Right: composition at 0.23 atm absolute pressure.

To avoid equilibrium limitations of light hydrocarbon dehydrogenation, other ways of catalytic dehydrogenation have been investigated. One of the most promising routes is the oxidative dehydrogenation (ODH). This process is thermodynamically favorable and, therefore, does not suffer from equilibrium limitations. However, there are still issues that have to be solved before this process can be commercialized. The main problem with oxidative dehydrogenation is the difficulty of controlling selectivity because the oxidative processes tend to propagate towards carbon oxides, rather than to stop at the desired alkenes.

The coke formation on the platinum catalysts is a result of the platinum-alkene interaction. For this reason, it is important to weaken the Pt-alkene interaction

without any significant decrease in the Pt-alkane interaction [101]. This will allow for alkenes to desorb faster from the catalyst surface after dehydrogenation and to a lesser extent undergo cracking or further dehydrogenation reactions. Arsenic, germanium, lead, bismuth, and tin are some of the elements that can be used as promoters to modify Pt-alkene interaction. The catalyst support is playing an important role in the activity, selectivity, and cost of catalyst [101]. The most commonly used support for Pt in direct catalytic dehydrogenation of propane is alumina, because of its thermal stability, mechanical strength, and, most importantly, ability to maintain high platinum dispersion [101]. The acidity of the alumina has to be reduced by modifiers to reduce cracking, and optimal pore structure should be controlled to maximize the mass transfer rate [101]. In this work, propane dehydrogenation is used as a model reaction to study effects of different carbon supports.

1.8 Hydrogenation of ethene

Hydrogenation of light linear alkenes is not an economically attractive process because unsaturated light linear hydrocarbons are usually more expensive than saturated. Nevertheless, the hydrogenation of alkenes has been studied both as a model reaction and for better understanding of the reaction itself. The hydrogenation of ethene is exothermic with $\Delta H^{o}_{298} = -133$kj/mol [109], and is not limited by the equilibrium.

$$C_2H_4 + H_2 \xleftrightarrow{Catalyst,heat} C_2H_6 \qquad \Delta H^{o}_{298} = -133 kj/mol \tag{2}$$

Deactivation of this reaction is caused primarily by side reactions of ethene hydrogenation, i.e. polymerization and dehydrogenated adsorption [110]. The rate of catalyst deactivation is strongly dependent on the catalyst itself. For example, polymerization is a major issue when Ni is supported on kieselguhr

(siliceous sedimentary rock), but not when the reaction occurs over unsupported Ni powder [110]. In addition, pretreatment of the catalyst is very important and must be precisely specified when catalysts from different studies are to be compared [110].

A mechanism for the hydrogenation of ethene over a platinum surface was proposed by Horiuti and Polanyi in the 1930s [111]. According to this mechanism, ethene adsorbs on the metal surface by breaking a C-C bond and forming two σ-bonds to the metal. The hydrogenation goes through an ethyl (M-CH_2CH_3) intermediate before ethane is produced. Development of spectroscopic techniques helped to bring more light on the reaction mechanism. For example the presence of two-σ-bonded ethene, ethyl, ethylidyne (M≡C-CH_3), and π-bonded ethene has been confirmed by spectroscopy on the Pt(111) surface and it was suggested that at specified conditions the ethyl intermediate and π-bonded ethene are the most important intermediates, while two-σ-bonded ethene and ethylidyne are hydrogenated at a much slower rate [112].

In spite of some reports of the particle size effects in the ethene hydrogenation [113; 114], it is commonly accepted that the ethene hydrogenation reaction over noble metals is structure insensitive, i.e. it is not affected by the type of the crystallographic surface of the active metal [112]. This means that the reaction rate at some conditions is proportional to the surface area of the catalytic metal, regardless of the particle size of this metal. Therefore, activity for the ethene hydrogenation can be used to compare the active surface area of different catalysts with the same catalytic metal. As with propane dehydrogenation, hydrogenation of ethene is used in this thesis as a model reaction to study effects of different carbon supports on the catalytic activity of Pt/carbon catalysts.

2. Experimental

2.1 Catalyst supports and catalyst preparation

Catalysts were prepared with five different commercially available carbon supports: synthetic graphite, platelet nanofibers, carbon black, conical platelet carbon nanofibers, and multiwalled carbon nanotubes. Information about the sample codes, particle sizes, and suppliers is presented in Table 2.1.

Table 2.1 Information about carbon materials used in this thesis.

Sample code	Commercial name and details	Particle size	Supplier
CB	VULCAN® XC-72R, carbon black	≈50 nm	Cabot Corporation
MWCNT	TNGM7, graphitized multi walled carbon nanotubes, 99.9% purity	30-50 nm (Diameter)	Chengdu Organic Chemicals Co. Ltd.
PlCNF	06-0170 carbon, stacked graphene platelet nanofibers, acid washed	40-50 nm (Diameter)	Chiron AS
CPCNF	PR-25-XT-HHT, graphitized, composed of conical platelets, thermally treated to 2900°C, <100 ppm iron content	125 – 150 nm (Diameter) 20-200 μm (Length)	Sigma-Aldrich
graphite	synthetic graphite powder,	< 20 μm	Sigma-Aldrich

The carbon-supported catalysts with a nominal loading of 1.0 wt% platinum were prepared by a modified polyol method, developed by Tsypkin et al. [115; 42]. This procedure consists of two steps, first platinum nanoparticles are prepared in a suspension, before the particles are loaded on to the supports. In the first step, hexachloroplatinic acid hexahydrate (0.644 g, $H_2PtCl_6 \cdot 6H_2O$,

Sigma-Aldrich) was dissolved in ethylene glycol (288 ml, EG, Fluka) and a 1.0 M solution of NaOH (Merck) in EG (32.0 ml) was added to the mixture. The mixture was first heated to 150.0 °C for three hours to reduce platinum while stirred and purged with argon (99.999%) and then cooled down to 25.0 °C. In the second step, a part of the Pt/EG suspension (40.0 ml) was sonicated for 5 minutes, heated to 150.0 °C while stirred and purged with argon. Then, the suspension was cooled down to 25 °C. After cooling, the support material (3.00 g) and argon purged ethanol (60.0 ml, 96%) was added to the Pt/EG suspension and the mixture was sonicated for approximately 10 minutes. Then the pH was reduced with an HCl solution (10.0 ml, 0.54 M, Merck) to pH 3.2 (± 0.1) and this mixture was sonicated again for 10 minutes. The deposition was done in a three-neck round-bottom flask by allowing the suspension to stand at 60 °C with Ar purge for 16 hours while stirred. Then the catalyst was extracted by centrifugation and washed by addition of Milli-Q water, dispersion in the water, and extraction by centrifugation. This washing procedure was repeated 10-20 times. Then the catalyst was washed twice with acetone by the same procedure and dried in air overnight at 70 °C.

2.2 Characterization

2.2.1 N_2-adsorption measurements

Nitrogen (99.999%) physisorption/desorption measurements were performed at liquid nitrogen temperature (77 K) using a Micromeritics 3000 Tristar II instrument. Before the measurement, the sample (100-200 mg) was evacuated at 200 °C and a pressure below 250 mTorr for 18 hours. BET specific surface area was calculated using the Brunauer-Emmet-Teller (BET) equation. Microporosity was determined using the t-plot method, while the total pore volume was

determined from the desorption isotherm using the Barrett-Joyner-Halenda (BJH) method.

2.2.2 Elemental analysis

Before the elemental analysis, the catalyst samples (approximately 400 mg) were burned in air at 900 °C to remove carbon. The heating rate was 5 °C/minute and this temperature was held for one hour before cooling down to 20 °C. Then the remaining ash was dissolved in freshly prepared aqua regia, a 1:3 mixture of HNO_3 (1.04 ml, 65%, Merck) and HCl (3.12 ml, 37%, Merck), and heated to boiling before dilution with Milli-Q water to 500 ml. The solution was analyzed for the Pt, Ni, Fe, and Cu content using an ELEMENT2 High Resolution ICP-MS.

2.2.3. Scanning electron microscopy

Scanning electron microscopy (SEM) images (micrographs) were recorded on a Hitachi S-5500 electron microscope by scattered electrons (SE) at 30.0 kV in a high vacuum. The samples were dispersed in ethanol (96%) and sonicated for approximately 5 minutes in an ultrasonic bath. The mixture was transferred to an aluminium sample holder and dried in air at room temperature (approximately 20 °C). Between 5 and 10 images were obtained from each sample and the most representative of them are presented.

2.2.4 Transmission electron microscopy

Transmission electron microscopy (TEM) micrographs were recorded using a JEOL JEM-2010 electron microscope, equipped with a tungsten filament, at an acceleration voltage of 200 kV. The samples were dispersed in isopropanol (99.9%, VWR) and sonicated for 5 minutes in an ultrasonic bath before being deposited on holey carbon TEM copper grids and dried in air at room

temperature. Average particle (cluster) size and a particle size distribution were obtained from 3-6 representative images (196-463 measured particles) of each sample. Dispersion ($Disp$) of one platinum particle was calculated from the particle size (d_m) using equation 3 and the average dispersion of all measured particles was reported.

$$Disp = \frac{6 \times \rho_{Pt} \times V_{Pt}}{10^{-7} \times d_m} = \frac{1.13}{d_m} \tag{3}$$

To avoid an overestimation of dispersion of small particles, the dispersion value of 1 was used for particles with a measured size of less than 1.13 nm. This equation assumes spherical particles, as done by Aramendia et al. [116] and an atom density on the Pt surface (ρ_{Pt}) of 1.24×10^{15} atoms/cm^2. This is the average atom density of (111), (100), and (110) crystal faces, as reported by Will [117]. The volume of one platinum atom (V_{Pt}) is 1.51×10^{-23} cm^3/atom and can be calculated from the density, the molar mass of platinum, and Avogadro's number.

2.2.5 Raman spectroscopy

Raman spectra were recorded on a Horiba Jobin Yvon LabRAM HR 800 spectrometer in air at room temperature and with a 632.8 nm He-Ne laser with effect of 30 mW as the excitation source. The laser was focused with a 10x objective and no filter was used during the measurement. The G, D, and D' peaks were fitted as Lorentzian peaks, while D" and I were fitted as Gaussian, as reported in literature [118; 119; 120].

2.2.6 Fourier Transform Infrared Spectroscopy

Diffuse reflectance infrared Fourier transform spectroscopy (DRIFTS) spectra were collected on a Nicolet iS50 FT-IR with 32 scans at 4 cm^{-1} resolution. The sample material was diluted by spectroscopy grade potassium bromide (KBr, Merk) and ground in an agate mortar. The background spectrum from pure KBr was subtracted. In addition, CO_2 and H_2O bands were removed by the OMNIC 9.2.86 software.

2.2.7 Thermogravimetric analysis

The TGA was done on Netzsch-STA 449C Jupiter thermo-microbalance to measure the metal loading by burning away carbon in a synthetic air flow (20.0 ml/min) and measuring the weight of the remaining ash. The ash weight from the metal-free material was subtracted from the ash weight of the platinum loaded samples to calculate the weight of platinum. An alumina sample crucible with between 10 and 30 mg of sample was used. The samples were heated to 950 °C at a heating rate of 10 °C/min and this temperature was held for 1 hour before cooling down to 20 °C.

2.2.8 Cyclic voltammetry

Potentiometric experiments were done in a conventional three-electrode cell with a VersaSTAT MC potentiostat with VersaStudio software. The reversible H_2 electrode (RHE), which is a subtype of the standard hydrogen electrode (SHE), was used as reference electrode, a platinum wire was used as counter (auxiliary) electrode, and a glassy carbon electrode with deposited sample on was used as the working electrode.

The catalyst samples were dispersed in a mixture of Milli-Q water and ethanol (96%) with 3:2 water to ethanol ratio. The concentration of the catalyst samples

in the suspension was 1.00 mg per ml. The suspension was sonicated until homogenous and 90.0 µg of catalyst was deposited on a disk-type glassy carbon electrode before drying in a N_2 (99.999%) flow. After the deposition and drying, 15.0 µl of Nafion® solution (0.5%, Sigma-Aldrich) diluted to 0.05% with ethanol was deposited on the electrode and dried again. The electrochemical cell was filled with H_2SO_4 solution (150 ml, 0.50 M) as electrolyte. This electrolyte was purged with N_2 (99.999%) for approximately 30 minutes prior to the measurement. The working electrode was electrochemically preconditioned from 0.05 to 1.20 V first at a scan rate 0.10 V/s and then at a scan rate 0.010 V/s. After conditioning, the potential was kept at 0.05 V and CO (99.3%) gas was bubbled through the electrolyte for 5 minutes. Then nitrogen was bubbled through the electrolyte for 30 minutes at this potential to remove excess CO and adsorbed CO was stripped at a scan rate of 0.010 V/s.

The stripping area related to CO oxidation (stripping), $Q_{CO\_oxidation}$, was obtained using equation 4, as done by Cuesta et al. [121]:

$$Q_{CO\_oxidation} = Q_{CO\_stripping\_total} - Q_{Pt\_oxidation} + Q_{CO\_adsorp\_initial} \quad (4)$$

Where $Q_{CO\_stripping\_total}$ was obtained by subtracting the background Q obtained without CO adsorbed (second cycle) from the voltammogram obtained with CO (first cycle). $Q_{Pt\_oxidation}$ was calculated by integration the peak associated with reduction of Pt oxide and $Q_{CO\_adsorp\_initial}$ was assumed to be zero.

The catalyst dispersion ($Disp$) was calculated by first calculating the active surface area of the catalyst, i.e. the area available for CO adsorption (S_{CO}), as seen in equation 5:

$$S_{CO} = \frac{Q_{CO\_oxidation}}{Q \times R} \quad (5)$$

Where Q is the CO monolayer stripping charge, 0.420 mC/cm^2 [74; 122; 123] and R is the stripping scan rate, 0.010 V/s. Then the number of active platinum atoms ($N_{activePt}$), i.e. atoms available for the CO adsorption was calculated, according to equation 6,

$$N_{activePt} = \frac{S_{CO}}{A_{Pt}} \quad (6)$$

Where A_{Pt} is the area of one platinum atom (8.06×10^{-16} cm^2/atom, inverse of the surface atom density used in equation 3). Then the dispersion was calculated using equation 7:

$$Disp = \frac{N_{activePt}}{N_A \frac{m_{Cat} X_{Pt}}{M_{Pt}}} \quad (7)$$

Where N_A is Avogadro`s number (6.022×10^{23}), m_{Cat} is the catalyst mass (gram), X_{Pt} is the metal loading of the catalyst ($g_{metal}/g_{catalyst}$), and M_{Pt} is the molar mass of platinum, 195.08 gram/mol. The average particle size (d_m) can then be calculated using equation 3.

2.2.9 Hydrogen chemisorption

Hydrogen chemisorption was carried out order to estimate metal dispersion on two different instruments. The volumetric chemisorption was carried out on a Micromeritics ASAP 2020 unit, while the dynamic pulse chemisorption was carried out on a Hiden CATLAB microreactor combined with a Hiden QGA mass spectrometer.

For the volumetric chemisorption, the sample (150-200 mg) was loaded together with quartz wool in a U-shaped quartz reactor heated by an electrical furnace. The sample was initially evacuated at 100 °C for 0.5 h and then reduced in H_2 (99.999% purity) flow while heating to 500 °C with a heating rate of 10 °C/minute. When the temperature reached 500 °C, the sample was cooled down in a He flow and the measurement was done at 35 °C. After the measurement of the first isotherm, the sample was evacuated for 30 min and a second isotherm was measured in order to separate strongly and weakly bonded H_2.

For the pulse chemisorption, 12-55 mg of sample was loaded in a quartz tube reactor together with quartz wool. The sample was heated in He (flow rate 40 ml/min, 5 °C /min) up to 500 °C and cooled down to 40 °C before measurement. Helium (99.999% purity) was used as carrier gas and the He/H_2 (95:5) mixture was used as the pulse gas. The pulse volume was 100 µl.

2.2.10 Measurement of Zeta potentials

Zeta potentials were measured with Zetasizer Nano ZS (Malvern Instruments Ltd.) using electrophoretic light scattering method in which particles move under an external electric field and their mobility is determined from the Doppler shift of scattered light. The Smoluchowski approximation was used, as is commonly done in polar solutions of moderate electrolyte concentrations [124; 125]. The measurements were done in disposable capillary cell (DTS1070)

at 35 °C. The carbon samples were dispersed in ethylene glycol/ethanol/H_2O (4:6:1) solution containing 0.09 mol NaCl per liter. The pH was adjusted manually with HCl (Merck) and NaOH (VWR Chemicals AnalaR NORMAPUR) aquatic solutions and measured by a Mettler Toledo SevenEasy benchtop pH meter.

2.3 Catalytic testing

2.3.1 Propane dehydrogenation experiments

Catalytic tests were performed at atmospheric pressure in a tubular fixed bed quartz reactor, where the catalyst powder (0.100 g) was placed on a quartz frit (pore size 40-90 μm) and held in place with quartz wool. The reactor was heated by an electrical oven with the temperature controlled by a thermocouple placed in a quartz tube and touching the catalyst bed. The catalyst reduction was done in He (99.996%), H_2 (99.999%), and N_2 (99.999%) flow in 50:25:25 ratio with a total flow of 100 ml/min while heated to 500 °C. For experiments without prior reduction, the heating was done in 100 ml/min flow of He/N_2 with 50:50 ratio. In both cases the heating rate was 9.5 °C/min. The gaseous products were analyzed with an Agilent 3000 Micro Gas Chromatograph with a thermal conductivity detector (TCD). Nitrogen (99.999%) was used as an internal standard for calculation of propane conversion and carbon based product selectivities. The dehydrogenation of propane was carried out at 500 °C with feed gases H_2 (99.999%), C_3H_8 (99.3%), and N_2 (99.999%) in 0:28:78 or 4.4:28:70 ratios, with a total flow rate of 100 ml/min. A schematic of the setup is shown in Figure 2.1.

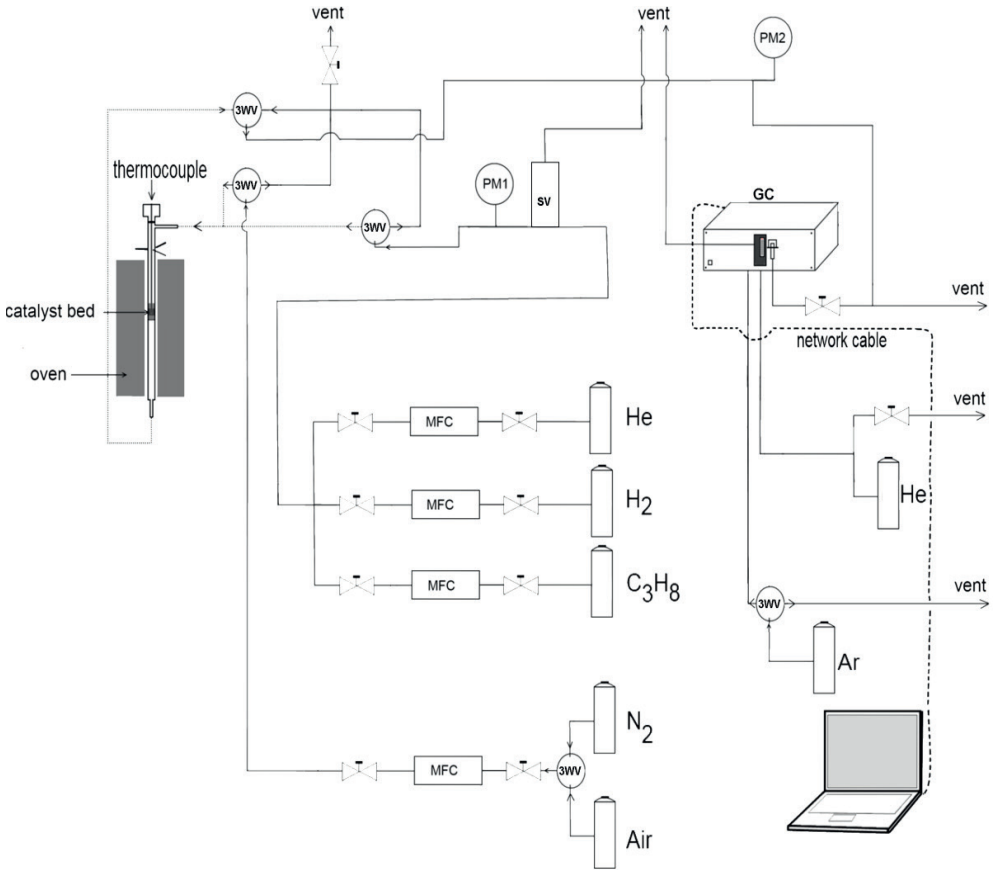

Figure 2.1 Schematic of the setup used for dehydrogenation experiments. PM1 and PM2 are pressure meters and 3WV is a 3-way valve. MFC is mass flow controller and SV is a safety pressure release valve.

Conversion (χ) and selectivity (S_i) were calculated using equation 8 and 9 respectively.

$$\chi = \frac{v_{C_3H_8\_in} - v_{C_3H_8\_out}}{v_{C_3H_8\_in}} \tag{8}$$

$$S_i = a_i \frac{v_{i\_out}}{v_{C_3H_8\_in} - v_{C_3H_8\_out}} \quad (9)$$

Where $v_{C_3H_8\_in}$ is the propane flow in the feed, $v_{C_3H_8\_out}$ is the propane flow in the outlet, and v_{i_out} is the flow of product i in the outlet. The carbon selectivity factor, a_i, is dependent on the number of carbon atoms of the hydrocarbon product molecules and is 1/3 for CH_4, 2/3 for C_2H_4 and C_2H_6, and 1 for C_3H_6. The carbon balance number (CBN) was calculated using equation 10, where the flow of each product was multiplied by the carbon selectivity factor and their sum was divided by the propane flow in the feed.

$$CBN = \frac{100 \times (v_{C_3H_8\_out} + v_{C_3H_6} + a_{C_2H_4} v_{C_2H_4} + a_{C_2H_6} v_{C_2H_6} + a_{CH_4} v_{CH_4})}{v_{C_3H_8\_in}} \quad (10)$$

The molar reaction rate, $R_{C_3H_6mol}$, (mol/(g_{cat}×s)) was calculated using equation 11 where V_{mol} is the molar volume at 20 °C and 1 atm (24044 ml/mol) and m_{Cat} is the catalyst mass in gram.

$$R_{C_3H_6mol} = \frac{v_{C_3H_8\_in} \times \chi \times S_{C_3H_6}}{60 \times V_{mol} \times m_{cat}} \quad (11)$$

The turnover frequency (TOF) for the reaction over each catalyst was calculated using equation 12, where $R_{C_3H_8mol}$ is the reaction rate (mol/(g_{cat}×s)), M_{Pt} is the molar mass of platinum (195.08 gram/mol), $Disp$ is the catalyst dispersion, and X_{Pt} is the metal loading of the catalyst ($g_{metal}/g_{catalyst}$). The reaction rate after 10 min on stream was used in this calculation.

$$TOF = \frac{R_{C_3H_8 mol} \times M_{Pt}}{Disp \times X_{Pt}} \quad (12)$$

In order to compare with the chemical equilibrium, the simulation data for propane dehydrogenation were calculated with the UniSim® Design R400 software (Honeywell). The modeled reaction temperature was 500 °C and the reaction pressure was 1.0 atm. Only the propane dehydrogenation reaction to hydrogen and propene was considered. The Peng–Robinson equation of state and conditions of equilibrium reactor were used in the simulation.

2.3.2 Ethene hydrogenation experiments

The ethene hydrogenation experiments were done at approximately 100 °C at the same setup as the propane dehydrogenation experiments (Figure 2.1). The catalyst (0.0050 g) was diluted by 1.000 g of silicon carbide (powder, particle size between 53 μm and 90 μm), loaded in a reactor and reduced the same way as for propane dehydrogenation. The feed composition for catalyst testing was H_2 (99.999%), C_2H_4 (99.95%), and N_2 (99.999%) in 15:10:75 ratio and the total flow rate was 100 ml/min. Conversions were compared after 60 minutes on stream to allow the reaction temperature to stabilize. The conversion of ethene was calculated using equation 13, by analogy with equation 8 for propane dehydrogenation.

$$\chi = \frac{v_{C_2H_4\_in} - v_{C_2H_4\_out}}{v_{C_2H_4\_in}} \quad (13)$$

As with propane dehydrogenation, nitrogen was used as an internal standard to compensate for volume (flow) change during the reaction.

3. Results and discussion

3.1. Catalyst morphology and properties

Carbon samples were heated in airflow while sample weight was measured. The TGA results in Figure 3.1 show that different carbon samples had different onset temperature for oxidation, i.e. the temperature at which the sample weight begun to decrease. This way the sample resistance towards oxidation was determined. The samples with lower onset temperature were more prone to oxidation. The order of the oxidation resistance of the carbon supports was:

graphite > MWCNT ≈ CPCNF > CB > PlCNF

According to Sebastian et al. [126] the ability of carbon to resist oxidation is related to the graphitic character and functionalization. Córdoba et al. [127] have reported that the oxidation resistance is influenced by the graphite sheet arrangement and graphitization degree. In addition, metal impurities can catalyze oxidation of carbons. Obtained results for the oxidation resistance show some correlation with the graphitization degree obtained by Raman spectroscopy (page 69). As expected, high surface area and low graphitization degree supports PlCNF and CB have low oxidation resistance; while low surface area and more ordered graphite has a higher resistance to oxidation. The stability of CPCNF was lower than the stability of graphite. This contradicts the results from Raman that have shown that CPCNF has a higher I_G/I_D band ratio than graphite and is therefore more ordered. Similarly, it cannot be explained by different impurity level since no significant amount of impurities was detected in the elemental analysis (page 50). However, CPCNF has a higher BET surface area than graphite, as determined by N_2 physisorption (page 54), and hence

CPCNF has a larger area that is exposed to air during heating. This can reduce the oxidation resistance of CPCNF compared to graphite.

In addition to the order of the oxidation resistance, the order of the oxidation rates (TG curve slope) can give information about the structure of carbon. Those rates are seen as the first derivative of TG curves with respect to time. High oxidation rates lead to steeper TG curve (higher slope) and higher negative value in DTG curve as presented in Figure 3.1. The order of the oxidation rates is as follows:

CPCNF > CB > MWCNT > graphite > PlCNF

The TG curve of CPCNF is steeper than graphite, PlCNF, MWCNT, and even the CB TG curve. The high slope of CB TG curve can be explained by the oxidation-susceptible semi-amorphous structure, while the high slope of the CPCNF TG curve cannot be explained by an amorphous structure, because CPCNF is highly ordered, as determined by Raman spectroscopy (page 69). Low concentration of amorphous carbon is seen indirectly in CPCNF by the high temperature of the initiation of gasification (>630 °C). However, once the gasification has started, the rate of gasification increased rapidly. According to TEM results (page 63) a typical CPCNF fiber consists of two layers, a multiwalled layer, similar to MWCNT on the outer surface of the fibers and a tilted layer on the inner surface of those fibers. The basal planes on the outer surface could be more resistant to the oxidation, while the oxidation of the inner surface could be limited by diffusion limitations. When the outer layers are oxidized the inner layers will become more exposed and will rapidly oxidize as well. This could explain why the combustion rate is so high for this sample. MWCNT has a lower gasification initiation temperature (≈ 610 °C, after 58 min) than CPCNF, probably because of a higher concentration of defects, as determined by Raman spectroscopy (page 69). In spite of this, MWCNT is

combusted slower than CPCNF because high aspect ratio nanotubes expose predominantly basal planes and do not contain tilted layers as in CPCNF.

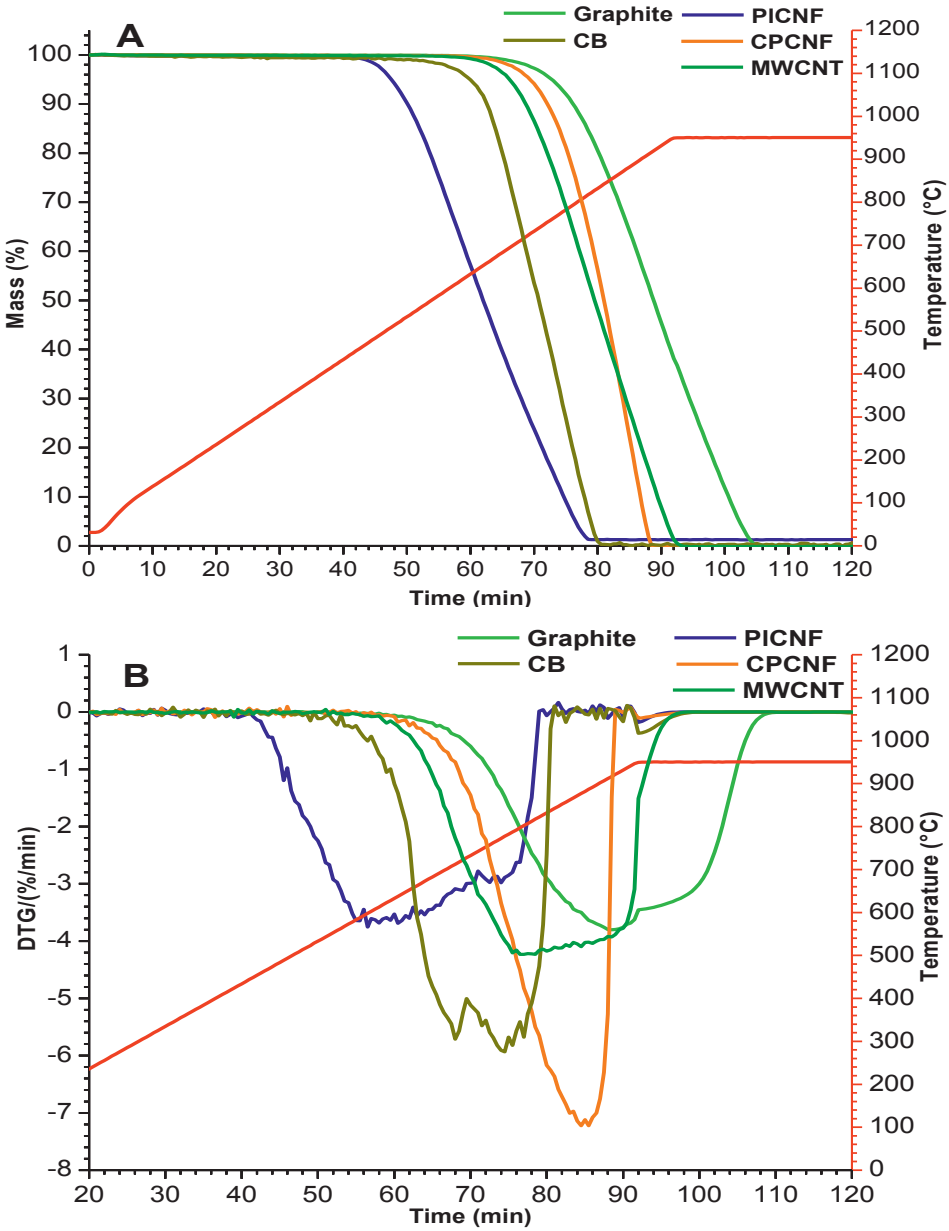

Figure 3.1 Gasification curves (TG) of the supports (A) and first derivative of TG curves with respect to time (B).

Similarly, graphite exposes predominantly basal planes which are less susceptible to oxidation. Since the oxidation probably occurs mainly along the edges of the layers, it will progress slower than when compared with for example CB. The slow oxidation of PlCNF is related to the inhomogeneous distribution of metal impurity catalyzing the oxidation as described below.

The gasification curves showing resistance to oxidation of the platinum-containing catalysts are presented in Figure 3.2. The deposition of platinum has severely reduced the resistance of oxidation of all the tested supports, except for PlCNF, which was almost unaffected. The order of the oxidation resistance of carbon supports with platinum was:

Pt/graphite > Pt/CPCNF > Pt/MWCNT > Pt/PlCNF > Pt/CB

This order did not match the order of graphitization degree as determined by the Raman spectroscopy (page 69) but is in god correlation to the order of carbon support BET surface areas (page 54). The ability of platinum to catalyze the oxidation of carbon has been reported by many authors [128; 129]. This effect was much more important for reducing the oxidation resistance than the presence of defects in the carbon structure. The effect of platinum deposition is clearly seen when the temperatures at which 50% of the material is combusted are compared. Such temperatures for two parallel measurements are presented in Table 3.1. The precision of the measurements is low due to high heating rate (10 °C/min) and possibly uneven distribution of material in the crucible. However, for all the tested samples, with the exception of PlCNF, the deposition of Pt have reduced average $T_{m(1/2)}$ between 175 °C and 206 °C. For PlCNF, the reduction in $T_{m(1/2)}$ was less than 4 °C. This could indicate that PlCNF already contained an impurity that acted as an oxidation catalyst and reduced the oxidation resistance. As determined by ICP-MS (page 50), this impurity was Ni that probably originated from the growth catalyst for PlCNF production. The ability of Ni to

catalyze the oxidation of carbons and hydrocarbons is well known and has been reported by many authors [130; 131].

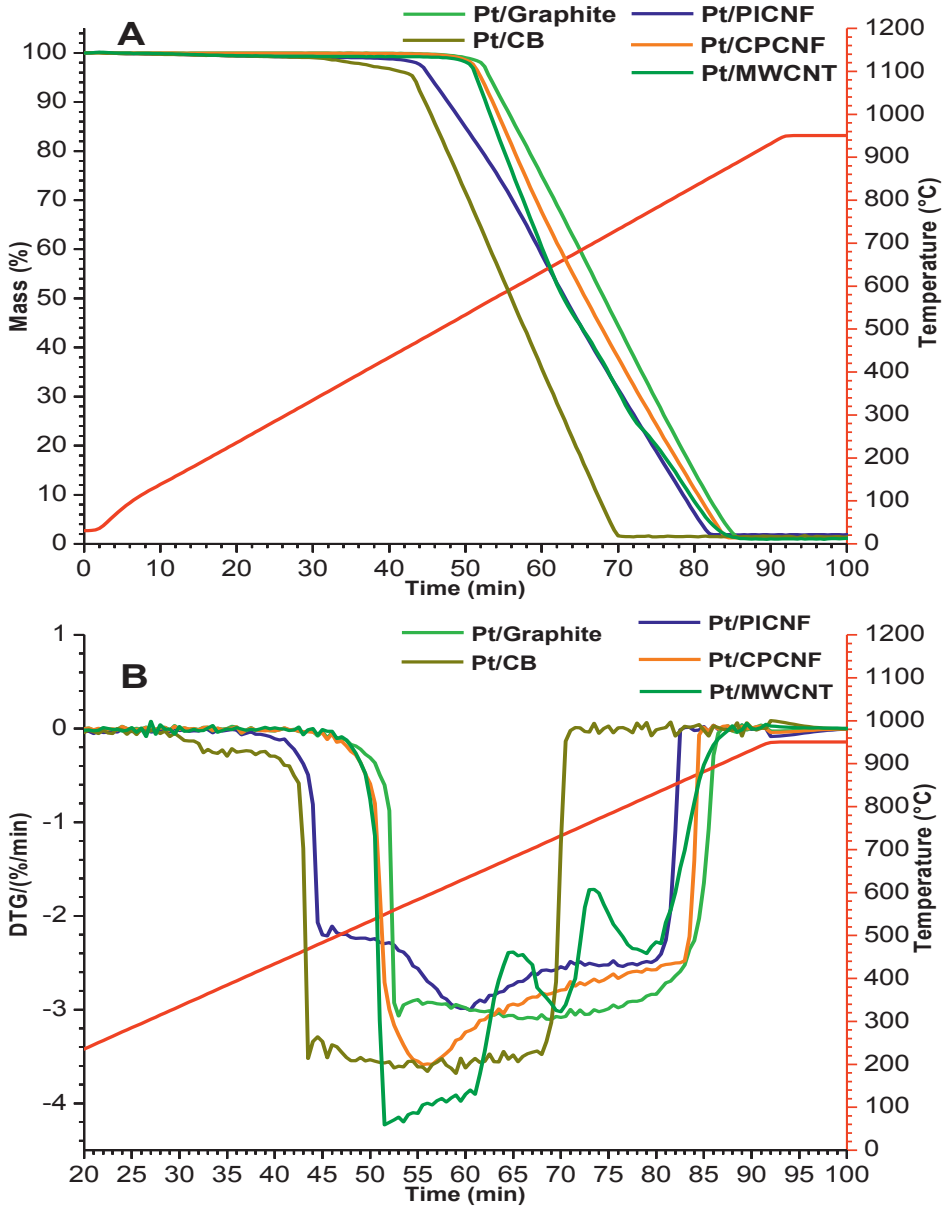

Figure 3.2 Gasification curves (TG) of the catalysts (A) and first derivative of TG curves with respect to time (B).

The first derivative with respect to time of TG curve for Pt/MWCNT is different from other curves by having regions where the mass decreases rapidly, followed by slowing down of the oxidation rate, as seen in Figure 3.2. This effect has also been seen by Stefov et al. [132] in oxidation of Co containing MWCNTs and can be related to a variation of temperature in the sample due to considerable amount of heat released as a result of MWCNT burning, followed by heat dissipation and a subsequent temperature drop. The ability of metal-containing MWCNTs to unevenly combust during programmed heating in air has also been described by Arepalli et al. [133].

Guterman et al. [128] has identified several segments for gasification of Pt-containing carbon black (XC-72R) in air. The number of segments and their slopes is dependent on metal loading, metal dispersion, and properties of the carbon support. Some of the segments can be observed in Figure 3.2. For example, Pt/CB gasification starts at 30 min (340 °C). This segment ends when the slope increases after 42 min (455 °C). Guterman et al. has identified two segments in this region, one due to decomposition of functional groups, and the second due to oxidation of the surface layers adjacent to the platinum nanoparticles. This segment is not as clear for metal-free CB, where the increase of the slope was more gradual.

The rate of oxidation can be influenced by the dispersion of platinum. The high concentration of platinum in some regions of the sample can cause local overheating, while regions with less platinum will be more stable and will oxidize at higher temperatures [128]. Therefore, the presence of carbon that is more stable to oxidation in air than the rest of Pt/Carbon sample can indicate an uneven distribution of platinum on the carbon surface. However, no clear separation of regions with different oxidation rates is seen in Figure 3.2, indicating a good distribution (dispersion) of platinum on the carbon surfaces.

Table 3.1 Temperatures at which 50% of the sample was combusted during the heating. Results from two parallel measurements and their averages are shown.

Sample name	$T_{m(1/2)}$		Average $T_{m(1/2)}$	Average difference between $T_{m(1/2)}$ with and without Pt
	Parallel I (°C)	Parallel II (°C)	(°C)	(°C)
Pt/CB	596	531	564	
CB	740	762	751	187
Pt/MWCNT	661	-	661	
MWCNT	830	897	864	203
Pt/PlCNF	667	670	669	
PlCNF	657	687	672	3
Pt/CPCNF	692	636	664	
CPCNF	842	898	870	206
Pt/graphite	717	715	716	
graphite	920	862	891	175

The ash content obtained as average from 2-3 parallel TG measurements is seen in Table 3.2. However, TGA have shown low repeatability (deviation more than ± 13%). Therefore those results are not considered to be reliable. The precision of results of Pt/PlCNF sample was lower than other samples (± 30%). This could be caused by the highest (about 1.1%) inhomogeneously distributed impurity level, probably remains of the growth catalyst.

Table 3.2 Ash content of catalyst samples determined from average results of 2-3 thermogravimetric analyzes.

Sample name	Loading (%)	Ash content of the support (%)
Pt/CB	1.1	< 0.1
Pt/MWCNT	1.2	< 0.1
Pt/PlCNF	0.6	1.1 ± 0.3
Pt/CPCNF	1.3	< 0.1
Pt/graphite	1.1	< 0.1

The low precision of the results obtained from the TGA led to the need for an alternative method for measurement of the metal loading. Therefore, elemental analysis with ICP-MS was done. The elemental analysis has shown that all supports except for PlCNF did not contain a significant amount of typical growth catalyst metals, as presented in Table 3.3. The impurity of Ni and Cu in PlCNF sample originates from the growth catalyst used to produce this material. The problem with inhomogeneous distribution of the growth catalyst in PlCNF that led to low precision in the TGA was solved by a better mixing of the powder before some of this powder was taken out for analysis and using a larger amount of sample for the analysis (approximately 400 mg). Since Ni in the growth catalyst is catalytically active for the conversion of hydrocarbons at elevated temperatures, its effect on the propane dehydrogenation and ethene hydrogenation reactions had to be investigated. However, this impurity did not give any measurable catalytic activity in catalytic tests with Pt-free PlCNF (pages 86 and 87).

Table 3.3 Composition of the catalysts and the catalyst supports. The studied catalysts contained between 0.77 wt% and 0.84 wt% of platinum. Standard deviation is given in parenthesis. Only Pt/PlCNF contained significant amounts of metal (Ni and Cu) impurity.

Sample code	Support material	Ni wt% (SD)	Cu wt% (SD)	Fe wt%	Pt wt% (SD)
Pt/CB	carbon black	<0.001	0.003	<0.002	0.82(1.4E-02)
Pt/MWCNT	graphitized multiwalled carbon nanotubes	<0.001	0.002	<0.002	0.84 (1.8E-02)
Pt/PlCNF	platelet carbon nanofibers	0.31 (5.6E-03)	0.11 (2.8E-03)	<0.002	0.81 (1.3E-02)
Pt/CPCNF	conical platelet carbon nanofibers	<0.001	0.007	<0.004	0.77 (1.1E-02)
Pt/graphite	graphite	<0.001	0.002	<0.004	0.78 (1.6E-02)

The measured platinum loading was slightly lower than the nominal loading of 1.0% and found to be in the range 0.77-0.84% for all the tested catalysts. This deviation could be caused by an error during weighing, caused by a high hygroscopicity of $H_2PtCl_6 \cdot (H_2O)_6$ metal precursor. This hygroscopicity was high enough to turn the solid precursor into liquid in few minutes of exposure to the atmosphere. Alternatively, some Pt could be lost by insufficient anchoring to the support. It is common that the actual loading is lower than the calculated loading because some loss of Pt in the metal deposition process [128]. This loss depends on both the surface area of the support and the electrostatic interaction between the platinum colloids and the carbon support in the synthesis process. In the

polyol method, the relation between the actual loading and the nominal loading is controlled by pH [51]. In a basic suspension, the negatively charged (glycolate anion stabilized) platinum particles are repelled from each other and from the (negatively charged oxygen-containing carbon) support. At lower pH, the repulsive forces become weaker and the particles will be deposited on the support. If the pH is too low, the actual loading on the support will get closer to the nominal, at the cost of particle dispersion. The relative value of the electrostatic interaction can be estimated by measuring the isoelectric point of the carbon supports in a solution with a similar composition to the solution used for the metal deposition. The pH during the deposition of platinum colloids was between pH 3.1 and pH 3.3. Zeta potential graphs are presented in Figure 3.3 and the estimated IEPs are presented in Table 3.4. As seen from both Figure 3.3 and Table 3.4 all the tested supports had positive zeta potentials at the platinum deposition pH and this is favorable for the interaction between the negatively charged platinum colloids [51] and the support.

CB (XC-72R) has IEP around 5 in aquatic suspension according to literature [134]. Here the IEP was measured in ethylene glycol/ethanol/H_2O solution similar in composition to the solution used for Pt deposition. Nevertheless, the measured IEP for CB was found to be close to the literature data. All other tested carbons had IEP around 5.0 ± 0.3 and this indicates that none of the tested supports had a high concentration of acidic functional groups on their surface. This is in agreement with results obtained by FTIR spectroscopy (page 67). All the tested supports had IEP above the deposition pH, as seen in Table 3.4 and the carbon surface had a positive zeta potential during the deposition of platinum.

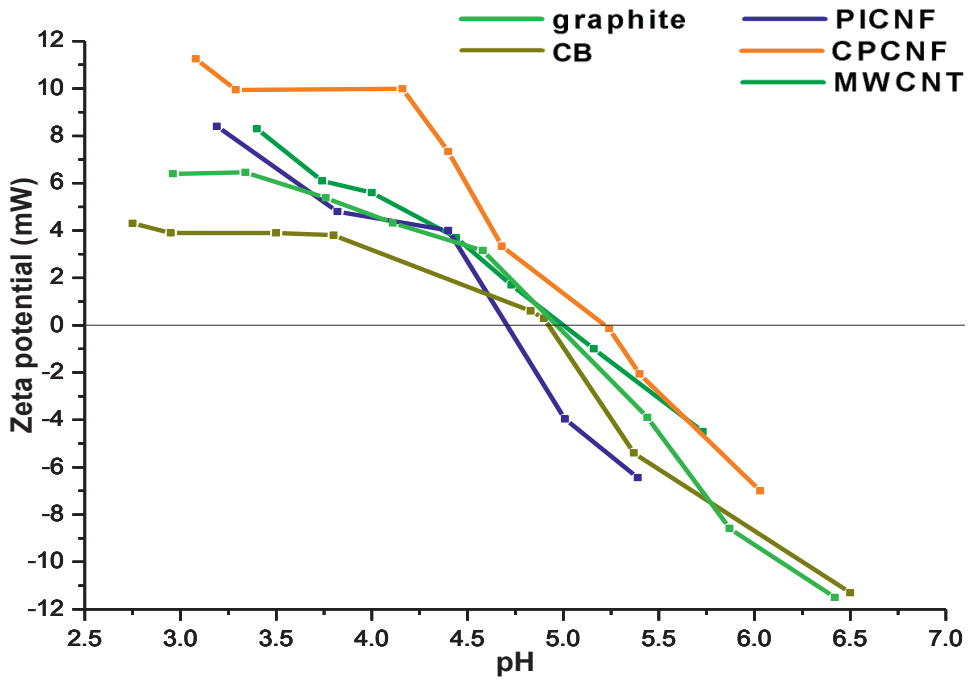

Figure 3.3 Dependence of zeta potential of the carbon supports on the pH. All the tested carbon materials had IEP around 5.0 ± 0.3.

Although the concentration of the oxygen-containing groups was low, the obtained results indicate that they were present because the isoelectric point is below 7. Oxygen-containing groups can form at edges or other defects by exposure to air. For example sites with higher concentrations of edge-localized unpaired electrons are unstable and will easily undergo additional reactions at many preparatory conditions [135]. However, the measurement of IEP has shown that the concentration of those groups was too low to cause a negative surface charge of carbons at the Pt deposition conditions and they did not affect the dispersion of platinum by repulsive electrostatic forces between the platinum colloids and the supports.

Table 3.4 The Pt deposition pH and IEP for the studied catalysts.

Samples	Deposition pH	Isoelectric point (IEP)
CB	3.2	4.9
MWCNT	3.3	5.0
PlCNT	3.1	4.7
CPCNF	3.2	5.2
graphite	3.2	5.0

The results from N_2 physisorption are presented in Table 3.5. The BET surface area of catalysts with high surface area supports, i.e. Pt/CB and Pt/PlCNF, is slightly less when compared with Pt-free carbons (CB and PlCNF). A small reduction of less than 1% is expected because catalyst contains both carbon and platinum as opposed to only carbon (and small amounts of possible impurities) in Pt-free supports. Nevertheless, the surface area of Pt/CB and Pt/PlCNF catalysts was 5% and 3% less than for CB and PlCNF supports respectively. No measurable change in the surface area was observed for low surface area supports, CPCNF and graphite, probably because such changes were below the detection limit. The reduction of the surface area can be explained by clustering of support particles during drying. It is also possible that some of the reduction was caused by the blockage of micropores by Pt or support particles, reducing their availability to N_2 molecules.

The CB support has the highest t-plot micropore volume. When compared with the cumulative pore volume, as determined by BJH, about 21% of the pore volume in CB is originating from the micropores. This is the highest fraction of micropores among the tested carbon materials. PlCNF shows similar cumulative pore volume as CB, but the fraction of micropores is much lower in this material. Instead, more than 95% of its pore volume consists of mesopores.

Therefore, the adsorption-desorption isotherms for PlCNF have a clearly visible hysteresis as seen in Figure 3.4. Similar but less clear hysteresis is visible for CB and MWCNT indicating the presence of mesopores in those materials.

Table 3.5 Surface area and porosity of the catalysts and the catalyst supports. Platinum deposition resulted a small decrease of the surface area, while no significant change in the pore volume was detected.

Samples	BET surface area (m^2/g)	Pore Volume[1] (cm^3/g).	Micropores t-plot (cm^3/g)
CB	230 ± 2	0.18	0.037
Pt/CB	218 ± 2	0.18	0.035
MWCNT	73.7 ± 0.4	0.11	0.001
Pt/MWCNT	72.8 ± 0.4	0.12	0.001
PlCNF	186 ± 0.5	0.18	0.008
Pt/PlCNF	180 ± 0.4	0.18	0.007
CPCNF	19.9 ± 0.2	0.03	0.000
Pt/CPCNF	20.3 ± 0.1	0.03	0.001
graphite	9.35 ± 0.05	0.01	0.000
Pt/graphite	9.40 ± 0.02	0.01	0.000

Note: 1. BJH Adsorption cumulative volume of pores between 17 Å and 3000 Å diameter (cm^3/g).

The deposition of platinum did not have any significant effect on the shape of N_2 physisorption isotherms, as seen in Figure 3.4. Observed isotherm shapes for CB and PlCNF can be described as Pseudo-Type II isotherms by the IUPAC

classification [136]. The Type II isotherms are commonly a result of monolayer-multilayer adsorption at nonporous or macroporous adsorbents. The transition from monolayer to multilayer is seen as a reduction of the slope during the adsorption. This point was termed Point B by Brunauer, Emmet, and Teller [137]. For CB and PlCNF, this is seen in at P/P_0 between 0.03 and 0.05. The difference between Type II and Pseudo-Type II isotherms is the presence of a hysteresis in the multilayer region of the latter. The mesopores responsible for this hysteresis are often described as "slit-shaped" [136]. According to the IUPAC classification, the observed hysteresis is type H3 [138]. This means that the mesopore size distribution is wide [139]. In case of MWCNT, PlCNF, and CB those pores are probably voids between different nanofibers or carbon particles.

The Point B is less clear for graphite, CPCNF, and MWCNT. Therefore, those materials exhibit an intermediate isotherm type between Pseudo-Type II and Type III. Those isotherms are convex to the P/P_0 axis and do not display a clear transition from the monolayer to the multilayer adsorption. Type III isotherms are caused by a weak adsorbent-adsorbate interaction as compared with the adsorbate-adsorbate interaction. This isotherm type is not common and can be observed for example with water vapor adsorption on pure nonporous carbons [138]. A small deviation from convex shape towards a stepwise isotherm is seen in MWCNT and CPCNF at high Y axis magnification. This is typical for Type VI isotherm where the multilayer adsorption is stepwise, and the filling of each layer is distinct from each other [138]. This property of CNFs has been reported in the literature [79].

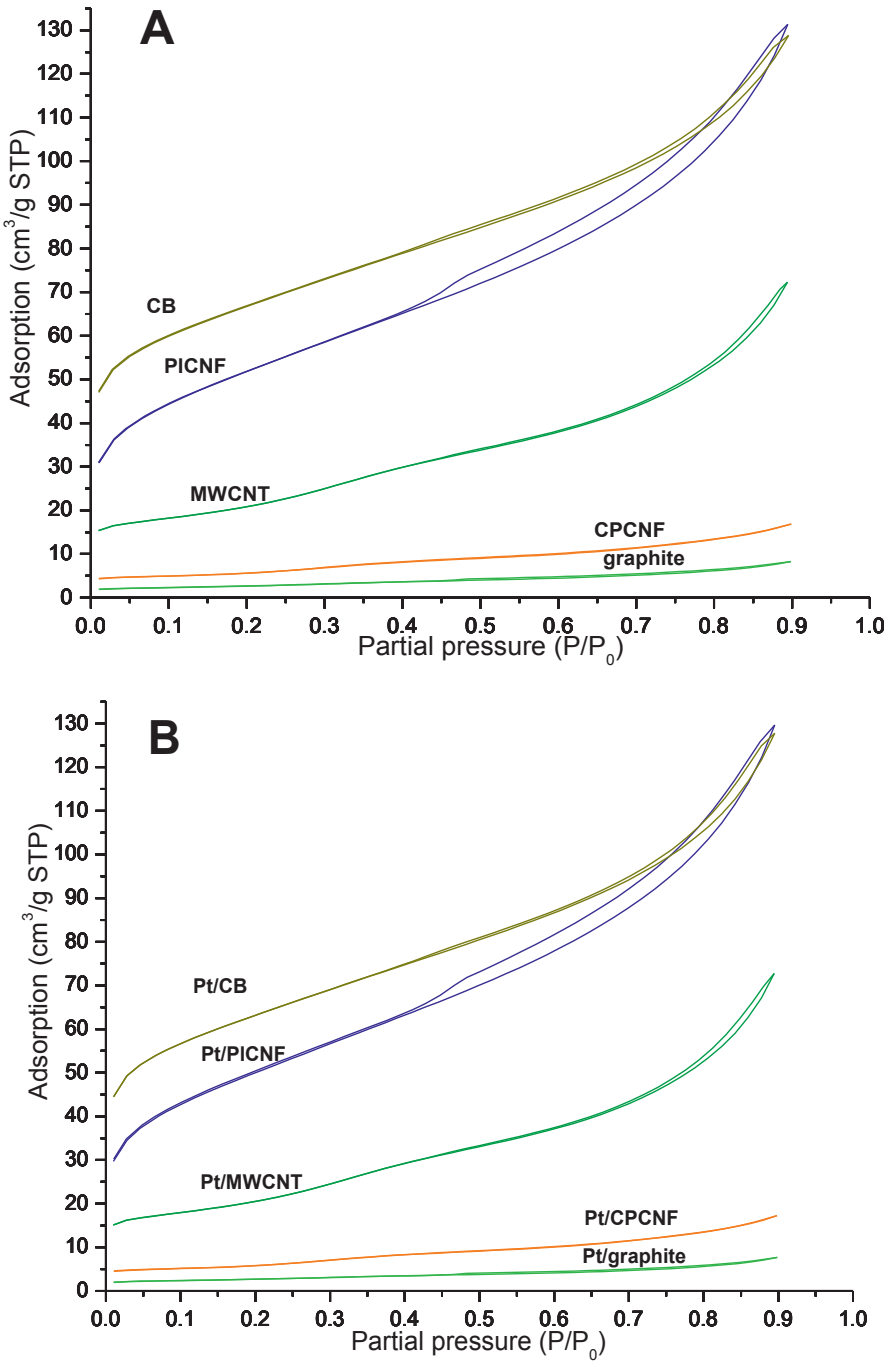

Figure 3.4 Adsorption and desorption isotherms of catalyst supports (A) and catalysts (B).

The SEM image in Figure 3.5 shows that CB consists of aggregated carbon particles. As seen in the TEM image in Figure 3.6(A), the distribution of platinum nanoparticles on CB was not entirely homogeneous in spite of a relatively smooth TG curve obtained during oxidation of this catalyst in air (pages 46 and 47). This could be due to insufficient sonication during the catalyst preparation. A uniform distribution is harder to achieve on CB than on other supports in this work because CB has high meso- and micro- porosity as seen from N_2 physisorption results (page 54). However, CB has a higher surface area that provides sufficient distance between particles to avoid agglomeration, so this non-uniform distribution is not expected to have a significant effect on the catalytic properties of this material.

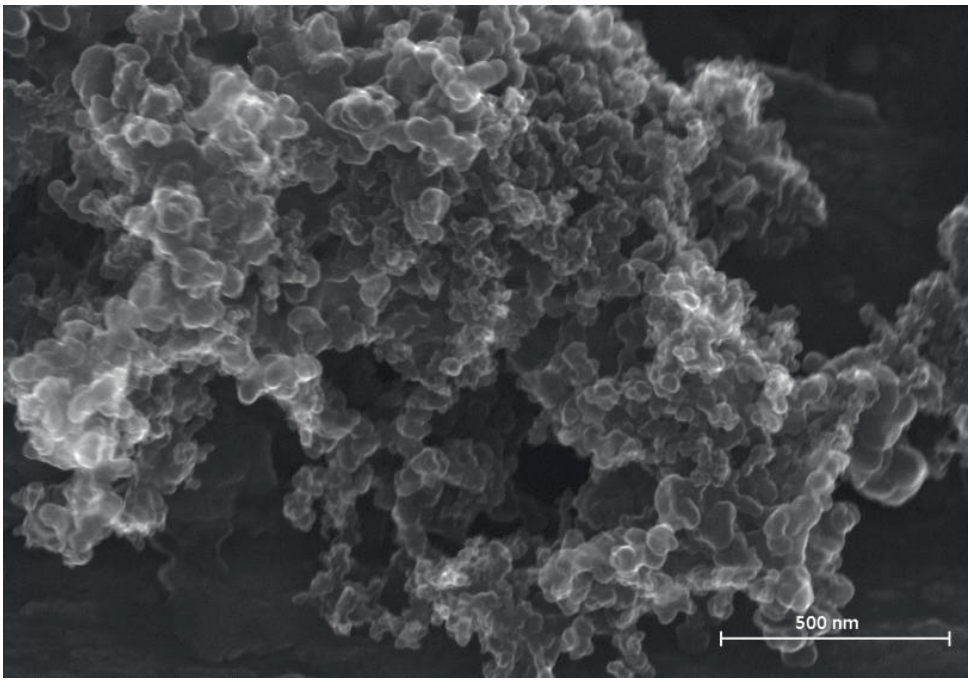

Figure 3.5 SEM image of Pt/CB. The image shows clustered carbon black particles.

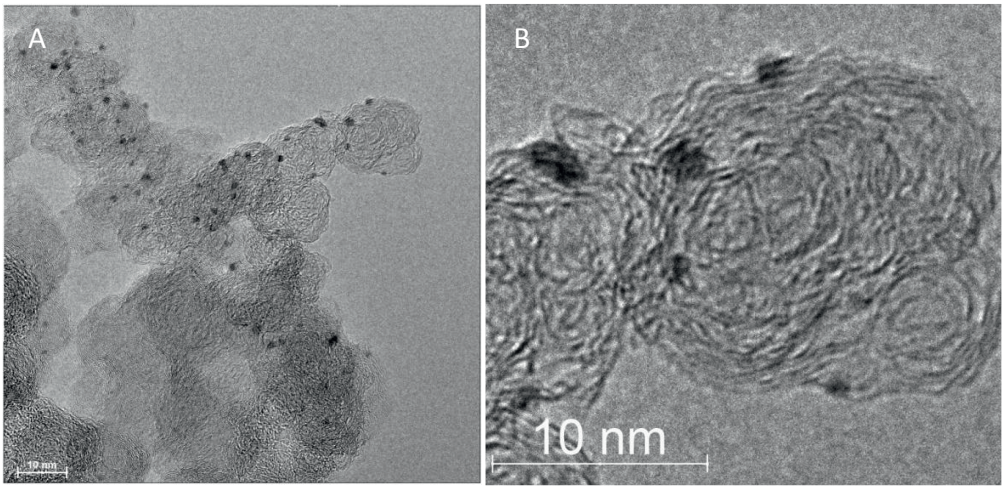

Figure 3.6 The TEM image A shows that Pt metal particles are not distributed homogeneously on the sample surface. Image B shows that Pt particles on the surface are predominantly spherical or oval in shape.

The majority of the carbon nanotubes have diameters of 20-50 nm as seen in Figure 3.7. The multiwall structure of MWCNT support was confirmed by TEM, as seen in Figure 3.8. The TEM images of Pt/MWCNT show that CNTs have closed tips, so the void inside the CNTs was not accessible to the platinum colloids.

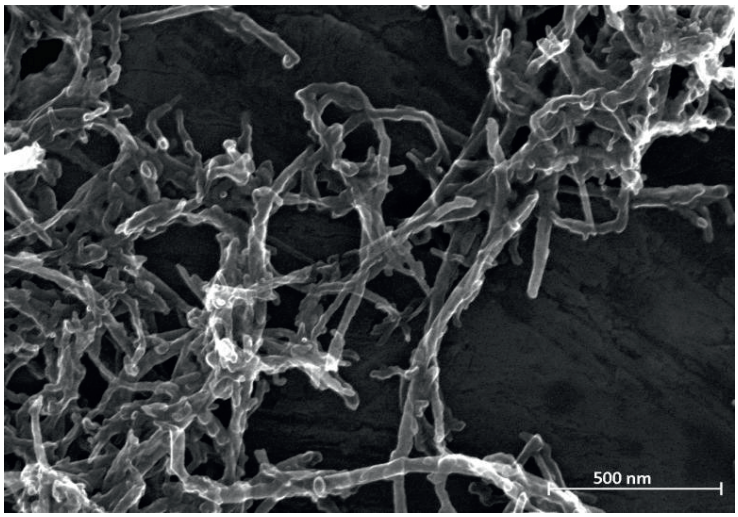

Figure 3.7 SEM image of Pt/MWCNT showing clustered carbon nanotubes.

The surface of carbon nanotube in Figure 3.8A seems to be different in the upper and lower part the tube. While it entirely consists of parallel layers above, it is seen that some pyrolytic secondary carbon is deposited at the downside of the tube. Such overlayers with pyrolytic carbon are usually undesired because they can significantly affect the surface properties of the material [3]. Closer inspection from other regions of the sample has shown that the majority of the nanotubes in this material do not have such overlayers. Therefore, this sample should exhibit MWCNT surface properties. However, the presence of the pyrolytic carbon cannot be neglected because such carbon can have more anchoring sites for Pt deposition than the clean MWCNT surface.

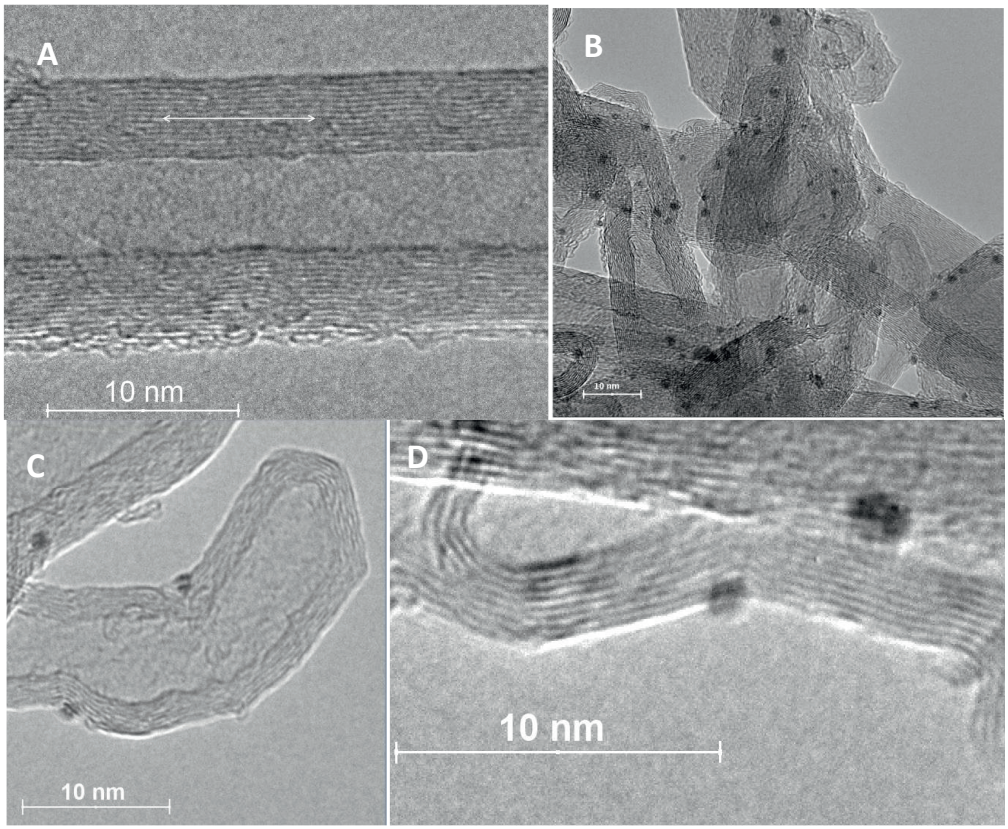

Figure 3.8 The parallel multiwalled tube structure is clearly seen in the TEM images A and D. The TEM images B, C, and D show the platinum nanoparticle distribution on MWCNTs.

The SEM image in Figure 3.9 shows that the platelet fibers were not as well defined as MWCNTs or CPCNFs. They have irregular shapes and lower aspect ratio. The TEM images, as seen in Figure 3.10, confirm the platelet structure of the fibers, although many of the layers are not perpendicular to the principal axis. Some regions with undefined crystallinity exist in this sample, but the majority of the platinum particles are deposited on the graphitic edges on the surface of nanofibers. The deposited platinum particles have a flat shape, as seen when the particles are viewed at the edge of the fibers in Figure 3.10(B). This indicates stronger metal-support interaction than what was observed for CB and possibly MWCNT. Similar effects of the metal-support interaction between the platinum particles and platelet carbon nanofibers have been described in the literature [74; 93].

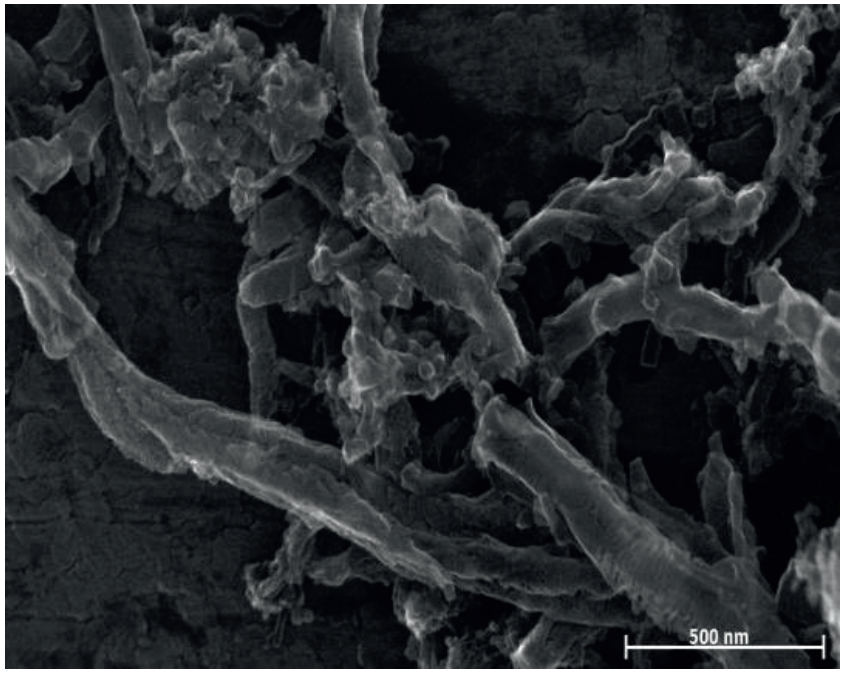

Figure 3.9 SEM image of Pt/PlCNF showing that the platelet fibers had a low aspect ratio and irregular width.

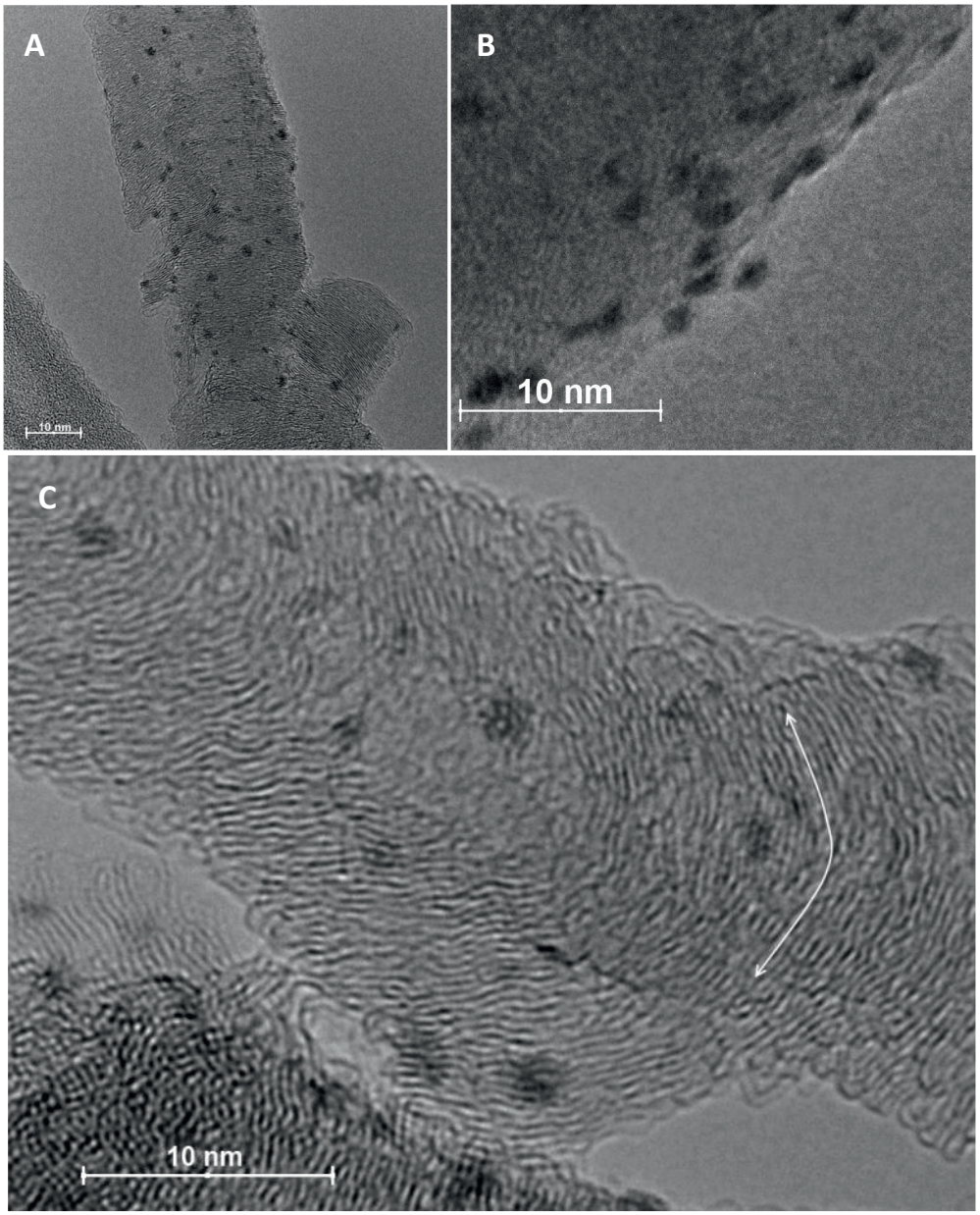

Figure 3.10 The TEM images A and C shows that PlCNFs consist of graphitic layers, but a large fraction of the layers are not perpendicular to the principal (fiber direction) axis. Image B shows that platinum particles deposited on the surface of the fiber have elongated shape.

The SEM images of CPCNF, as seen in Figure 3.11, show that the majority of the carbon nanofibers had high aspect ratio and diameters between 50 nm and 150 nm. However, very little information was obtained from SEM on the inner structure of the fibers.

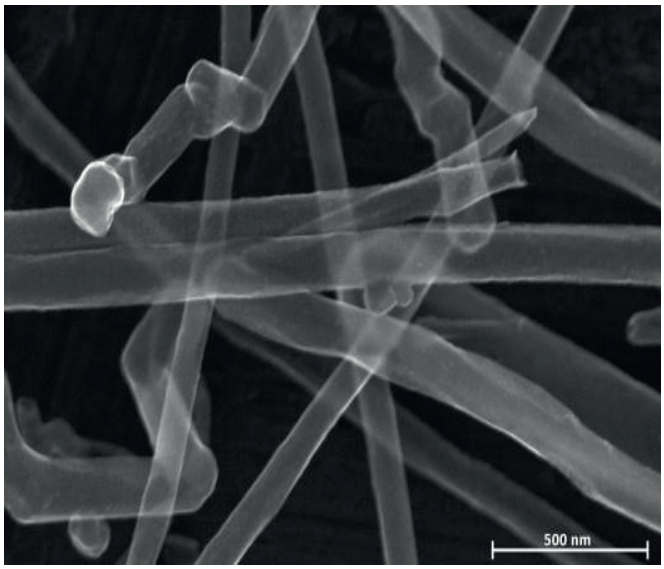

Figure 3.11 SEM image of Pt/CPCNF showing that fibers have high aspect ratio and diameters between 50 nm and 150 nm.

The TEM images, on the other hand, were much more informative and have shown that this sample consists of at least three different types of hollow fibers. There are bamboo-type of fibers, i.e. fibers with closed interior compartments [140], fibers with cavities in their walls, and fibers with a stacked-cup structure. The last type is most common and, as seen in Figure 3.12, the fibers consist of a parallel layer on the outside and tilted stacked-cup layer inside. This is important, as the outer and inner surface of the fibers will exhibit different properties. This structure has also been observed in other commercial CNFs by other groups [91]. The inner cavity of those fibers is accessible to the platinum nanoparticles and the majority of platinum nanoparticles are deposited there.

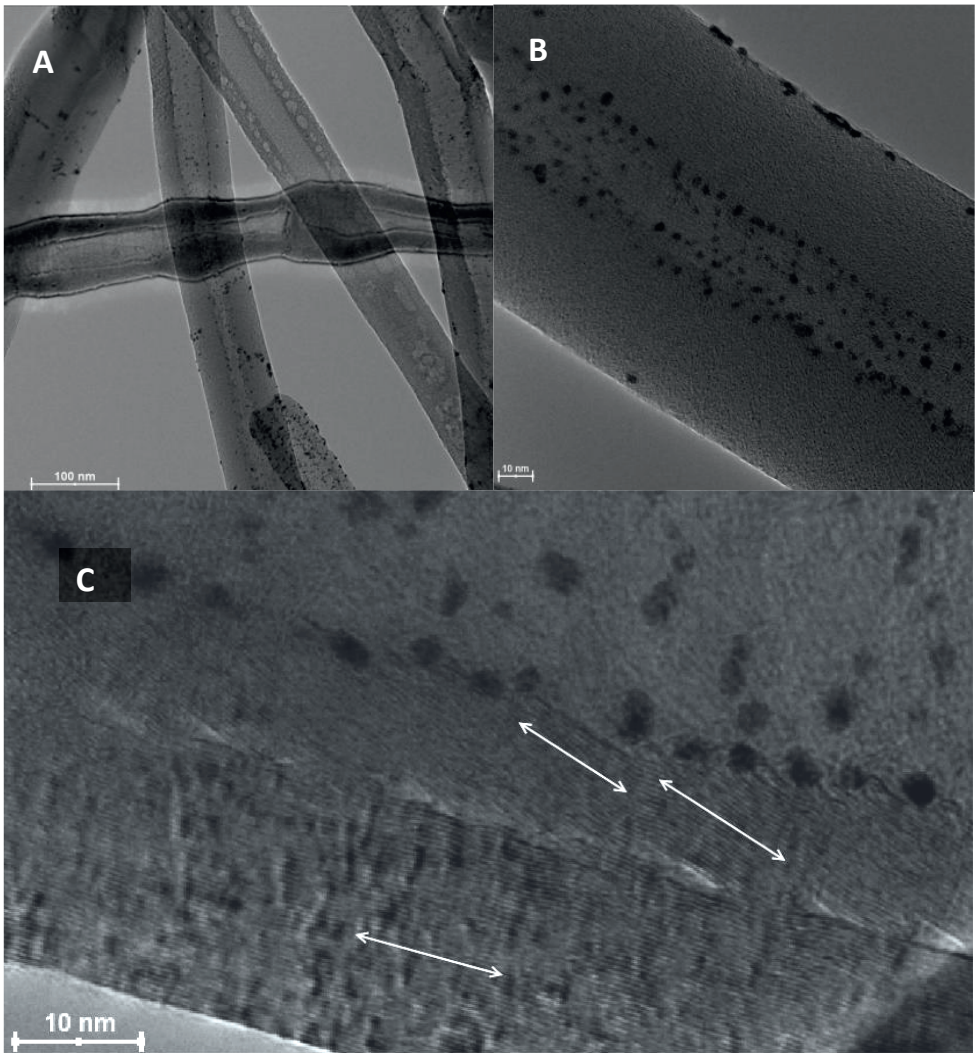

Figure 3.12 TEM images show that the sample consists of at least three different types of hollow fibers, as seen in image A. Some of the Pt particles are located inside the hollow fibers, as well as on the fiber surface (B). Image C shows conical platelet fibers inside a multiwalled structure.

The ability of metal particles to deposit on the inner surface of carbon nanofibers has been previously demonstrated by Winter et al. [141] using an ion adsorption method and HNO_3-treated CNFs and later by Li et al. [91] using modified polyol method and CNFs oxidized by HNO_3 and H_2SO_4 containing

solution. In this work, the particles that are deposited on the outer surface of those fibers seem to agglomerate easily, indicating low interaction and few anchoring sites. On the other hand, particles on the inner surface of the fibers seem to agglomerate less and this indicates a larger concentration of anchoring sites. The tilted layers on the inner surface of CNFs are better suited for metal particle deposition and this could be caused by a better interaction between the edges of the layers containing dangling bonds and the platinum particles.

Figure 3.13 shows that the graphite sample consist of large graphite particles (<20 μm according to the supplier) and the platinum nanoparticles were deposited on their surface. Low surface area of the graphite support led to extensive agglomeration of platinum particles and larger particles consisting of several clustered particles can be observed with SEM, seen as small bright dots on the graphite surface in Figure 3.13. As seen in Figure 3.14, there are some regions with a higher concentration of particles and where particles are probably deposited on edges of graphite layers. This is expected as the edges and other defects are more likely to provide an anchoring site to metal particles.

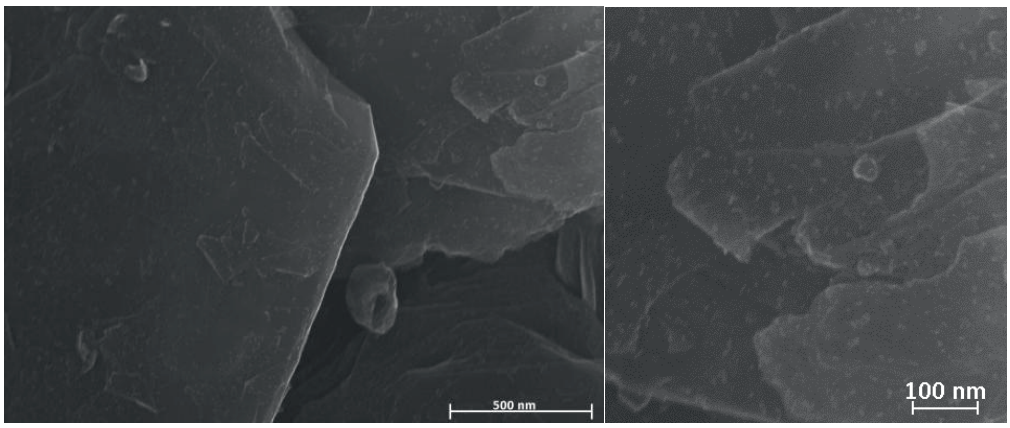

Figure 3.13 SEM images showing relatively large graphite particles covered by platinum particles.

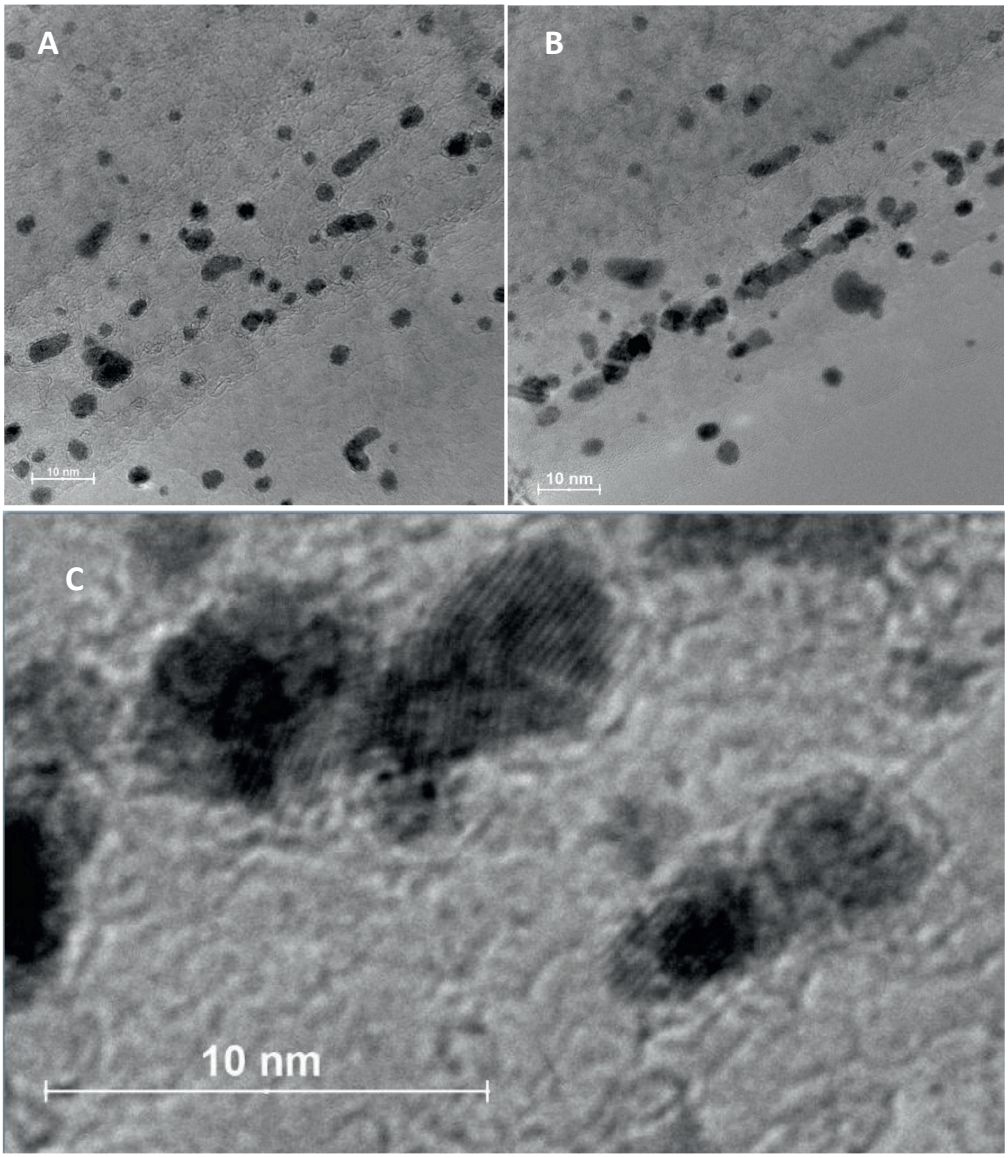

Figure 3.14 Agglomerations of platinum nanoparticles on the graphite surface. The elongated shape of agglomerates as, seen in image A and B, indicates that platinum particles are anchored along the edges of graphite layers. Image C shows the crystal structures of some of the particles.

Unlike particles deposited on other supports studied in this thesis, some of the particles seen in Figure 3.14(C) seem to be highly crystalline with their surface

structure visible at applied resolution. This could be caused by larger particles on the Pt/graphite than other studied catalysts and a better metal-support contrast of the images.

The FTIR results (Figure 3.15) do not show any significant presence of oxygen-containing functional groups except for -OH. The typical oxygen-containing functional groups found on carbon surfaces are anhydrides, ketones, aldehydes, esters, quinones, carboxylic acids, ethers, lactones, and phenols. Anhydrides have been reported by Shin et al. [142] and references therein, to give a band at 1880-1740 cm^{-1}. The stretching mode of ketonic C=O groups of ketones, aldehydes and esters would appear at 1740 cm^{-1} if those groups are not conjugated with a double band or aryl group [143]. Conjugated ketones or quinones appear at 1670-1660 cm^{-1} [142; 144; 145]. Aromatic carboxyl acid group would give a band in 1700-1680 cm^{-1} region and are affected by different peripheral functional groups, and the non-aromatic carboxyl acid groups have been reported to give a band at 1712 cm^{-1} [142]. Ether type structures would give C-O stretching vibration bands at 1245 cm^{-1} and 1160 cm^{-1} [143]. Lactones have been reported to appear at 1740-1710 cm^{-1} and 1264-1260 cm^{-1} and the phenolic groups would appear in the 1200-1100 cm^{-1} region [142; 143].

The broad band at 3434 cm^{-1} can be assigned to hydroxyl stretching vibrations of the HO- group and adsorbed water, as observed by Gomez-Serrano et al. [143] and Puziy et al. [146]. The broadness of this band indicates involvement of the hydroxyl groups in hydrogen bonding. Bands at 2955 cm^{-1}, 2921 cm^{-1}, and 2854 cm^{-1} can be assigned to CH_3 and CH_2 stretching vibrations as observed by Gomez-Serrano et al. [143], Puziy et al. [146] and Russo et al. [147].

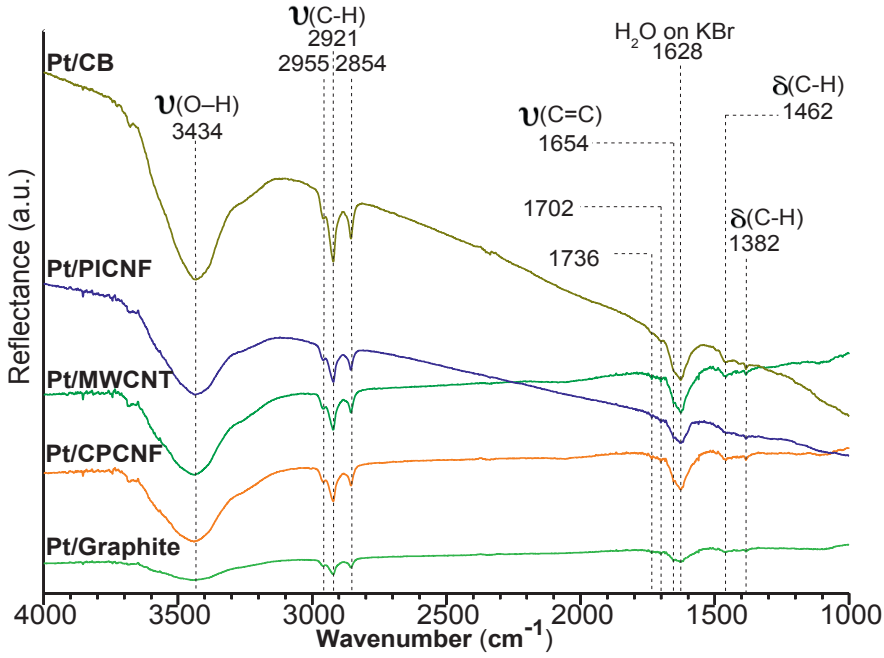

Fig. 3.15 FTIR spectra of the catalysts. The reflectance axis has arbitrary units for each sample. Therefore, the absorption peaks are for qualitative comparison. Letter υ denotes stretching modes and δ denotes in-plane bending modes. All spectra have shown similar absorption bands.

Two very weak bands, at 1738 cm^{-1} and at 1702 cm^{-1}, have been observed for all supports, as seen in Figure 3.15. However, those bands are too weak to firmly identify them as ketone or carboxyl groups. The band at 1628 cm^{-1} can be assigned to adsorbed water on the KBr. Teng et al. [148] have observed this band at 1630 cm^{-1}. A small shoulder of this band can be observed at 1654 cm^{-1} and can be attributed to C=C stretching at terminal olefinic bonds [143]. The band at 1462 cm^{-1} can be attributed to the asymmetrical bending (scissor) mode of CH_3 and CH_2 groups and has been reported by Gomez-Serrano et al. [143] and Teng et al. [148]. The band at 1382 cm^{-1} can be assigned to CH_2 and CH_3 bending vibrations, as observed by Gomez-Serrano et al. [143] and Russo et al.

[147]. Pt/CB and Pt/PlCNF background spectra are sloping down to lower wavenumbers. This could be due to scatter from sample particles causing deeper light penetration at the longer wavelengths (lower wavenumbers). The presence of bending and stretching modes of C-H can be clearly observed for all samples indicating that all supports, including carbon nanotubes and fibers contain defects. The degree of disorder in carbon supports can be assessed from Raman spectra, presented in Figure 3.16.

The FTIR technique is not very sensitive for characterization of materials with small amounts of functional groups [3], and the absence of any definite absorption bands from the oxygen-containing functional groups does not provide evidence that those groups are absent. Therefore, to ensure that acidic functional groups do not reduce the isoelectric point enough to cause an electrostatic repulsion between the Pt particles and the supports during the metal deposition, a measurement of the zeta potential was done (page 52).

The Raman spectra of the catalysts are presented in Figure 3.16. The spectra of the platinum-free supports were also collected (not shown), but they were similar to the spectra of the catalysts in Figure 3.16.

Since Raman spectra of carbon materials are usually composed of several overlapping bands, a deconvolution is commonly used to obtain more information from those spectra. There are no standard procedures for the deconvolution of Raman spectra of carbon materials and different research groups have reported different number of bands and bandshapes (Gaussian, Lorentzian, Breit-Wigner-Fano, pseudo-Voigt, etc.) [119; 149; 150; 151; 152; 153; 154; 155] in the first order region of Raman spectra (1000-1800 cm^{-1}). In this work, five bands in the first order region were fitted as described in several other studies [118; 119; 120].

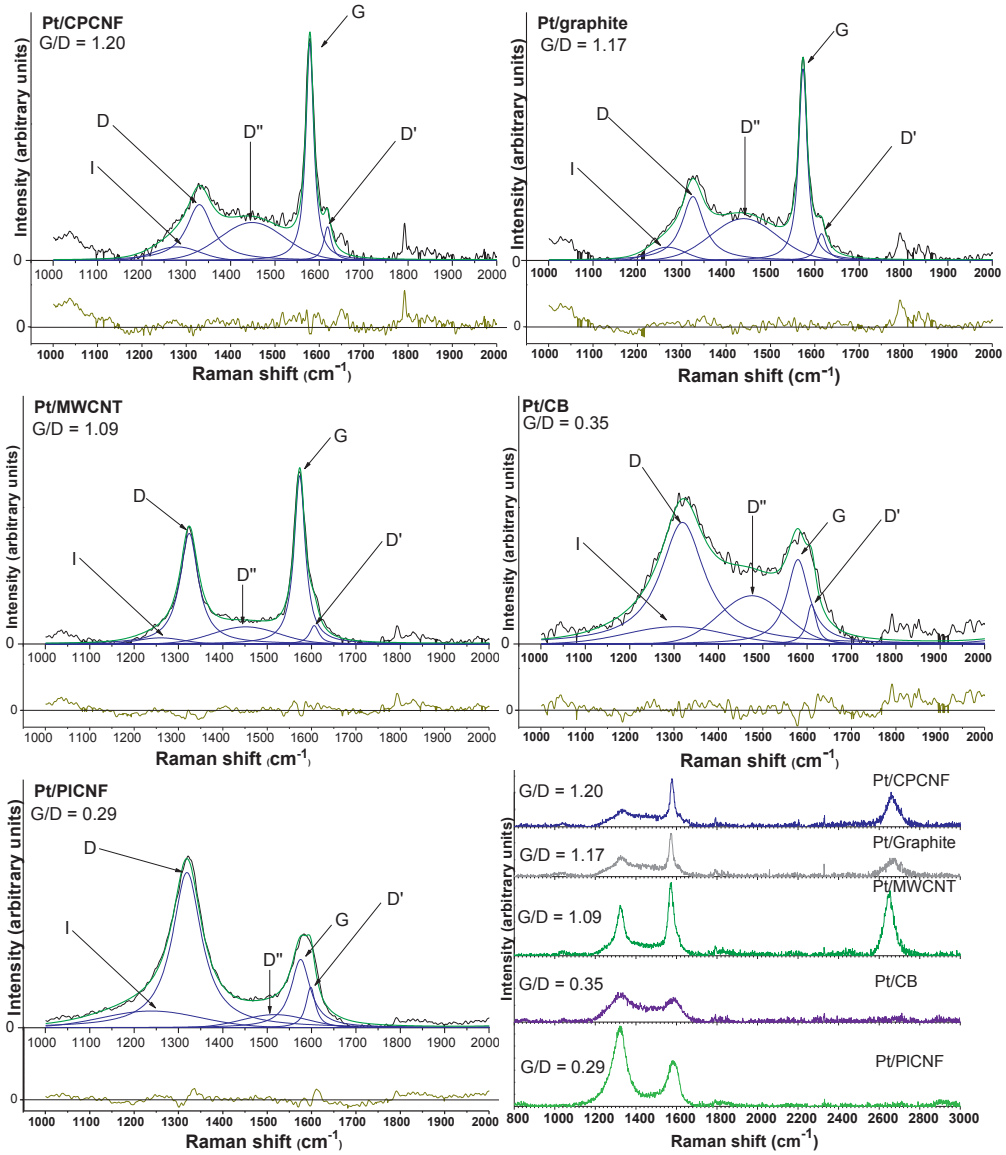

Figure 3.16 Raman spectra of carbon-supported catalysts. The G/D band ratio shows that Pt/PlCNF had the highest degree of disorder, while Pt/CPCNF had the highest degree of order.

The most important bands in the five band fitting procedure of the first order region of carbon spectra are I, D, D'', G, and D':

- The I band can be related to disorder in the graphitic lattice or polyene-like structures [120; 156]. The maximum of this band was observed in the 1230-1304 cm^{-1} range.

- The maximum of the D band is observed in the 1319-1330 cm^{-1} range. The position of this band is dependent on the type of laser used and moves to lower Raman shift with increasing laser wavelength [149; 157; 158]. Choi et al. [159] have reported this band in the 1350 cm^{-1} range for MWCNTs when 633 nm laser was used. Vallerot et al. [119] have observed this band in pyrocarbons at 1330 cm^{-1} using the same type of laser. This band is associated with a disorder of carbon and stems from a double resonance process involving a phonon and defects such as edges, vacancies or dopants [120].

- The D'' band has been attributed to the presence of amorphous carbon [150], [120]. It was observed in the 1440-1518 cm^{-1} range.

- The first order Raman allowed G band originates from the stretching of the C-C bond and is common for all sp^2 carbon materials. This band is observed in 1573-1579 cm^{-1} range and is associated with the degree of graphitization order of the carbon. This band is independent of the laser wavelength for graphitic samples, but as reported by Ferrari et al. [149], this band can move to lower Raman shift with increasing laser wavelength in amorphous samples. Choi et al. [159] have reported this band in the 1582 cm^{-1} range for MWCNTs when a 633 nm laser is used.

- The maximum of the D' band is observed in 1600-1619 cm^{-1} range. This band is overlapping with the much stronger G band and is disorder related [151; 119]. Choi et al. [159] have reported this band in the 1610 cm^{-1} range for MWCNTs, while Vallerot et al. [119] have observed this band in heat treated pyrocarbons at 1620 cm^{-1}.

In the second order region, a band called 2D is observed for some of the studied catalysts. This band is also known as G' band [157; 160] and is observed in 2645-2674 cm^{-1} range. This is the second order of the D band [160]. As with D band, the position of this band is dependent on laser wavelength. However, this band does not require a defect for activation. The 2D band was not observed for samples with low graphitization degree (Pt/PlCNF and Pt/CB), while it was clearly visible in more graphitic samples (Pt/MWCNT, Pt/graphite, and Pt/CPCNF). Its intensity can be related to spatial uniformity in the graphitic plane or the uniformity of interlayer spacing [120]. The suppression or the absence of 2D band in disordered carbons has been observed by Ferrari [160] and by McEvoy et al. [120].

The ratio of the intensity of the G band and the D band (G/D) is often assumed to be proportional to the crystallite size (L_a) and is commonly used to assess the extent of graphitization degree of carbon materials [150; 161; 152; 153]. However, this value is only recommendatory since simple G/D comparison has many uncertainties, including a nonlinear dependence on the crystallite size, when the crystal size is below 2 nm [154] and dependence on excitation wavelength [157]. Based on the G/D band ratio, we observe the following increasing degree of disorder:

Pt/CPCNF(1.20)>Pt/graphite(1.17)>Pt/MWCNT(1.09)>Pt/CB(0.35)>Pt/PlCNF(0.29)

The high crystallinity of CPCNF is not surprising since this sample has been thermally treated to 2900°C in inert atmosphere according to the supplier (page 30).

The lower G/D ratio of PlCNF compared to CB seemingly indicates that PlCNF is more disordered than carbon black, which is known for poor crystallinity. The TEM results (Figure 3.10, page 61) show that PlCNF although having many defects, consists of graphitic layers on top of each other. Hence, it should contain a higher concentration of sixfold aromatic rings. For disordered carbons, the intensity of the D band becomes proportional to the probability of finding a sixfold ring in a given area while the G band does not require a sixfold ring. Therefore, high D band in distorted carbons can indicate ordering, which is the opposite of what is observed for more graphitic carbons [149; 155].

3.2. Dispersion of platinum

The platinum colloid deposition (modified polyol) method is suitable for studying the effect of different supports because the Pt colloids are premade in a solution. Their formation is therefore not affected by the support. Sintering of the particles can still occur during and after the deposition (page 64 and 75), but the initial particle size is expected to be the same. Likewise, if Pt particles are formed in a solution, then this formation of the particles can not affect surface chemistry of the supports. A study by Coloma et al. [53] has shown that reduction of hexachloroplatinic acid on a carbon support can cause an introduction of oxygen-containing functional groups. Since functional groups can have an effect on catalytic properties of the samples, it is advantageous that the main step of the platinum reduction is done before the deposition on the

support. Figure 3.17 shows the color change as platinum is reduced by ethylene glycol and Pt colloids are formed in an alkaline solution.

Figure 3.17 During the heat treatment, the Pt colloids are formed from a solution. This is observed as a color change from yellow H_2PtCl_6 solution (left) to dark platinum colloid suspension (right).

One of the most important parameters of supported metal catalysts is the dispersion of the catalytic metal because it can affect the utilization of the catalytic metal and have an effect on structure sensitive reactions. Therefore, the metal dispersion of the catalysts was measured by chemisorption, cyclic voltammetry, and TEM. Figure 3.18 shows the results of the dynamic chemisorption measurements over CB support and a Pt/CB catalyst sample. No hydrogen adsorption activity was measured over the bare support. When Pt/CB was heated in a helium flow, hydrogen evolution was detected with a maximum at 370 °C. Similar hydrogen evolution at 350 °C was observed by Jiang et al. [162], and it was attributed to desorption of hydrogen that was adsorbed on the sample due to the spillover effect.

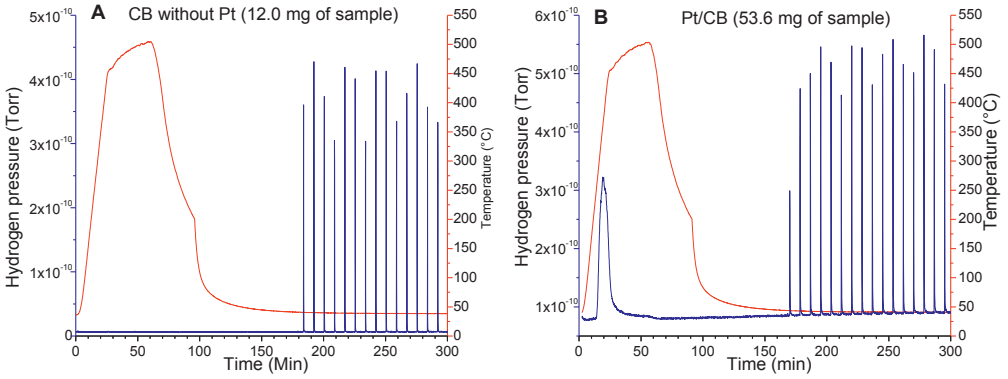

Figure 3.18 Dynamic chemisorption measurement over the CB support (A) and the Pt/CB sample (B). No H_2 adsorption was detected over CB, while only small amounts of H_2 were adsorbed on Pt/CB.

In spite of a desorption of significant amounts of hydrogen during heating, only a negligible amount of hydrogen was adsorbed during the H_2 pulses at 40 °C. Similar results were obtained for Pt/graphite and Pt/CPCNF, while Pt/MWCNT and Pt/PlCNF were not tested. The amount of adsorbed or desorbed hydrogen was not reproducible and could not give quantitative estimates of the platinum dispersion. A similar problem was observed with the static chemisorption. Neither the static volumetric nor the dynamic chemisorption yielded reproducible results. The difficulty of measuring metal dispersion by hydrogen chemisorption on metal/carbon catalysts has been observed by other authors [163; 164].

The TEM results were more informative, and the TEM images are presented in Figures 3.6, 3.8, 3.10, 3.12, and 3.14 (pages 58, 59, 61, 63, and 65 respectively). The results of the Pt particle size measurements are shown in Figure 3.19 and Table 3.6. As expected, catalysts with low surface area supports (page 54), graphite and CPCNF, had comparatively large average metal particle sizes of 3.1 nm and 2.4 nm respectively. On the other hand, the supports with higher surface areas, MWCNT, PlCNF, and CB, had smaller average Pt particle size of

1.5 - 1.6 nm. The larger average particle size on graphite and CPCNF than on other supports was caused by a small fraction of large particles, seen as a tail above 5 nm in the particle size distribution histogram in Figure 3.19. Since all catalyst samples in this thesis were prepared from the same colloidal platinum suspension, it is reasonable to assume that large particles arise from agglomeration of smaller particles. For example for graphite, the increase in the number of particles larger than 1.5 nm came at the expense of particles in the 0-1.5 nm size range. This gives the size distribution histogram a skewed shape. Another indication of Pt particle agglomeration on Pt/graphite is seen directly from the TEM micrographs presented in Figure 3.14 (page 65). The elongated agglomerated particles are observed along the graphite flake edges. This could be caused by scarcity of other anchoring sites on the graphite surface. A similar, but smaller tail than for Pt/graphite is observed for Pt/CPCNF. The majority of observed particles with size above 5 nm were observed on the outer surface of the fibers. On the other hand, a majority of the particles inside the hollow fibers were between 1.0 nm and 3.5 nm in diameter. The smaller particles on the internal surface of the fibers than on the external surface indicates more favorable adsorption effects on the tilted layers on the internal surface of the fibers, as seen in Figure 3.12 (page 63).

The Pt particles on PlCNF were well dispersed with an average particle size of 1.5 nm. This indicates little agglomeration, which is expected since PlCNF had high BET surface area (page 85) and many defects (pages 60-61 and pages 69 and 73) that can act as anchoring sites. No particles below 0.5 nm have been observed, but this could be due to limited resolution, rather than an absence of those particles. Thus, it is possible that the true average particle size was below 1.5 nm. As with Pt/PlCNF, Pt/MWCNT had well-dispersed particles with little agglomeration and an average particle size around 1.5 nm. Similar average

particle size was observed for Pt/CB. In contrast to Pt/graphite and Pt/CPCNF, the high surface area samples did not show any significant tail and the agglomeration was much less. Similar dispersion of platinum on the high surface area supports indicates that the average particle size of platinum on those supports probably approached the average particle size in the colloid suspension.

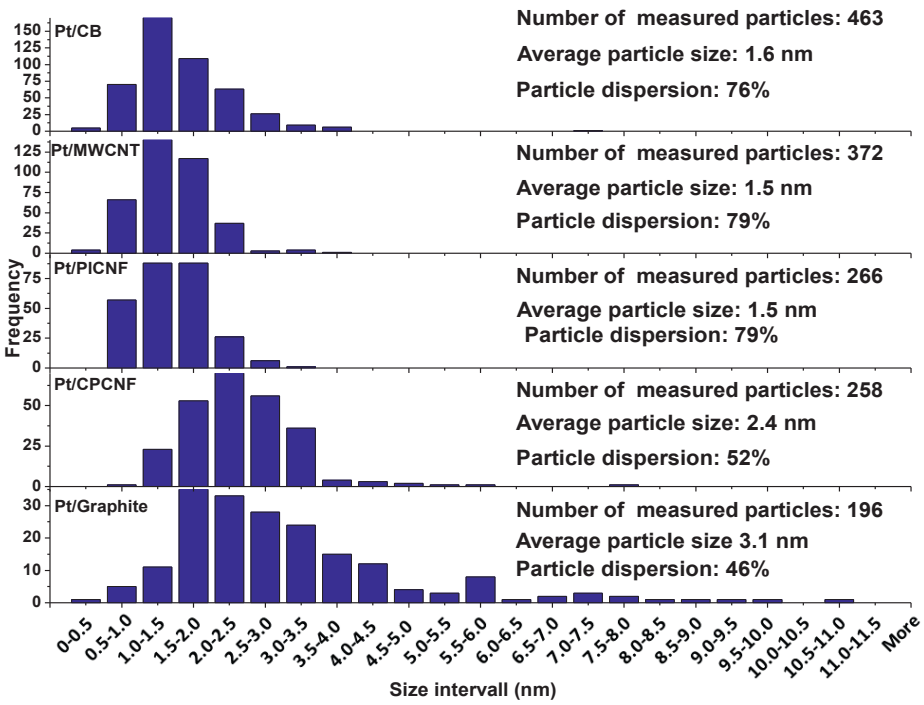

Figure 3.19 Platinum particle size distributions. Pt/MWCNT and Pt/PlCNF had the highest platinum dispersion (79%), while Pt/graphite had the lowest (46%). The catalysts Pt/CPCNF and Pt/graphite show the most significant tail in the particle distribution histogram, due to particle agglomeration.

The measurement of particle sizes by TEM is a very useful method to determine metal particle dispersion on supports, but this method has some limitations. It can be difficult to obtain representative images of a sample by studying only a small area, especially in samples with a very wide particle size distribution

caused by severe agglomeration [122] as Pt/graphite in this work. In addition, small particles can be invisible if the TEM resolution is too low, and this can lead to overestimation of the average particle size. There are also some difficulties in accurate measurement of the size of particles that are in close proximity to each other. Therefore, the TEM results have to be confirmed by other methods. A useful method for determining metal dispersion on (conductive) carbon supports is the cyclic voltammetry. It is performed by cycling the potential of a working electrode with a sample back and forth between two values, causing redox reactions and measuring the resulting current. This technique can be used to study adsorption and desorption of compounds such as H_2 or CO on a metal surface and measure the metal surface area (and metal dispersion) available for the reaction. The CO stripping voltammetry method usually operates with the following assumptions [123]:

I. Probed species (CO) form a saturated adlayer on the metal surface in a certain potential region.
II. The stoichiometric ratio between the metal atom and the adsorbed CO is constant.

The coverage of the saturated adlayer in the first assumption is dependent on the potential during the CO adsorption. As shown by Cuesta et al. [121] to achieve high coverage of CO in CO-free solution (0.68 for Pt(111) and 0.78 for Pt(100)), this potential has to be below 0.25 V against RHE. In this work, the adsorption potential was 0.05 V.

There is no consensus on what the stoichiometric ratio between CO and platinum is. Different values between 0.65 and 0.8 ML (metal to ligand) have been reported [123]. As shown by Cuesta et al. [121] at adsorption potential 0.1 V against RHE, the adsorbed CO on polycrystalline surfaces is a mixture of on top (1 ML) and twofold (0.5 ML) adsorption. This issue is complicated further

by the fact that CO adsorbed on platinum and CO in the solution (electrolyte) are in a dynamic equilibrium. Therefore, when CO is removed by an inert gas, the CO coverage of the electrode will decrease [121]. In CO stripping from the platinum surface it is common to use the charge density for oxidation of the monolayer value of 0.420 mC/cm^2 [74; 122; 123] and this value is assumed to be independent of the particle dispersion.

The voltammograms are presented in Figure 3.20. The thin line is obtained after the CO stripping, while the thick line is obtained during the stripping. All voltammograms can be divided into three regions, region A, B, and C. The stripping of adsorbed hydrogen is seen in the region A. The current in this region was higher for the sample without adsorbed CO, indicating that after the CO adsorption the Pt surface was occupied by CO rather than hydrogen. It is known that CO adsorbs strongly on the platinum surface and can displace most other preadsorbed species including hydrogen atoms [165]. When the surface was stripped of CO, hydrogen atoms (protons) from the acidic solution will again occupy the platinum surface. The adsorbed CO is stripped in region B, and the area difference between the voltammograms with and without adsorbed CO is dependent on the platinum surface area available for CO adsorption. All observed CO stripping peaks have their maximum between 0.85 and 0.90 V. Region C occurs at decreasing potential and the observed current in this region could be caused by a reduction of platinum oxides that have been formed at increasing oxidation potentials [123].

The simplest approach is to consider that Pt oxide formation is independent of the presence of CO and is equal during and after CO stripping [122]. However, it is seen in Figure 3.20, that the oxide formation for all tested samples was not the same during and after the CO stripping. The effect of CO on platinum oxidation is not clear, nevertheless, Chen et al. [123] has reported that repeated

CO adsorption and CO stripping will cause a significant alteration in the surface structure of catalysts with high dispersion. Chiang et al. [34] has reported that the oxide formation and reduction occurs in the region from 0.5 V to 1.0 V and this region coincides with the stripping peak.

The amount of the oxide formation during the CO stripping, as seen in Figure 3.20, was more significant than in several other studies where potentiometric stripping of CO used to characterize platinum catalysts [74; 122]. This could be caused by a small size of Pt particles used in this work because small metal particles are more oxophilic [166], i.e. more prone to oxidation. It is also possible that the observed difference was caused by higher concentration of oxygen in the electrolyte after purging with N_2. Although the electrolyte was purged with N_2 for approximately 30 minutes, this difference could have been caused by differences in the experimental setup.

To obtain more accurate results, assuming that the charges for the Pt oxide formation and reduction are the same, area C (difference between curve during and after the CO stripping) was subtracted from area B. Both the results with and without correction for the oxide formation are presented in this thesis (Tables 3.6 and 3.7).

Observed CO stripping peaks were in 0.85-0.86 V range for all catalysts in this study except for Pt/MWCNT, which had a stripping peak at 0.90 V. According to Maillard et al. [167] the overpotential for CO oxidation on the platinum surface can indicate a high dispersion of platinum. However, as seen from Table 3.6, Pt/PlCNF has at least as high dispersion, and no such overpotential was observed for this sample. Other authors have reported that the position of the CO stripping peak can be influenced by the type of Pt crystal surface [168].

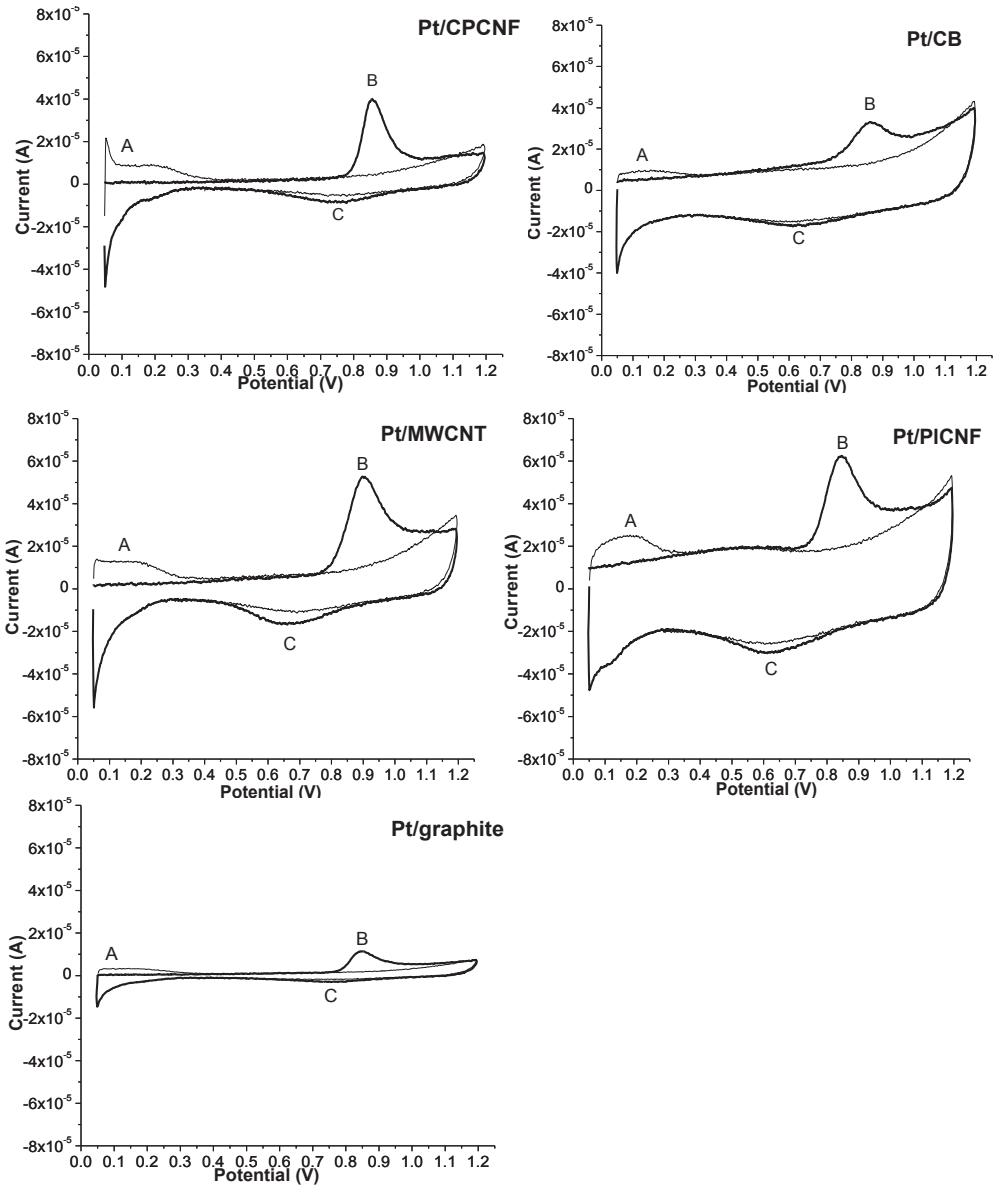

Figure 3.20 Voltammograms for the catalysts studied in this thesis. First stripping after CO adsorption (thick line) was done, then the second stripping (thin line) was done to obtain a voltammogram of CO-free catalyst. Results of the particle size and dispersion measurements from TEM and CV can be seen in Table 3.6.

Mayrhofer et al. [166] have reported that the onset potential of CO oxidation is almost independent of the Pt particle size. However, the particle size affects the rate of the CO oxidation (and CO_2 production) with larger particles oxidizing CO at a higher rate than smaller particles, due to fewer defects on the surface of the latter. In this work all CO stripping measurements were done at the same scan rate, so the rate of CO oxidation would influence the shape of the CO stripping peak. However, as the majority of the particles in the studied catalysts were smaller than 5 nm the effect of different particle sizes on the rate of CO oxidation cannot be unambiguously determined.

Some authors [74; 121; 169; 170] have reported a prepeak in the region before the CO desorption peak and the origin of this prepeak has been discussed in the literature. Millard et al. [170] have suggested that two separate stripping peaks originate from different electronic properties of particles of different sizes. They have reported that a bimodal particle size distribution can result an independent population of CO adsorbed on platinum particles observed as a smaller peak after the main peak. Muthuswamy et al. [74] has reported that a prepeak about 0.09-0.15 V before the CO stripping peak appear in a study of catalysts with higher Pt loadings (10.6 wt% and 16.7 wt%) on oxidized supports (CNFs), but not at lower loading (4.5 %wt). This could indicate that the prepeak was caused by an interaction between platinum and the oxidized sites on the support. At lower loadings, the negatively charged platinum colloids are deposited on the oxygen-free sites, while at higher loadings some of the colloids are deposited on sites with acidic oxygen-containing groups. An unfavorable charge interaction between negatively charged colloids and acidic groups causes significant agglomeration, and those agglomerates could have desorbed CO at the lower potential. It is not clear if the prepeak is caused by merely agglomeration or metal-support interaction between oxygen-containing groups and platinum.

Nevertheless, in this work the supports were not oxidized and the loadings were low (<1 wt%) giving monomodal rather than a bimodal distribution of particle sizes, so no prepeaks were observed.

An alternative explanation of the origin of the prepeak has been reported by Morimoto et al. [169] and Cuesta et al. [121] on polycrystalline platinum electrodes. According to Morimoto et al. [169] the prepeak is caused by oxidation of the bridge-bonded CO molecules, while the linear bonded CO molecules are oxidized in the main CO stripping peak. On the other hand, Cuesta et al. [121] suggests that the splitting of the stripping peak is caused by a difference between CO adsorbed at step sites and terrace sites. Since both linear and bridge bonded CO adsorption is expected in this work as well as CO is expected to adsorb at both step sites and terrace sites, the absence of the splitting of CO stripping peak is not expected. This could be related to a different nature of the studied catalysts. Both by Cuesta et al. and Morimoto et al. have studied bulk electrodes. Therefore, those catalysts might have different metal surface properties than carbon-supported catalysts with highly dispersed metal particles.

The TEM results generally gave a somewhat higher estimation of dispersion and a lower estimation of average particle size than CV results that were corrected for oxide formation, as seen from Table 3.6.

The TEM and the CV results show a good correlation for Pt/PlCNF and the discrepancy for this sample is not significant. The discrepancy in the measured particle size (corrected for the oxide formation) for Pt/CPCNF and Pt/MWCNF is 0.5 nm (21%) and 0.4 nm (27%) respectively. Unfortunately, not enough parallel measurements with CV of Pt/CPCNF and Pt/MWCNF were done to calculate the standard deviation.

Table 3.6 Results showing particle size and dispersion obtained by TEM and CV. The discrepancy between TEM and CV results is most pronounced for Pt/CB and Pt/graphite. The standard deviation is given in parenthesis.

Samples	Results from TEM		Results from Cyclic voltammetry		Results from Cyclic voltammetry (corrected for oxide formation)	
	Particle size	Dispersion	Particle size	Dispersion	Particle size	Dispersion
	nm	%	nm	%	nm	%
Pt/CB	1.6 (0.3)	76 (11)	2.1 (0.3)	54 (6)	2.5 (0.2)	45 (4)
Pt/MWCNT	1.5 (0.1)	79 (2.3)	1.4	79	1.9	60
Pt/PlCNF	1.5 (0.2)	79 (4.7)	1.3	87	1.5	75
Pt/CPCNF	2.4 (0.2)	52 (3.7)	2.3	50	2.9	39
Pt/graphite	3.1 (0.8)	46 (8.4)	6.3 (0.7)	18 (2)	7.9 (1)	14 (2)

Since both TEM and CV methods are based on entirely different principles, some discrepancy was expected. Both methods are based on assumptions that could cause a deviation from the correct value. For example, in case of TEM some bias could have been caused by limited TEM resolution when the size of overlapping particles is measured. It can be difficult to determine if one elongated particle or two (or more) overlapping particles are observed. In case of CO stripping, some error could have been caused by premature CO desorption during the N_2 purging and before the stripping step. Since CO adsorbed on the Pt surface is in dynamic equilibrium with CO in the solution [121], the surface coverage with adsorbed molecules will go down during the N_2 purging. This will in turn affect the CO monolayer stripping charge that is used in equation 5 (page 36). Nevertheless, those discrepancies are not very large and this indicates that the TEM and the CV methods can give consistent values for

platinum dispersion for platinum catalysts supported by carbon nanofibers and carbon nanotubes.

The discrepancy for Pt/CB and Pt/graphite was more severe with deviation in particle size of 0.9 nm (56%) and 4.7 nm (155%) respectively. However, both methods gave the same order of metal particle size, as seen from Table 3.6:

Pt/PlCNF ≤ Pt/MWCNT < Pt/CB < Pt/CPCNF < Pt/graphite

The larger discrepancy between the CV results and the TEM results for Pt/CB could have been caused by the high microporosity of the carbon black support. The micropores of CB can be inaccessible to Nafion® micelles (>40 nm in size), reducing the electrochemical activity of platinum particles in those pores [83] leading to an underestimation of the dispersion. This problem can be especially noticeable when low loadings (as in this work) are applied since a large fraction of deposited metal particles can be inaccessible due to mass transfer limitations.

The discrepancy between the CV and TEM results for Pt/graphite could have been caused by difficulties in determining the average particle size in this sample with TEM. Pronounced particle sintering led to a wide particle size distribution (Figures 3.14 page 65 and 3.19, page 76). Therefore, some of the largest Pt agglomerates may not be present in the selected TEM images. In contrast to TEM, CV gives an estimate of the average particle size in the entire sample. A similar discrepancy has been reported by Vidaković et al. [122] when comparing TEM and CV methods for determining the average particle size of an unsupported platinum catalyst.

A convenient way to compare electrochemical catalysts is to compare their active surface areas per gram of the catalyst metal. The active metal areas of the tested catalysts are presented in Table 3.7.

Table 3.7 Active platinum surface areas per gram of platinum metal. The order of active surface area is the same as the order of particle size and dispersion described in the text, with Pt/PlCNF having the largest metal surface area and Pt/graphite having the lowest.

Samples	CV results not corrected for oxide formation m^2/g_{Pt}	CV results corrected for oxide formation m^2/g_{Pt}
Pt/CB	132 (61 %)	112 (61 %)
Pt/MWCT	196 (90 %)	149 (81 %)
Pt/PlCNF	217 (100 %)	185 (100 %)
Pt/CPCNF	124 (57 %)	96 (52 %)
Pt/graphite	45 (21 %)	36 (19 %)

Since the tested catalysts had similar metal loading, the order of active surface area is the same as the order of particle size and dispersion described above.

3.3 Catalytic experiments

3.3.1 Ethene hydrogenation experiments

Ethene hydrogenation over platinum is a structure insensitive reaction [171; 172; 173], i.e. independent of the type of Pt crystal faces exposed. Therefore, this reaction is dependent only on the surface area of the active metal. For this reason, ethene hydrogenation tests can be done to compare the active surface area of different platinum catalysts.

Ethene hydrogenation is exothermic [109], and therefore the temperature was allowed to stabilize at 100 °C during the first 60 min time on stream (TOS). This approach assumes that the catalyst deactivation (by polymerization of ethene) affects the activity of all samples equally. Experiments without catalysts have

shown that at those conditions a contribution from gas phase reactions was negligible. Similarly, no catalytic activity was observed over the platinum-free supports, showing that the catalytic contribution of carbon supports at the tested conditions was negligible. This includes PlCNF support that contained 0.31 wt% Ni and indicates that amount of accessible Ni was not enough to have an effect on this reaction. The order of catalyst activity reported as conversion of ethene after 60 min was:

Pt/PlCNF(68%) ≈Pt/MWCNT(68%) >Pt/CB(43%) >Pt/CPCNF(35%) >Pt/graphite(16%)

This order is similar to the order of dispersion obtained from TEM and CV (page 83). If the conversions are divided by the platinum loading (page 50) and this order is normalized setting the highest conversion (over Pt/PlCNF) to 100% then the results can be compared to results of the active surface area per gram of platinum in Table 3.7.

Pt/PlCNF(100%)≈Pt/MWCNT(96%)>Pt/CB(62%)>Pt/CPCNF(54%)>Pt/graphite(24%)

While TEM indicates that Pt/CB has similar or slightly lower dispersion (and active area) than Pt/PlCNF and Pt/MWCNT, both CV and ethene hydrogenation methods indicate that Pt was significantly better dispersed on MWCNT and PlCNF than on CB. This is in spite of larger BET surface area of CB (page 54). This discrepancy can be caused by the larger microporosity of CB causing diffusion limitations. Those diffusion limitations could affect both CV and ethene hydrogenation results but not the TEM results. The activity for ethene hydrogenation of Pt/CB per gram of platinum is about 62% of the activity of Pt/PlCNF and this is in line with CV results presented in Table 3.7 showing that Pt/CB has 61% of the active surface area of Pt/PlCNF. Low BET surface area samples Pt/CPCNF and Pt/graphite show 54% and 24% activity compared to Pt/PlCNF. This is also close to values in Table 3.7 of 52-57% and 19-21%

respectively. The largest discrepancy was observed for Pt/MWCNT. The conversion over Pt/MWCNT was somewhat higher than expected from Table 3.7 and was 96% of the conversion over Pt/PlCNF, while the measured active surface area from Table 3.7 was 81-90% of the active surface area of Pt/PlCNF.

The most important source of possible error in this experiment was the difficulty of controlling the temperature during the first 60 minutes of the reaction. Nevertheless, the results confirm that the ethene hydrogenation tests can be used to determine the relative active (metal) surface of different platinum-containing catalysts. Although this method cannot measure dispersion and particle size directly, if the metal loading is known and if the active surface area of one of the samples in a series can be determined by another method, an estimate of the dispersion and particle size can be calculated.

3.3.2 Propane dehydrogenation experiments

Propane dehydrogenation without hydrogen in the feed

Experiments with an empty reactor have shown that the contribution from the gas phase reactions was negligible at the tested reaction conditions (with and without H_2 in the feed). Also experiments with platinum-free carbon supports have shown a negligible conversion. Conversions obtained over Pt/CB and Pt/MWCNT without the addition of H_2 to the feed and without prior reduction of the catalyst with H_2 are presented in Figure 3.21. The reaction over Pt/CB exhibited approximately 8% conversion of propane at 10 min time on stream (TOS). This conversion decreased to less than 0.3% after 30 min TOS indicating rapid deactivation of the catalyst. The Pt/MWCNT catalyst had very low activity, with conversion below 0.5%.

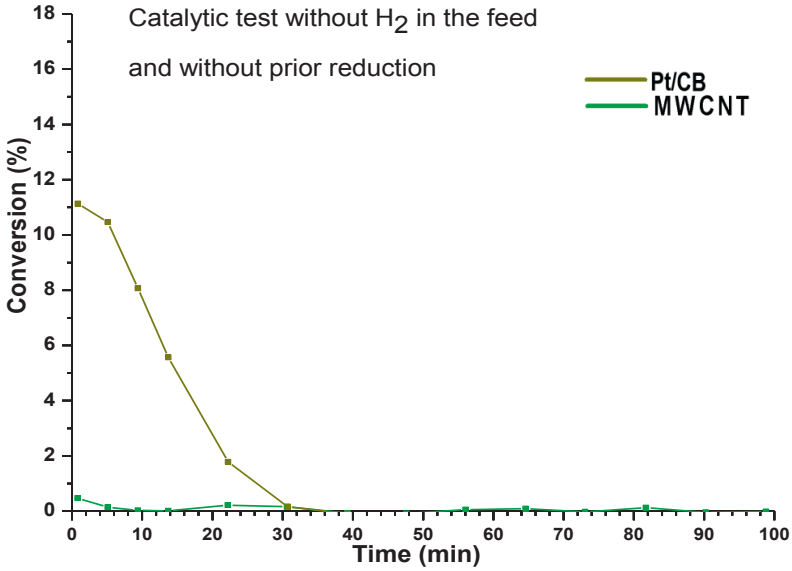

Figure 3.21 Conversion results for propane dehydrogenation without prior reduction of the catalysts and without the addition of hydrogen to the feed.

The main product was propene, as seen in Table 3.8. No other products were detected over Pt/MWCNT, but this could have been caused by low conversion leading to product concentrations lower than the detection limits. The detected by-products in the reaction over Pt/CB were ethane, ethane, and methane. This indicates that the rapid deactivation was probably caused by the coke that was produced together with C2 compounds and methane via a cracking mechanism.

Table 3.8 Selectivities to different products during propane dehydrogenation without H_2 in the feed and without prior reduction. Low conversion over Pt/MWCNT led to product concentrations lower than the detection limits.

Samples	C_3H_6 (%)		C_2H_6 (%)		C_2H_4 (%)		CH_4 (%)	
	10 min	60 min	10 min	60 min	10 min	60 min	10 min	60 min
Pt/CB	98.0	100	0.55	n.d.	0.8	n.d.	0.60	n.d.
Pt/MWCNT	100	100	n.d.	n.d.	n.d.	n.d.	n.d.	n.d.

As seen in Figure 3.22, the reduction of the catalysts with H_2 prior to the catalytic test has increased the conversion over Pt/CB from 8% to 10% after 10 minutes TOS. This indicates that not all platinum in Pt/CB was in the reduced state, and in spite of a reduction step during the catalyst preparation (heating of platinum solution with ethylene glycol), some non-metallic Pt remained in the catalyst. Therefore, a gas-phase reduction step with H_2 was necessary for this catalyst. Despite the reduction, the catalysts Pt/graphite, Pt/PlCNF, Pt/CPCNF, and Pt/MWCNT exhibited low activity, and lack of a reduction step cannot explain the low activity of those catalysts.

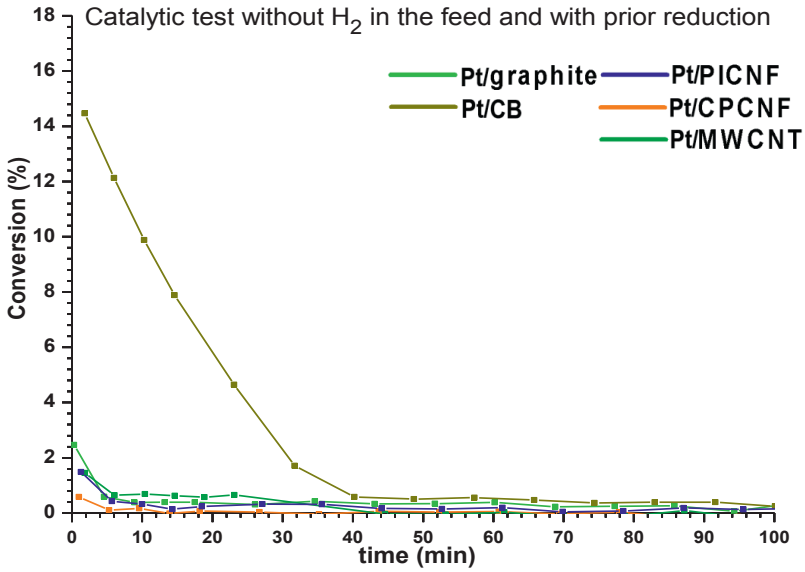

Figure 3.22 The reduction with hydrogen before the measurement slightly improved the conversion over Pt/CB. All other catalysts exhibited low activity.

Table 3.9 Selectivity to different products in propane dehydrogenation over reduced Pt/CB without H_2 in the feed. Propene was the main product. All by-product concentrations for the catalysts Pt/MWCNT, Pt/PlCNF, Pt/CPCNF, and Pt/graphite were below the detection limit due to low conversions and were therefore not observed.

Samples	C_3H_6 (%)		C_2H_6 (%)		C_2H_4 (%)		CH_4 (%)	
	10 min	60 min	10 min	60 min	10 min	60 min	10 min	60 min
Pt/CB	98.9	100	0.43	n.d.	0.66	n.d.	n.d.	n.d.

In spite of the improvement in the activity of Pt/CB catalyst after reduction, the catalyst still deactivated rapidly, and the conversion was reduced to 0.6% after 40 min TOS. All other catalysts have shown very low activity, indicating that those catalysts were either inactive or have rapidly deactivated. Since all catalysts in this thesis had available platinum, as seen from CV and ethene hydrogenation experiments and platinum is catalytically active for propane dehydrogenation, the rapid deactivation hypothesis seems more likely. In addition, the measured activity of all catalysts was slightly higher the first 5 minutes on stream, as seen in Figure 3.22, indicating a rapid deactivation at the beginning of the reaction. The conversion level the first 2-3 minutes is difficult to quantify, because it was measured before the gas that was initially present in the reactor (helium) was flushed away, and before the feed gas composition (including nitrogen that was used as an internal standard) has stabilized. Nevertheless, a measurable and decreasing amount of product in the first minutes of the reaction indicates a rapid deactivation, probably by coking. In spite of this, the carbon balance number calculated from equation 10 (page 40) was 101 ± 3%. Therefore, the amount of produced coke was low, indicating that the formed coke was highly toxic to the catalysts.

Propane dehydrogenation with hydrogen in the feed

The addition of 4.3% H_2 to the feed improved the conversion over all catalysts, as seen in Figure 3.23 and Figure 3.24. This confirms that the observed rapid deactivation was caused by coking. After 60 min TOS, the conversion over the reduced Pt/CB was 9.1%. Similar positive effect of H_2 was observed for other catalysts, although they were less active than Pt/CB.

The effect of hydrogen slowing down the coke formation rate is well known and has been observed with other Pt-based catalysts by Li et al. [174]. Calculation of the reaction equilibrium with the UniSim Design R400 software has shown that the introduction of 4.3% hydrogen to the feed reduced the equilibrium conversion, from 30.5% to 24.3%. This was expected because the presence of H_2 (one of the products) will reduce the equilibrium conversion according to the Le Chatelier's principle. However, this conversion was still above the conversion achieved by the tested catalysts, thus allowing informative comparison of catalysts to be done.

The positive effect of the reduction with H_2 prior to the reaction was clearer when hydrogen was added to the feed. This was especially noticeable for the reaction over catalysts Pt/CB and Pt/PlCNF. The conversion over unreduced Pt/CB increased the first 5 minutes on stream when hydrogen was added to the feed, as seen in Figure 3.23 (page 94). This can indicate that some of the platinum in the catalyst was reduced during the reaction. This was not observed in reaction over other catalysts. It is possible that the diffusion limitations in the micropores of CB were slowing down the reduction of platinum compared to other catalysts. This made the reduction observable as an increase in the conversion graph, while the reduction of Pt in other samples was completed before the first measurement. Also Pt/PlCNF showed different behavior with

and without reduction prior to the catalytic test. In experiments without the reduction, this catalyst exhibited lower conversion than Pt/MWCNT, as seen in Figure 3.23. After the reduction, this catalyst exhibited higher activity than Pt/MWCNT, as seen in Figure 3.24 and as expected from the measured active (platinum) surface area of this catalyst (page 85). This could indicate that Pt/PlCNF catalyst contained a larger amount of unreduced platinum than Pt/MWCNT. However, all catalysts in this thesis were prepared with same partially reduced Pt-colloidal dispersion and should contain same amounts of unreduced platinum. In addition, it seems unlikely that the platinum was not reduced during the catalytic tests with hydrogen in the feed, as observed for Pt/CB. It is possible that the reduction with hydrogen prior to the catalytic test has affected the metal dispersion of Pt/PlCNF. The TEM study have shown that Pt/PlCNF exhibited stronger metal-support interaction than Pt/MWCNT, seen as a flat shape of Pt particles on PlCNF support in Figure 3.10 (page 61).

The addition of H_2 improved the selectivity to propene, as seen in Table 3.10 and Table 3.11, probably by suppressing the undesired cracking reactions. Generally, the addition of H_2 reduced the C_2H_4/C_2H_6 ratio and this could indicate that hydrogen saturates ethene or its precursors. The selectivity to cracking products was reduced, but the amount of change was different for various catalysts. For Pt/CB, the addition of H_2 did not affect the selectivity to methane as much as ethane and ethene. For other catalysts, especially for Pt/MWCNT, the reduction of the selectivity to methane was much more significant. It is not clear why propane dehydrogenation over Pt/MWCNT had a much higher selectivity to methane than other catalysts. This cannot be explained by the higher acidity of oxygen-containing groups on MWCNT, since all supports had a similar value of the isoelectric point (page 52). The higher selectivity to methane could be related to the metal-support interaction promoting formation

of certain platinum crystalline faces. The platinum crystal surfaces with a high concentration of kink sites are known to be most active for the hydrogenolysis of alkanes [175]. It is possible that it is related to high overpotential to CO oxidation, as seen in section 3.2 (pages 79 and 80). However, the TEM images could not provide any evidence of a more faceted structure of platinum particles on MWCNT.

The selectivities for each catalyst changed differently with time. With an addition of H_2, the reaction over reduced Pt/CB produced 98% propene after 10 minutes TOS, and this selectivity was stable after 60 minutes TOS. On the other hand, reduced Pt/MWCNT, Pt/PlCNF, Pt/CPCNF, and Pt/graphite had propene selectivities of 91.4%, 91.1%, 92.7%, and 93.8% respectively after 10 minutes on stream. This selectivity increased by 1-3% after 60 minutes TOS, probably due to deactivation of sites responsible for cracking.

The highest conversion and the best selectivity to propene over Pt/CB both with and without H_2 comes in spite of the fact that the dispersion (or available Pt surface area) of this catalyst was not the highest, as shown by TEM, CV, and ethene hydrogenation experiments (pages 83 and 86). The cause of the difference between Pt/CB and other tested catalysts is not clear, but CB has significantly different structure than the more ordered MWCNT, PlCNF, CPCNF, and graphite. This could in turn affect the metal-support interaction and favor formation of propene over the coke producing reaction.

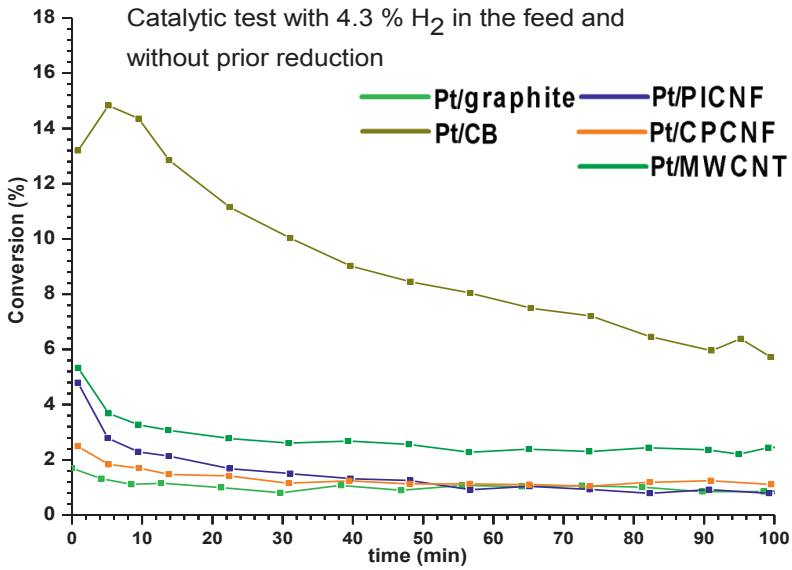

Figure 3.23 Conversion results for experiments done with the addition of H_2 to the feed and without prior reduction.

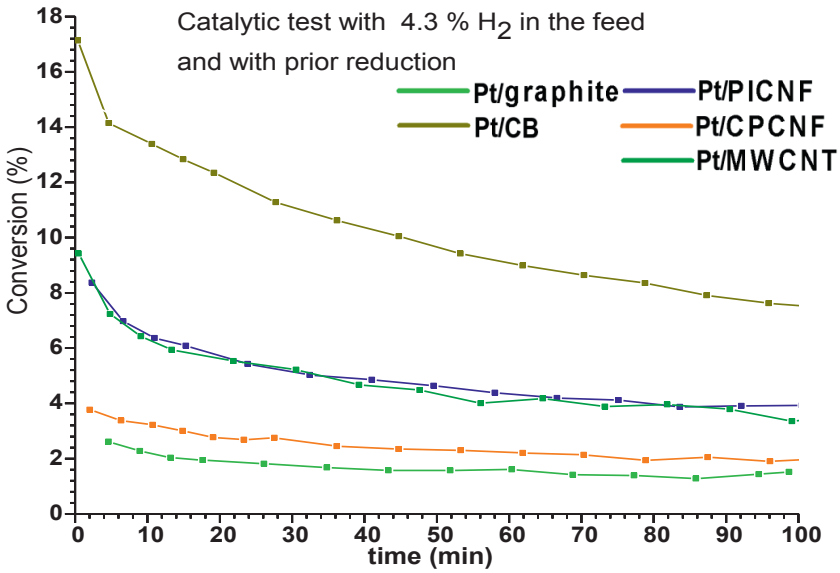

Figure 3.24 Conversion results for experiments done with the addition of H_2 in the feed and after prior reduction with H_2.

Table 3.10 Selectivities to different products during propane dehydrogenation with H_2 but without prior reduction. Propene was the main product, but the selectivity to cracking by-products was greater than over the reduced catalysts in Table 3.11.

Samples	C_3H_6 (%)		C_2H_6 (%)		C_2H_4 (%)		CH_4 (%)	
	10 min	60 min	10 min	60 min	10 min	60 min	10 min	60 min
Pt/CB	93.8	93.5	4.5	3.4	0.7	2.1	1.0	1.0
Pt/MWCNT	77.6	84.6	2.4	1.5	3.1	2.4	16.9	11.5
Pt/PlCNF	87.6	89.7	3.8	2.3	2.2	2.1	6.4	5.9
Pt/CPCNF	86.1	90.0	1.7	1.1	3.8	3.1	8.4	5.8
Pt/graphite	88.9	91.6	0.9	0.5	2.2	1.6	8.0	6.3

Table 3.11 Selectivities to different products during propane dehydrogenation with H_2 after reduction. Propene is the main product, while cracking products methane, ethane, and ethene have also been observed.

Samples	C_3H_6 (%)		C_2H_6 (%)		C_2H_4 (%)		CH_4 (%)	
	10 min	60 min	10 min	60 min	10 min	60 min	10 min	60 min
Pt/CB	97.7	97.9	1.3	0.9	0.1	0.3	0.9	0.9
Pt/MWCNT	91.4	93.7	2.5	1.4	1.4	1.2	4.7	3.7
Pt/PlCNF	91.1	93.3	3.6	2.0	1.5	1.4	3.8	3.3
Pt/CPCNF	92.7	95.7	1.6	0.7	2.7	1.5	3.0	2.1
Pt/graphite	93.8	95.3	1.2	0.5	2.0	1.2	3.0	3.0

CB is a commercial carbon black and the only tested support that is not composed of stacked graphene layers. The platinum support interaction is dependent on the structure of the support, and a semi-crystalline support, such as carbon black, will result in a weaker interaction than a crystalline support. It is not clear if the observed difference in catalytic properties of the tested catalysts is caused by merely electronic effects, or by a possible phase restructuring of the platinum particles induced by the stronger interaction with the supports. This difference between different carbon supports could be due to an effect of metal-support interaction causing particle reconstruction as observed by Muthuswamy et al. [74]. They reported that platinum nanoparticles deposited on platelet CNFs by the modified polyol method undergoes changes in their geometry as opposed to particles deposited on carbon black. A similar effect was observed in this study, as seen in Figures 3.06, 3.08, 3.10, and 3.12, carbon supports influences shape and possibly crystal structure of deposited platinum particles. However, the resolution of applied TEM was not sufficient to confirm the correlation between the crystal structure of faces of platinum particles and catalytic properties.

The turnover frequencies (TOF) for propane dehydrogenation with H_2 in the feed and with reduced catalyst were calculated using the TEM and the CV results and are presented in Table 3.12. Both types of catalyst with carbon nanofibers (Pt/PlCNF and Pt/CPCNF) and carbon nanotubes (Pt/MWCNT) show very similar TOF calculated when CV results are not corrected for Pt oxide formation. When the CV results are corrected for the oxide formation, the deviation is larger but still acceptable.

Table 3.12 The TOF for the propane dehydrogenation reaction after 10 min time on stream, calculated from catalyst dispersion obtained from TEM and from CV.

Samples	TOF values from TEM	TOF values from Cyclic Voltammetry	
		Not corrected for Pt oxide formation	Corrected for Pt oxide formation
	(s^{-1})	(s^{-1})	(s^{-1})
Pt/CB	0.77	1.08	1.30
Pt/MWCNT	0.35	0.35	0.46
Pt/PlCNF	0.38	0.35	0.40
Pt/CPCNF	0.31	0.32	0.41
Pt/graphite	0.23	0.59	0.77

This indicates that CV and TEM give consistent results when applied to characterize this type of catalysts. The TOF results for Pt/graphite and Pt/CB are not consistent, due to inconsistency in the value of measured dispersion by the TEM and the CV methods. This exposes the weaknesses of each method, as TEM gives a larger error when a sample has a wide particle size distribution (as on graphite), while the CV method is dependent on accessibility of Pt particles in micropores (of CB).

Nevertheless, both methods indicate that the propane dehydrogenation reaction over Pt/CB had a higher TOF than the reaction over the other catalysts, meaning that sites in Pt/CB are more active, or other activity is introduced.

The polyol method used in this work did not selectively produced sub-nanometer Pt particles. Still, some of the particles of size 0.5 nm or smaller have

been observed with TEM (page 76). Babar et al. [176] have used ab initio projector augmented wave pseudopotential method to study interaction of carbon and small Pt clusters and they have concluded that small Pt clusters (up to 10 atoms) may not be poisoned by carbon but rather form Pt-C covalent bonds that can improve the catalytic activity of those clusters. It can be suggested that in this work those covalent Pt-C bonds are formed on non-graphitic CB rather than CNTs or CNFs and this could be a possible explanation for the higher activity of Pt/CB.

4. Conclusions

A set of different carbon-supported Pt catalysts was prepared by depositing metal particles from a common suspension of Pt nanoparticles onto a range of different carbon supports. After depositing the Pt particles on the support, the catalysts were characterized using a range of techniques. The results show that TEM and CO stripping by CV give consistent values with a discrepancy in the average metal particle size of 27% or less for platinum catalysts supported by carbon nanofibers and carbon nanotubes. There were more severe discrepancies between the techniques for Pt/graphite and Pt/CB, probably due to issues with the mass transfer limitations, the particle size distributions, and TEM resolution. The hydrogenation of ethene, a facile reaction, was also used as a characterization tool, and the results confirmed the dispersion. In catalytic dehydrogenation of propane, the Pt/CB showed a higher conversion and TOF value than catalysts prepared using carbon nanofibers, carbon nanotubes, and graphite as support. In addition to giving higher TOF, the propane dehydrogenation reaction over Pt/CB was less susceptible to deactivation in experiments without hydrogen in the feed, indicating that the carbon black support either reduces the rate of coke formation or the toxicity of the coke formed. A possible reason can be a metal-support interaction, causing changes in the electronic properties of platinum or a possible restructuring of the metal surface due to interaction with the supports.

5. Suggestions for future work

Metal-carbon interaction is a complicated topic with many unsolved challenges remaining. In order to obtain more detailed knowledge how different carbon surfaces affect metal nanoparticles deposited on them a range of techniques not used in this thesis have to be utilized.

A better understanding of the metal-carbon interaction can be obtained by a systematic study of different metal-carbon catalysts with X-ray photoelectron spectroscopy, as it would give information about the binding energies and, therefore, the electronic state of platinum on different carbon supports.

The metal-support interaction can also be investigated by temperature programmed reduction measuring the reduction temperature of the active metal in hydrogen. However, this would require other catalyst preparation techniques because the polyol method used is this thesis results in (partially) reduced active metal.

Use of spectroscopic methods, such as IR, to study adsorbed probe molecules is another interesting tool that can give information about the degree of the metal-support interaction.

No on purpose functionalization of carbons has been studied in this thesis. However, different functional groups can interact with deposited metal particles and affect their catalytic properties. The effects of introduced functional groups can be worth investigating.

HRTEM analysis might not only give information about the dispersion of adsorbed metal particles on carbon supports but also about the crystallographic structure of metal particles. The crystallographic state of metal particles was not

studied in this work, but it can potentially be used as an indicator of the strength of the metal-support interaction.

It is important to keep in mind that the majority of carbons, including nanostructured carbons as carbon-nanotubes and carbon-nanofibers, have many different sites where metal particles can adsorb. Only a few methods (as HRTEM) can be used to investigate the effect of metal particles on each of those sites, and the rest of the methods will give an average state of those particles. In addition, metal particles of different size and structure can have a different interaction with the same site on carbon. Therefore, a detailed model of metal-support interaction on different carbons can be obtained only by a combination of experimental studies and molecular dynamic and other simulations. Those investigations might in the future give us the possibility to tailor catalysts at the atomic level for specific applications.

6. References

1. **Khavryuchenko OV, Khavryuchenko VD.** "Classification of carbon materials for developing structure-properties relationships based on the aggregate state of the precursors", 2014. *Chinese Journal of Catalysis.* Vol. 35, (Issue. 6), pp.778-782.

2. **Chalifoux WA, Tykwinski RR.** "Synthesis of Polyynes to Model the sp-Carbon Allotrope Carbyne", 2010. *Nature Chemistry.* Vol. 2, pp.967–971.

3. **Schlögl, R.** "Chapter Two – Carbon in Catalysis", 2013. *Advances in Catalysis.* Vol. 56, pp.103-185.

4. **Kim Y-A, Hayashi T, Naokawa S, Yanagisawa Y, Endo M.** "Comparative study of herringbone and stacked-cup carbon nanofibers", 2005. *Carbon.* Vol. 43, (Issue 14), pp.3005–3008.

5. **Ramos A, Cameán I, García AB.** "Graphitization thermal treatment of carbon nanofibers", 2013. *Carbon.* Vol. 59, pp.2–32.

6. **Radushkevich LV, Lukyanovich VM.** "O strukture ugleroda, obrazujucegosja pri termicheskom razlozhenii okisi ugleroda na zheleznom kontakte (About the structure of carbon formed by thermal decomposition of carbon monoxide on iron substrate)", 1952. *Zurn Fisic Chim.* 26, (Issue 1), pp.88-95, Original article (in russian) is available at: nanotube.msu.edu/HSS/2006/4/index.html, Updated: 5 July 2007, Accessed 23 Oct. 2014.

7. **Monthioux M, Kuznetsov VL.** "Who should be given the credit for the discovery of carbon nanotubes?", 2006. *Carbon.* Vol. 44, (Issue 9), pp.1621-1623.

8. **Iijima, S.** "Helical microtubules of graphitic carbon", 1991. *Nature.* Vol. 354, pp. 56-58.

9. **Iijima S, Ichihashi T.** "Single-shell carbon nanotubes of 1-nm diameter", 1993. *Nature.* Vol. 363, pp.603-605.

10. **Bethune DS, Kiang CH, De Vries MS, Gorman G, Savoy R, Vazquez J, Beyers R.** "Cobalt catalyzed growth of carbon nanotubes with single-atomic-layer walls", 1993. *Nature.* Vol. 363, pp.605-607.

11. **Ignacio M-G, Vera J, Conesa JA, Gonzalez JL, Merino C.** "Differences between carbon nanofibers produced using Fe and Ni catalysts in a floating catalyst reactor", 2006. *Carbon.* Vol. 44, (Issue 8), pp.1572-1580.

12. **Melechko AV, Merkulov VI, McKnight TE, Guillorn MA, Klein KL, Lowndes DH, Simpson ML.** "Vertically aligned carbon nanofibers and related structures: Controlled synthesis and directed assembly", 2005. *Journal of Applied Physics.* Vol. 97, (Issue 4), pp.1-40.

13. **Hughes TV, Chambers CR.** *"Manufacture of Carbon Filaments". US Patent 405480* 1889.

14. **Bartholomew, CH.** "Carbon Deposition in Steam Reforming and Methanation", 1982. *Catalysis Reviews: Science and Engineering.* Vol. 24, (Issue 1), pp.67-112.

15. **Hillert M, Lange N.** ”The structure of graphite filaments”, 1959. *Zeitschrift für Kristallographie.* Vol. 111, (Issue 1-6), pp.24-34.

16. **Teng L-h, Tang T-d.** "IR study on surface chemical properties of catalytic grown carbon nanotubes and nanofibers", 2008. *Journal of Zhejiang University SCIENCE A.* Vol. 9, (Issue 5), pp.720-726.

17. **Jong KPD, Geus JW.** ”Carbon Nanofibers: Catalytic Synthesis and Applications”, 2000. *Catalysis Reviews: Science and Engineering.* Vol. 42, (Issue 4), pp.481-510.

18. **Nørskov JK, Abild-Pedersen F, Rostrup-Nielsen JR, Sehested J, Helveg S.** “Mechanisms for catalytic carbon nanofiber growth studied by ab initio density functional theory calculations”, 2006. *Physical Review B.* Vol. 73, (Issue 11), p.115419.

19. **Baker RTK, Barber MA, Harris PS, Feates FS, Waite RJ.** "Nucleation and growth of carbon deposits from the nickel catalyzed decomposition of acetylene", 1972. *Journal of Catalysis.* Vol. 26, (Issue 1), pp.51–62.

20. **Figueiredo JL, Trimm DL.** "Gasification of Carbon Deposits on Nickel Catalysts", 1975. *Journal of Catalysis.* Vol. 40, (Issue 2), pp.154-159.

21. **V, Patel.** “Global carbon nanotubes market - industry beckons”. *Nanowerk.* Downloaded from: www.nanowerk.com/spotlight/spotid=23118.php, Posted: Oct 20 2011, Accessed: Oct. 24 2014.

22. **Wolf EE, Alfani F.** "Catalysts Deactivation by Coking", 1982. *Catalysis Reviews: Science and Engineering.* Vol. 24, (Issue 3), pp.329-371.

23. **Ampelli C, Perathoner S, Centi G.** “Carbon based catalysts: Opening new scenario to develop next generation nano-engineered catalytic materials”, 2014. *Chinese Journal of Catalysis.* Vol. 35, (Issue 6), pp.783-791.

24. **Zhu J, Zhao T, Kvande I, Chen D, Zhou X, Yuan W.** "Carbon Nanofiber-Supported Pd Catalysts for Heck Reaction: Effects of Support Interaction", 2008. *Chinese Journal of Catalysis.* Vol. 29, (Issue 11), pp.1145–1151.

25. **Toebes ML, van der Lee MK, Tang LM, Huis in ‘t Veld MH, Bitter JH, van Dillen AJ, de Jong KP.** "Preparation of Carbon Nanofiber Supported Platinum and Ruthenium Catalysts: Comparison of Ion Adsorption and Homogeneous Deposition Precipitation", 2004. *The Journal of Physical Chemistry B.* Vol. 108, (Issue 31), pp.11611-11619.

26. **Pereira MFR, Figueiredo JL, Orfao JJM, Serp P, Kalck P, Kihn Y.** "Catalytic activity of carbon nanotubes in the oxidative dehydrogenation of ethylbenzene", 2004. *Carbon.* Vol. 42, (Issue 14), pp.2807–2813.

27. **Ros TG, van Dillen AJ, Geus JW, Koningsberger DC.** "Surface Oxidation of Carbon Nanofibres", 2002. *Chemistry - A European Journal.* Vol. 8, (Issue 5), pp.1151–1162.

28. **Maiyalagan T, Viswanathan B, Varadaraju UV.** "Nitrogen containing carbon nanotubes as supports for Pt – Alternate anodes for fuel cell applications", 2005. *Electrochemistry Communications.* Vol. 7, (Issue 9), pp.905–912.

29. **Purdue University, Department of Chemistry, Honeywell.** Material Safety Data Sheet. Downloaded from: www.chem.purdue.edu/chemsafety/equip/hfmsds.pdf, Updated: Feb. 2002, Accessed: Nov. 13 2014.

30. **Wang Y, Shah N, Huggins FE, Huffman GP.** "Hydrogen Production by Catalytic Dehydrogenation of Tetralin and Decalin Over Stacked Cone Carbon Nanotube-Supported Pt Catalysts", 2006. *Energy Fuels.* Vol. 20, (Issue 6), pp.2612–2615.

31. **Chinthaginjala JK, Bitter JH, Lefferts L.** "Thin layer of carbon-nano-fibers (CNFs) as catalyst support for fast mass transfer in hydrogenation of nitrite", 2010. *Applied Catalysis A: General.* Vol. 383, (Issue 1-2), pp.24-32.

32. **Ovchinnikov II, Shuvaeva MA, Kuznetsov VL, Lisitsyn AS.** "Synthesis of Highly Dispersed Pt Catalysts on MWCNTs via Hydrolytic Deposition without Preliminary Modification of the Support", 2014. *Advanced Materials Research.* (Issue 1040), p.399.

33. **Ayala P, Arenal R, Rummeli M, Rubio A, Pichler T.** "The doping of carbon nanotubes with nitrogen and their potential applications", 2010. *Carbon.* Vol. 48, (Issue 3), pp.575–586.

34. **Chiang Y-C, Hsieh M-K, Hsu H-H.** "The effect of carbon supports on the performance of platinum/carbon nanotubes for proton exchange membrane fuel cells", 2014. *Thin Solid Films (TACT 2013 International Thin Films Conference).* Vol. 570, Part B, pp.221–229.

35. **Delgado JJ, Chen X, Tessonnier JP, Schuster ME, Del Rio E, Schlögl R, Su DS.** "Influence of the microstructure of carbon nanotubes on the oxidative dehydrogenation of ethylbenzene to styrene", 2010. *Catalysis Today.* Vol. 150, (Issues 1–2), pp.49–54.

36. **McGregor J, Huang Z, Parrott EPJ, Zeitler JA, Nguyen KL, Rawson JM, Carley A, TW Hansen, Tessonnier J-P, Su D S, Teschner D, Vass E M, Knop-Gericke A, Schlögl R, Gladden LF.** "Active coke: Carbonaceous materials as catalysts for alkane dehydrogenation", 2010. *Journal of Catalysis.* Vol. 269, (Issue 2), pp.329-339.

37. **Rinaldi A, Frank B, Su DS, Hamid SBA, Schlögl R.** "Facile Removal of Amorphous Carbon from Carbon Nanotubes by Sonication", 2011. *Chemistry of Materials.* Vol. 23, (Issue 4), pp.926–928.

38. **Ahmadi R, Amini MK.** "Synthesis and characterization of Pt nanoparticles on sulfur-modified carbon nanotubes for methanol oxidation", 2011. *International Journal of Hydrogen Energy.* Vol. 36, (Issue 12), pp.7275-7283.

39. **Sui Z-j, Zhou J-h, Dai Y-ch, Yuan W-k.** "Oxidative dehydrogenation of propane over catalysts based on carbon nanofibers", 2005. *Catalysis Today.* Vol. 106, (Issues 1–4), pp.90–94.

40. **Serp, P.** Chapter 9. Carbon Nanotubes and Nanofibers in Catalysis. [book auth.] Figueiredo J.L. Serp P. *Carbon Materials for Catalysis.* New Jersey : Wiley, 2009, p. P. 335.

41. **Li X, Tuo Y, Li P, Duan X, Jiang H, Zhou X.** "Effects of carbon support on microwave-assisted catalytic dehydrogenation of decalin", 2014. *Carbon.* Vol. 67, pp.775–783.

42. **Kvande I, Briskeby ST, Tsypkin M, Ronning M, Sunde S, Tunold R, Chen D.** "On the preparation methods for carbon nanofiber-supported Pt catalysts". *Topics in Catalysis.* Vol. 45, 2007, (Issue 1-4), pp.81-85.

43. **Verbrugge, MW.** "Selective Electrodeposition of Catalyst within Membrane-Electrode Structures", 1994. *Journal of The Electrochemical Society.* Vol. 141, (No. 1), pp.46-53.

44. **Luty-Błocho M, Wojnicki M, Pacławski K, Fitzner K.** "The synthesis of platinum nanoparticles and their deposition on the active carbon fibers in one microreactor cycle", 2013. *Chemical Engineering Journal.* Vol. 226, pp.46–51.

45. **Kuppan B, Selvam P.** "Platinum-supported mesoporous carbon (Pt/CMK-3) as anodic catalyst for direct methanol fuel cell applications: The effect of preparation and deposition methods", 2012. *Progress in Natural Science: Materials International.* Vol. 22, (Issue 6), pp.616–623.

46. **Rong-Li J, Cheng-Yang W, Bin Z.** "Preparation of platinum supported on carbon blacks with different surface chemical characteristics", 2005. *Proceedings of FUELCELL, Third International Conference on Fuel Cell Science, Engineering and Technology.* http://proceedings.asmedigitalcollection.asme.org/pdfaccess.ashx?ResourceID=5253199&PDFSource=13, Accessed: Nov. 12 2014.

47. **Bittencourt C, Hecq M, Felten A, Pireaux JJ, Ghijsen J, Felicissimo MP, Rudolf P, Drube W, Ke X, Van Tendeloo G.** "Platinum-carbon nanotubes interaction", 2008. *Chemical Physics Letters.* Vol. 462, (Issue 4–6), pp.260–264.

48. **Hsueh Y-C, Wang C-C, Kei C-C, Lin Y-H, Liu C, Perng T-P.** "Fabrication of catalyst by atomic layer deposition for high specific power density proton exchange membrane fuel cells", 2012. *Journal of Catalysis.* Vol. 294, pp.63–68.

49. **Chaa SY, Leeb WM.** "Performance of Proton Exchange Membrane Fuel Cell Electrodes Prepared by Direct Deposition of Ultrathin Platinum on the Membrane Surface", 1999. *Journal of The Electrochemical Society.* Vol. 146, (Issue 11), pp.4055-4060.

50. **Solar JM, Leon y Leon CA, Osseo-Asare K, Radovic LR.** "On the importance of the electrokinetic properties of carbons for their use as catalyst supports", 1990. *Carbon.* Vol. 28, (Issue 2-3), pp.369-375.

51. **Oh H-S, Oh J-G , Kim H.** "Modification of polyol process for synthesis of highly platinum loaded platinum–carbon catalysts for fuel cells", 2008. *Journal of Power Sources.* Vol. 183, (Issue 2), pp.600–603.

52. **Lau AC, Furlong DN, Healy TW, Grieser F.** "The electrokinetic properties of carbon black and graphitized carbon black aqueous colloids", 1986. *Colloids Surfaces.* Vol. 18, (Issue 1), pp.93-104.

53. **Coloma F, Sepulveda-Escribano A, Fierro JLG, Rodriguez-Reinoso F.** "Preparation of Platinum Supported on Pregraphitized Carbon Blacks", 1994. *Langmuir.* Vol 10, (No. 3), pp.750-755.

54. **Rodriguez-reinoso, F.** "The role of carbon materials in heterogeneous catalysis", 1998. *Carbon.* Vol. 36, (Issue 3), pp.159-175.

55. **Coloma F, Sepulveda-Escribano A, Rodriguez-reinoso F.** "Heat-Treated Carbon Blacks as Supports for Platinum Catalysts", 1995. *Journal of Catalysis.* Vol. 154, (Issue 2), pp.299-305.

56. **Katsuhiro N, Toru HO.** Chapter 2.10 – Platinum Group Metals Production. [book auth.] Treatise on Process Metallurgy: Industrial Processes. [ed.] Seetharaman S. *Volume 3: Industrial Processes.* s.l. : Elsevier, 2014, pp. 1071–1097.

57. **Reith F, Campbell SG , Ball AS, Pring A, Southam G.** "Platinum in Earth surface environments", 2014. *Earth-Science Reviews.* Vol. 131, pp.1-21.

58. **JM, Stellman.** *"Encyclopaedia of Occupational Health and Safety: Chemical, industries and occupations".* Vol. 3. s.l. : International Labour Organization, 1998. p. 141.

59. **Xiaoyan S, Rui W, Dangsheng S.** "Research progress in metal-free carbon-based catalysts", 2013. *Chinese Journal of Catalysis.* Vol. 34, (Issue 3), pp.508–523.

60. **Nørskov JK, Abild-Pedersen F, Studt F and Bligaard T.** "Density functional theory in surface chemistry and catalysis", 2012. *Proceedings of the National Academy of Science of the U.S.A.* Vol. 108, (No. 3), pp.937–943.

61. **Van Santen RA, Van Leeuwen PWNM, Moulijn JA, Averill BA.** *"Catalysis: An Integrated Approach", 1999.* 2nd ed. Amsterdam : Elsevier. pp. 433-434.

62. **Delmon B, Froment GF.** *Catalyst deactivation.* Amsterdam : Elsevier Science B.V., 1994. p. 17.

63. **Ratkovic S, Vujicic Dj, Kiss E, Boskovic G, Geszti O.** "Different degrees of weak metal–support interaction in Fe–(Ni)/Al2O3 catalyst governing activity and selectivity in carbon nanotubes' production using ethylene", 2011. *Materials Chemistry and Physics.* Vol. 129, (Issue 1–2), pp.398-405.

64. **Tauster SJ, Fung SC, Garten RL.** "Strong Metal-Support Interactions. Group 8 Noble Metals Supported on TiO2", 1978. *Journal of the American Chemical Society.* Vol. 100, (Issue 1), pp.170.

65. **Cagnoli MV, Alvarez AM, Gallegos NG, Bengoa JF, Duarte de Souza CD, Schmal M, Marchetti SG.** "Mössbauer and XPS spectroscopies studies of SMSI effect on Fe/Nb2O5 catalysts for the Fischer–Tropsch synthesis", 2007. *Applied Catalysis A: General.* Vol. 326, (Issue 1), pp.113-119.

66. **Cunningham J, O'Brien S, Sanz J, Rojo JM, Soria JA, Fierro JLG.** "Exceptional susceptibility of ceria-supported rhodium catalyst to inhibitory SMSI effects including acetone hydrogenation", 1990. *Journal of Molecular Catalysis.* Vol. 57, (Issue 3), pp.379–396.

67. **Rodriguez NM, Kim M-S, Baker RTK.** "Carbon Nanofibers: A Unique Catalyst Support Medium", 1994. *Journal of Physical Chemistry.* Vol. 98, (No. 50), pp.13108-13111.

68. **Planeix JM, Coustel N, Coq B, Brotons V, Kumbhar PS, Dutartre R, Geneste P, Bernier P,Ajayan PM.** “Application of Carbon Nanotubes as Supports in Heterogeneous Catalysis”, 1994. *Journal of the American Chemical Society.* Vol. 116, (No. 17), pp.7935–7936.

69. **Sanz-Navarro CF, Åstrand P-O, Chen D, Rønning M, van Duin ACT, Goddard WA.** "Molecular Dynamics Simulations of Metal Clusters Supported on Fishbone Carbon Nanofibers", 2010. *The Journal of Physical Chemistry C.* Vol. 114, (No. 8), pp.3522–3530.

70. **Sebetci A, Güvenç ZB.** "Energetics and structures of small clusters: PtN, N=2–21", 2003. *Surface Science.* Vol. 525, (Issue 1–3), pp.66-84.

71. **Kuhrt Ch, Harsdorff M.** "Photoemission and electron microscopy of small supported palladium clusters", 1991. *Surface Science.* Vol.245, (Issue 1-2), pp.173-179.

72. **Wang J, Yin G, Shao Y, Wang Z, Gao Y.** "Investigation of Further Improvement of Platinum Catalyst Durability with Highly Graphitized Carbon Nanotubes Support", 2008. *Journal of Physical Chemistry C.* Vol. 112, (Issue 15), pp.5784-5789.

73. **Sanz-Navarro CF, Åstrand P-O, Chen D, Rønning M, van Duin ACT, Jacob T, Goddard WA.** "Molecular Dynamics Simulations of the Interactions between Platinum Clusters and Carbon Platelets", 2008. *Journal of Physical Chemistry A.* Vol. 112, (No.7), pp.1392-140.

74. **Muthuswamy N, Gomez de la Fuente JL, Ochal P, Giri R, Raaen S, Sunde S, Rønning M and Chen D.** "Towards a highly-efficient fuel-cell catalyst: optimization of Pt particle size, supports and surface-oxygen group concentration", 2013. *Physical Chemistry Chemical Physics.* Vol. 15, pp.3803-3813.

75. **Kvande I, Zhu J, Zhao T-J,Hammer N, Rønning M,Raaen S, Walmsley JC, Chen D.** "Importance of Oxygen-Free Edge and Defect Sites for the Immobilization of Colloidal Pt Oxide Particles with Implications for the Preparation of CNF-Supported Catalysts", 2010. *Journal of Physical Chemistry C.* Vol. Vol. 114, (No. 4), pp.1752-1762.

76. **Chen W, Ji J, Duan X, Qian G, Li P, Zhou X, Chen D, Yuana W.** "Unique reactivity in Pt/CNT catalyzed hydrolytic dehydrogenation of ammonia borane", 2014. *Chemical Communications.* Vol. 50, (Issue 17), pp. 2142-2144.

77. **Lazaro MP, Garcıa-Bordeje E, Sebastian D, Lazaro MJ, Moliner R.** "In situ hydrogen generation from cycloalkanes using a Pt/CNF catalyst", 2008. *Catalysis Today.* Vol. 138, (Issue 3-4), pp.203–209.

78. **Du J-p, Song C, Song J-l, Zhao J-h, Zhu Z-p.** "Cyclohexane dehydrogenation over the platinum catalysts supported on carbon nanomaterials", 2009. *Journal of fuel chemistry and technology.* Vol. 37, (Issue 4), pp.468-472.

79. **Zhao T-J, Sun W-Z, Gu X-Y, Rønning M, Chen D, Dai Y-C, Yuan W-K, Holmen A.** "Rational design of the carbon nanofiber catalysts for oxidative dehydrogenation of ethylbenzene", 2007. *Applied Catalysis A: General.* Vol. 323, pp.135–146.

80. **Xiao-Feng Guo, Joong-Ho Kim, Geon-Joong Kim.** "Dehydrogenation of ethylbenzene to styrene on a direct synthesized Co, Ni/carbon nanotubes catalysts", 2011. *Catalysis Today.* Vol. 164, (Issue 1), pp.336–340.

81. **Liu X, Su DS, Schlögl R.** "Oxidative dehydrogenation of 1-butene to butadiene over carbon nanotube catalysts", 2008. *Carbon.* Vol. 46, (Issue 3), pp.547–549.

82. **Zhang J, Liu X, Blume R, Zhang A, Schlögl R, Su DS.** "Surface-Modified Carbon Nanotubes Catalyze Oxidative Dehydrogenation of n-Butane", 2008. *Science.* Vol. 322, (no. 5898), pp.73-77.

83. **Sharma S, Pollet BG.** "Support materials for PEMFC and DMFC electrocatalysts—A review", 2012. *Journal of Power Sources.* Vol. 208, pp.96–119.

84. **Park S, Shao Y, Kou R, Viswanathan VV, Towne SA, Rieke PC, Liu J, Lin Y, Wang Y,.** "Polarization Losses under Accelerated Stress Test Using Multiwalled Carbon Nanotube Supported Pt Catalyst in PEM Fuel Cells", 2011. *Journal of The Electrochemical Society.* Vol. 158, (Issue 3), pp.B297-B302.

85. **Shao Y, Yin G, Zhang J, Gao Y.** "Comparative investigation of the resistance to electrochemical oxidation of carbon black and carbon nanotubes in aqueous sulfuric acid solution", 2006. *Electrochimica Acta.* Vol 51, (Issue 26), pp.5853–5857.

86. **Li L, Xing Y.** "Electrochemical Durability of Carbon Nanotubes in Noncatalyzed and Catalyzed Oxidations", 2006. *Journal of The Electrochemical Society.* Vol. 153, (Issue 10), pp. A1823-A1828.

87. **Wong WY, Daud WRW, Mohamad AB, Kadhum AAH, Loh KS, Majlan EH.** "Recent progress in nitrogen-doped carbon and its composites as electrocatalysts for fuel cell applications", 2013. *International Journal of Hydrogen Energy.* Vol. 38, (Issue 22), pp.9370–9386.

88. **Geng D, Liu H, Chen Y, Li R, Sun X, Ye S, Knights S.** "Non-noble metal oxygen reduction electrocatalysts based on carbon nanotubes with controlled nitrogen contents", 2011. *Journal of Power Sources.* Vol. 196, (Issue 4), pp.1795–1801.

89. **Alexeyeva N, Shulga E, Kisand V, Kink I, Tammeveski K.** "Electroreduction of oxygen on nitrogen-doped carbon nanotube modified glassy carbon electrodes in acid and alkaline solutions", 2010. *Journal of Electroanalytical Chemistry.* Vol. 648, (Issue 2), pp.169–175.

90. **Zheng J-S, X-S Zhang, Li P, Zhu J, Zhou X-G, Yuan W-K.** "Effect of carbon nanofiber microstructure on oxygen reduction activity of supported palladium electrocatalyst", 2007. *Electrochemistry Communications.* Vol. 9, (Issue 5), pp.895–900.

91. **Li W, Waje M, Chen Z, Larsen P, Yan Y.** "Platinum nanopaticles supported on stacked-cup carbon nanofibers as electrocatalysts for proton exchange membrane fuel cell", 2010. *Carbon.* Vol. 48, (no. 4), pp.995-1003.

92. **Kang S, Lim S, Peck D-H, Kim S-K, Jung D-H, Hong S-H, Jung H-G, Shul Y.** "Stability and durability of PtRu catalysts supported on carbon nanofibers for direct methanol fuel cells", 2012. *International Journal of Hydrogen Energy.* Vol. 37, (Issue 5), pp.4685-469.

93. **Bessel CA, Laubernds K, Rodriguez NM, Baker RTK.** "Graphite Nanofibers as an Electrode for Fuel Cell Applications", 2001. *The Journal of Physical Chemistry B.* Vol. 105, (No. 6), pp.1115-1118.

94. **Dow Chemical Company.** "Product Safety Assessment, Ethylene". Downloaded from: msdssearch.dow.com/PublishedLiteratureDOWCOM/dh_0914/0901b80380914256.pdf?filepath=productsafety/pdfs/noreg/233-00280.pdf&fromPage=GetDoc, Updated: July 1 2014, Accessed: Oct. 25 2014.

95. **Ceresana – Market Intelligence. Consulting.** "Market Study: Propylene". 2011, Downloaded from: www.ceresana.com/en/market-studies/chemicals/propylene/, Accessed: Oct. 24 2014.

96. **Dow Chemical Company.** Product Safety Assessment, DOW™ Propylene. Downloaded from: http://msdssearch.dow.com/PublishedLiteratureDOWCOM/dh_07f3/0901b803807f335e.pdf?filepath=productsafety/pdfs/noreg/233-00236.pdf&fromPage=GetDoc, Posted: Nov. 19 2010, Accessed: Oct. 25 2014.

97. **Research and Markets.** "Research and Development Forecast of China Propylene Market, 2013-2015". Downloaded from: www.researchandmarkets.com/research/39x78m/research_and, Posted: Sept. 2013, Accessed: Oct. 24 2014.

98. **Intratec Solutions.** "Technology Economics: Propylene via Propane Dehydrogenation". Downloaded from: www.slideshare.net/intratec/propylene-production-via-propane-dehydrogenation, Posted: Jun 28 2012, Accessed: Oct. 24 2014.

99. **Tullo, A.** "Tough Times For Propylene Buyers". *C&EN.* Downloaded from: cenblog.org/the-chemical-notebook/2012/04/tough-times-for-propylene-buyers, Posted: March 10 2014, Accessed: Oct. 24 2014.

100. **Hodges, P.** "New propylene supply increases market uncertainty". *Chemical companies.* Downloaded from: www.icis.com/blogs/chemicals-and-the-economy/2012/08/on-purpose-propylene-set-to-ch/, Posted: Aug. 14 2012, Accessed: Oct. 24 2014.

101. **Bhasin MM, McCain JH, Vora BV, Imai T, Pujado PR.** "Dehydrogenation and oxydehydrogenation of paraffins to olefins", 2001. *Applied Catalyst A: General.* Vol. 221, (Issue 1-2), pp.397-419.

102. **Intratec knowledge base.** "Propylene from Propane via Dehydrogenation (similar to Lummus CATOFIN)". Downloaded from: base.intratec.us/home/chemical-processes/propylene/propylene-from-propane-via-dehydrogenation-2, Accessed: Oct. 24, 2014.

103. **Haensel, V.** *"Conversion of hydrocarbons with platinum composite catalyst". U.S. Patent 2,602,772* 8 July 1952.

104. **Sahebdelfar S, Tahriri Zangeneh.** "Dehydrogenation of Propane to Propylene Over Pt-Sn/Al2O3 Catalysts: The influence of operating conditions on product selectivity", 2010. *Iranian Journal of Chemical Engineering, .* Vol. 7, (No. 2), pp.51-57.

105. **Bloch, HS.** *"Catalytic dehydrogenation of paraffinic hydrocarbons at high space velocity". U.S. Patent 3,448,165* 3 June 1969.

106. **Vora, BV.** "Development of Dehydrogenation Catalysts and Processes", 2012. *Topics in Catalysis.* Vol. 55, (Issue 19-20), pp.1297-1308.

107. **Låte L, Rundereim J-I, Blekkan EA.** "Selective combustion of hydrogen in the presence of hydrocarbons. Pt-based catalysts". *Applied Catalysis A: General.* Vol. 262, 2004, (Issue 1), pp.53–61.

108. **Iglesias-Juez A, Beale AM, Maaijen K, Weng TC, Glatzel P, Weckhuysen BM.** "A combined in situ time-resolved UV–Vis, Raman and high-energy resolution X-ray absorption spectroscopy study on the deactivation behavior of Pt and Pt-Sn propane dehydrogenation catalysts under industrial reaction conditions", 2010. *Journal of Catalysis.* Vol. 276, (Issue 2), pp.268-279.

109. **Negi AS, Anand SC.** *"A Textbook of Physical Chemistry".* New Delhi : New Age International (P) Limited, 1985. p. 220.

110. **Horiuti J, Miyahara K.** "Hydrogenation of Ethylene on Metallic Catalysts". *National Standard Reference Data Series (NSRDS):8.* 1968, Downloaded from: www.nist.gov/data/nsrds/NSRDS-NBS-13.pdf, Accessed: Nov. 15 2014.

111. **Horiuti I, Polanyi M.** "Exchange reactions of hydrogen on metallic catalysts", 1934. *Transactions of the Faraday Society.* Vol. 30, pp.1164-1172.

112. **Cremer PS, Su X, Shen YR, Somorjai GA.** "Ethylene Hydrogenation on Pt(111) Monitored in Situ at High Pressures Using Sum Frequency Generation" . *Journal of the American Chemical Society.* Vol. 118, 1996, pp.2942-2949.

113. **Binder A, Seipenbusch M, Muhler M, Kasper G.** "Kinetics and particle size effects in ethene hydrogenation over supported palladium catalysts at atmospheric pressure". *Journal of Catalysis.* Vol.268, 2009, (Issue 1), pp.150–155.

114. **McLeod AS, Cheah KY, Gladden LF.** "The quantitative representation of heterogeneity in metal catalysts", 1998. *Studies in Surface Science and Catalysis.* Vol. 118, pp.1–14.

115. *The 8th Frumkin Symposium: ''Kinetics of Electrode Processes'', 2005* . **Tsypkin M, Briskeby ST, Kongstein OE, Børresen B, Tunold R.** Moscow : Russian Academy of Science, p.165.

116. **Aramendia MA, Borau V, Jimenez C, Marinas JM, Moreno A.** "Comparative measurements of the dispersion of Pd catalyst on SiO2-AlPO4 support using TEM and H2 chemisorption". *Colloids and Surfaces A: Physicochemical and Engineering Aspects.* Vol. 106, 1996, (Issue 2–3), pp.161-165.

117. **Will, FG.** "Hydrogen Adsorption on Platinum Single Crystal Electrodes", 1965. *Journal of the electrochemical society.* Vol. 112, (No. 4), pp.451-455.

118. **Umair A, Raza TZ, Raza H.** "On the Crystal Size Studies of Pyrolytic Carbon by Raman Spectroscopy". Downloaded from: http://arxiv.org/abs/1303.6364, Posted: Mar 26 2013, Accessed: Feb. 12 2015.

119. **Vallerot J-M, Bourrat X, Mouchon A, Chollon G.** "Quantitative structural and textural assessment of laminar pyrocarbons through Raman spectroscopy, electron diffraction and few other techniques", 2006. *Carbon.* Vol. 44, (Issue 9), pp.1833-1844.

120. **McEvoy N, Peltekis N, Kumar S, Rezvani E, Nolan H, Keele GP, Blau WJ, Duesberg GS.** "Synthesis and analysis of thin conducting pyrolytic carbon films", 2012. *Carbon.* Vol. 50, (Issue 3), pp.1216–1226.

121. **Cuesta A, Couto A, Rincon A, Perez MC, Lopez-Cudero A, Gutierrez C.** "Potential dependence of the saturation CO coverage of Pt electrodes: The origin of the pre-peak in CO-stripping voltammograms. Part 3: Pt(poly)", 2006. *Journal of Electroanalytical Chemistry.* Vol. 586, (Issue 2), pp.184–195.

122. **Vidaković T, Christov M, Sundmacher K.** "The use of CO stripping for in situ fuel cell catalyst characterization", 2007. *Electrochimica Acta.* Vol. 52 , (Issue 18), pp.5606–5613.

123. **Chen D, Tao Q, Liao LW, Liu SX, Chen YX, Ye S.** "Determining the Active Surface Area for Various Platinum Electrodes", 2011 . *Electrocatalysis.* Vol. 2, (Issue 3), pp.207-219.

124. **Malvern Instruments Ltd.** "Zeta potential - An introduction in 30 minutes". Version 3 Technical Note, Downloaded from: www.malvern.com/en/support/resource-center/technical-notes/TN101104ZetaPotentialIntroduction.aspx, Accessed: May 21 2015.

125. **Escubed Ltd.** "Zeta Potential – Electrophoresis". Downloaded from: www.escubed.co.uk/sites/default/files/zeta_potential_%28an011%29_elecrophoresis.pdf, Accessed: May 21 2015.

126. **Sebastián D, Suelves I, Moliner R, Lázaro MJ.** "The effect of the functionalization of carbon nanofibers on their electronic conductivity", 2010. Vol. 48, (Issue 15), pp.4421–4431.

127. **Córdoba JM, Tamayo-Ariztondo J, Molina-Aldareguia JM, Elizalde MR, Odén M.** "Morphology influence of the oxidation kinetics of carbon nanofibers", 2009. *Corrosion Science.* Vol. 51, (Issue 4), pp.926–930.

128. **Guterman VE, Belenov SV, Krikov VV, Vysochina LL, Yohannes W, Tabachkova NY, Balakshina EN.** "Reasons for the Differences in the Kinetics of Thermal Oxidation of the Support in Pt/C Electrocatalysts", 2014. *The Journal of Physical Chemistry C.* Vol 118, (Issue 41), pp.23835−23844.

129. **Stevens DA, Dahn JR.** "Degradation of the carbon support in carbon supported electro-catalysts for PEM Fuel Cells", 2003. *The Electrochemical Society.* 204th Meeting, Abs. 1022.

130. **McKee, DW.** "Metal oxides as catalysts for the oxidation of graphite", 1970. *Carbon.* Vol.8, (Issue 5), pp.623–626.

131. **Kim TH, Park MH, Ryu J, Yang CW.** "Oxidation mechanism of nickel oxide/carbon nanotube composite", 2013. *Microscopy and Microanalysis.* Vol. 19, pp.202-206.

132. **Stefov V, Najdoski M, Bogoeva-Gaceva G, Buzarovska A.** "Properties assessment of multiwalled carbon nanotubes: A comparative study", 2014. *Synthetic Metals.* Vol. 197, pp.159–167.

133. **Arepalli S, Nikolaev P.** Thermogravimetric Analysis (TGA). [book auth.] Hooker S, Migler K, Arepalli S Freiman S. *"Measurements Issues in Single WallCarbon Nanotubes".* Washington : National Institute of Standards and Technology, SpecialPublication, 2008, p. 8.

134. **Zenyuk IV, Litster S.** "Spatially Resolved Modeling of Electric Double Layers and Surface Chemistry for the Hydrogen Oxidation Reaction in Water-Filled Platinum−Carbon Electrodes", 2012. *Journal of Physical Chemistry C.* Vol. 116, pp.9862-9875.

135. **Klein DJ, Bytautas L.** "Graphitic Edges and Unpaired π-Electron Spins", 1999. *Journal of Physical Chemistry A.* Vol 103, (No. 26), pp.5196-5210.

136. **Sing, KSW.** "Physisorption of Nitrogen by Porous Materials", 1995. *Journal of Porous Materials.* Vol.2, (Issue 1), pp.5-8.

137. **Brunauer S, Emmett PH and Teller E.** "Adsorption of Gases in Multimolecular Layers", 1938. *Journal of the American Chemical Society.* Vol. 60 , (Issue 2), pp.309–319.

138. **Sing, KSW.** "Reporting Physisorption Data For Gas/Solid Systems", 1982. *Pure & Applied Chemistry.* Vol.54, (No.11), pp.2201-2218.

139. **Chang S-S, Clair B, Ruelle J, Beauchene J, Renzo FD, Quignard F, Zhao G-J, Yamamoto H, Gril J.** "Mesoporosity as a new parameter for understanding tension stress generation in trees", 2009. *Journal of Experimental Botany.* Vol.60, (no. 11), pp.1-8.

140. **Y Saito, T Yoshikawa.** "Bamboo-shaped carbon tube filled partially with nickel", 1993. *Journal of Crystal Growth.* Vol. 134, (Issues 1-2), pp.154-156.

141. **Winter F, Bezemer GL, van der Spek C, Meeldijk JD, van Dillen AJ, Geus JW, de Jong KP.** "TEM and XPS studies to reveal the presence of cobalt and palladium particles in the inner core of carbon nanofibers", 2005. *Carbon.* Vol. 43, (Issue 2), pp.327–332.

142. **Shin S, Jang J, Yoon SH, Mochida I.** "A study on the effect of heat treatment on functional groups of pitch based activated carbon fiber using FTIR", 1997. *Carbon.* Vol. 35, (Issue 12), pp.1739–1743.

143. **Gomez-Serrano V, Piriz-Almeida F, Duran-Valle JC, Pastor-Villegas J.** "Formation of oxygen structures by air activation. A study by FT-IR spectroscopy", 1999. *Carbon.* Vol. 37 , (Issue 10), pp.1517-1528.

144. **Moreno-Castilla C, Carrasco-Marin F, Maldonado-Hodar FJ, Rivera-Utrilla J.** "Effects of non-oxidant and oxidant acid treatments on the surface properties of an activated carbon with very low ash content", 1998 . *Carbon.* Vol. 36 , (No 1–2), pp.145–151.

145. **Moreno-Castilla C, Lopez-Ramon MV, Carrasco-Marın F.** "Changes in surface chemistry of activated carbons by wet oxidation", 2000. *Carbon.* Vol. 36, (Issue 14), pp.1995-2001.

146. **Puziy AM, Poddubnaya OI, Martínez-Alonso A, Suárez-García F, Tascón JMD.** "Synthetic carbons activated with phosphoric acid: I. Surface chemistry and ion binding properties"Synthetic carbons activated with phosphoric acid: I. Surface chemistry and ion binding properties", 2002. *Carbon.* Vol.40, (Issue 9), pp.1493–1505.

147. **Russo C, Stanzione F, Tregrossi A, Ciajolo A.** "Infrared spectroscopy of some carbon-based materials relevant in combustion: Qualitative and quantitative analysis of hydrogen", 2014. *Carbon.* Vol. 74, pp.127–138.

148. **Teng L-h, Tang T-d.** "IR study on surface chemical properties of catalytic grown carbon nanotubes and nanofibers", 2008. *Journal of Zhejiang University SCIENCE A.* Vol. 9, (Issue 5) pp.720-726.

149. **Ferrari AC, Robertson J.** "Resonant Raman spectroscopy of disordered, amorphous, and diamondlike carbon", 2001. *Physical Review B.* Vol. 64, pp.1-13.

150. **Jawhari T, Roid A, Casado J.** "Raman spectroscopic characterization of some commercially available carbon black materials", 1995. *Carbon.* Vol. 33, (Issue 11), pp.1561–1565.

151. **Vollebregt S, Ishihara R, Tichelaar FD, Hou Y, Beenakker CIM.** "Influence of the growth temperature on the first and second-order Raman band ratios and widths of carbon nanotubes and fibers", 2012. *Carbon.* Vol. 50, (Issue 10), pp.3542–3554.

152. **Kostecki R, Tran T, Song X, Kinoshita K, McLarnon F.** "Raman Spectroscopy and Electron Microscopy of Heat-Treated Petroleum Cokes for Lithium-Intercalation Electrodes", 1997. *Journal of The Electrochemical Society.* Vol. 144, (No 9), pp. 3111-3117.

153. **Ungar T, Gubicza J, Ribarik G, Pantea C, Zerda TW Carbon.** "Microstructure of carbon blacks determined by X-ray diffraction profile analysis", 2002. *Carbon.* Vol. 40, (Issue 6), pp.929–937.

154. **Zickler GA, Smarsly B, Gierlinger N, Peterlik H, Paris O.** "A reconsideration of the relationship between the crystallite size La of carbons determined by X-ray diffraction and Raman spectroscopy", 2006. *Carbon.* Vol. 44, (Issue 15), pp.3239–3246.

155. **Ferrari AC, Robertson J.** "Interpretation of Raman spectra of disordered and amorphous carbon", 2000. *Physical Review B.* Vol. 61 , (No 20), pp.14095-14107.

156. **Ishida H, Fukuda H, Katagiri G, Ishitani A.** "An application of surface-enhanced Raman scattering to the surface characterization of carbon materials", 1986 . *Applied Spectroscopy.* Vol. 40 , (no 3), pp.322-330.

157. **Soin N, Roy SS, Ray SC, McLaughlin JA.** "Excitation energy dependence of Raman bands in multiwalled carbon nanotubes", 2009. *Journal of Raman Spectroscopy.* Vol. 41 , (Issue 10), pp.1227–1233.

158. **Wang Y, Alsmeyer DC, McCreery RL.** "Raman Spectroscopy of Carbon Materials: Structural Basis of Observed Spectra", 1990. *Chemistry of Materials.* Vol. 2 , (Issue 5), pp.557–563.

159. **Choi YC, Min K-I, Jeong MS.** "Novel Method of Evaluating the Purity of Multiwall Carbon Nanotubes Using Raman Spectroscopy", 2013 . *Journal of Nanomaterials.* Vol. 2013, (No. 2), pp.1-6.

160. **Ferrari, AC.** "Raman spectroscopy of graphene and graphite: Disorder, electron–phonon coupling, doping and nonadiabatic effects", 2007. *Solid State Communications.* Vol 143, (Issue 1-2), pp.47–57.

161. **Tuinstra F, Koenig JL.** "Raman Spectrum of Graphite", 1970. *The Journal of Chemical Physics.* Vol. 53, (Issue 3), pp.1126-1130.

162. **Jiang N, Rama Rao KS, Jin M-J, Park S-E.** "Effect of hydrogen spillover in decalin dehydrogenation over supported Pt catayst", 2012. *Applied Catalysis A: General .* Vol. 425-426, pp.62-67.

163. **Chambers A, Nemes T, Rodriguez NM, Baker RTK.** "Catalytic Behavior of Graphite Nanofiber Supported Nickel Particles. 1. Comparison with Other Support Media", 1998. *The Journal of Physical Chemistry B.* Vol. 102, (Issue 12), pp. 2251-2258.

164. **Sepúlveda-Escribano A, Coloma F, Rodríguez-Reinoso F.** "Platinum catalysts supported on carbon blacks with different surface chemical properties", 1998. *Applied Catalysis A: General.* Vol. 173, (Issue 2), pp.247-257.

165. **Orts JM, Gomez R, Feliu JM, Aldaz A, Clavilier J.** "Potentiostatic charge displacement by exchanging adsorbed species on Pt(111) electrodes-acidic electrolytes with specific anion adsorption", 1994 . *Electrochimica Acta.* Vol. 39, (No 11/12), pp.1519-1524.

166. **Mayrhofer KJJ, Arenz M, Blizanac BB, Stamenkovic V, Ross PN, Markovic NM.** "CO surface electrochemistry on Pt-nanoparticles: A selective review", 2005. *Electrochimica Acta.* Vol. 50, (Issues 25–26), pp.5144–515.

167. **Maillard F, Schreier S, Hanzlik M, Savinova ER, Weinkauf S, Stimming U.** "Influence of particle agglomeration on the catalytic activity of carbon-supported Pt nanoparticles in CO monolayer oxidation", 2005. *Physical Chemistry Chemical Physics.* Vol. 7, (Issue 2), pp.385-393.

168. **Inkaew, P.** "Electrochemistry of carbon monoxide on platinum single-crystal surfaces", 2008. *Texas Tech University.* pp.58,78.

169. **Morimoto Y, Yeager EB.** "CO oxidation on smooth and high area Pt, Pt-Ru and Pt-Sn electrodes", 1998. *Journal of Electroanalytical Chemistry.* Vol. 441 , (Issue 1-2), pp.77-81.

170. **Maillard F, Savinova ER, PA Simonov, Zaikovskii VI, Stimming U.** "Infrared Spectroscopic Study of CO Adsorption and Electro-oxidation on Carbon-Supported Pt Nanoparticles: Interparticle versus Intraparticle Heterogeneity", 2004. *Journal of Physical Chemistry B.* Vol. 108 , (Issue 46), pp.17893-17904.

171. **Schlatter JC, Boudart M.** "Hydrogenation of ethylene on supported platinum", 1972. *Journal of Catalysis.* Vol. 24 , (Issue 3), pp.482–492.

172. **Zaera F, Somorjai GA.** "Hydrogenation of ethylene over platinum (111) single-crystal surfaces", 1984. *Journal of the American Chemical Society.* Vol. 106 , (Issue 8), pp.2288–2293.

173. **Rioux RM, Komor R, Song H, Hoefelmeyer JD, Grass M, Niesz K, Yang P, Somorjai GA.** Kinetics and mechanism of ethylene hydrogenation poisoned by CO on silica-supported monodisperse Pt nanoparticles, 2008. *Journal of Catalysis.* Vol. 254, (Issue 1), pp.1–11.

174. **Li Q, Sui Zh, Zhou X, Chen D.** "Kinetics of propane dehydrogenation over Pt–Sn/Al2O3 catalyst", 2011. *Applied Catalysis A: General.* Vol. 398, (Issue 1–2), pp.18–26.

175. **Falicov LM, Somorjai GA.** "Correlation between catalytic activity and bonding and coordination number of atoms and molecules on transition metal surfaces: Theory and experimental evidence", 1985. *Proceedings of the National Academy of Sciences.* Vol. 82, (Issue 8), pp.2207-2211.

176. **Babar VP, Jaiswal S, Kumar V.** "Interaction of a carbon atom on small platinum clusters and its effects on hydrogen binding", 2013. *Chemical Physics Letters .* Vol. 560, pp.42–48.

Journal Paper

The role of carbon support for propane dehydrogenation over platinum catalysts

Andrey Volynkin, Magnus Rønning, Edd Anders Blekkan*

Department of Chemical Engineering, Norwegian University of Science and Technology (NTNU), 7491 Trondheim, Norway.

*Corresponding author. Tel.: +47 73594157; fax: +4773594080; E-mail: edd.a.blekkan@ntnu.no

Abstract

Carbon-supported Pt catalysts were prepared by depositing the metal from a suspension of Pt nanoparticles on a range of different carbon supports. The catalysts were characterized using a range of techniques. The results show that transmission electron microscopy (TEM) and CO stripping by cyclic voltammetry (CV) give consistent values for platinum dispersion for platinum catalysts supported by carbon nanofibers and carbon nanotubes. There were some discrepancies between the techniques for Pt/graphite and Pt/carbon black, possibly due to issues with mass transfer limitations, the particle size distributions and TEM resolution. The hydrogenation of ethene, a facile reaction, was also used as a characterization tool to verify the catalyst dispersion (and available metal surface area). The results from the hydrogenation of ethene were consistent with the results from TEM and cyclic voltammetry. In catalytic dehydrogenation of propane the Pt/carbon black showed higher conversion and turnover frequency (TOF) than the catalysts prepared using carbon nanofibers, carbon nanotubes, and graphite as support. The propane dehydrogenation reaction over Pt/carbon black also showed less deactivation in experiments without hydrogen in the feed. The difference in activity and stability can be due to metal support interactions, causing changes in the electronic properties of platinum or a possible phase restructuring of the metal surface due to a strong interaction with the supports.

1. Introduction

Carbon materials have many unique properties, making them attractive for a range of applications, including as catalyst supports or even as catalysts on their own [1]. Those materials offer great flexibility because of the chemical (surface functional groups) and physical (surface area and porosity) properties of carbons can be modified to meet different requirements [2]. The electrical conductivity of carbons, as well as availability and relative inertness, makes them useful as electrocatalyst support [3]. Another useful property of carbon materials for large scale application as a catalyst support for noble metals is the possibility of easy recovery of those metals by burning of carbon [4]. Discovery of nanostructured carbons has opened new possibilities for catalysis. For example since the structure of those materials can be modified at nano-level, new effects as nano-confinement can be studied [5]. However, carbons have some severe deficiencies limiting their applications compared to more conventional supports as alumina or silica. Carbons are chemically unstable in oxidative environments and this not only limits their application in high-temperature oxidative processes, but also prevents regeneration of coked catalyst by oxidative treatment. In spite of this, Zhi-jun Sui et al. [6] have demonstrated that vulnerability of carbon nanofibers to oxidative reactions during oxidative dehydrogenation of propane can be somewhat reduced by a post-production treatment of carbons with phosphate. Another problem is the high cost of some nanostructured carbon materials, as for example, single-walled carbon nanotubes (SWCNT) [1]. Other problems with carbon materials include potential health hazards associated with particle inhalation of some nanostructured carbons such as carbon nanotubes (CNTs) [7]. In addition, the low density of some carbons makes the materials fluffy and staining, and therefore making handling those materials more complicated. But in spite of those disadvantages, carbon supported catalysts have found their way into several commercial applications, including fuel cell electrodes [8] and in liquid phase processes [9]. Rapid

development in the field of carbon materials gives importance to the development of new methods for carbon (supported) catalysts characterization.

A common procedure used to determine dispersion of supported platinum catalysts is H_2 chemisorption. Unfortunately, this method can be susceptible to complicating effects such as spillover, especially in catalysts with a small particle size of the catalyst metal [10]. Therefore, alternative methods like CO chemisorption, transmission electron microscopy (TEM), and CO stripping by cyclic voltammetry (CV) can be applied. CO stripping voltammetry is a common method in electrocatalysis and is often used for characterization of fuel cell electrode catalysts [11]. It is less commonly used in conventional heterogeneous catalysis in spite of being cheaper than alternative methods like TEM. In this work both of those methods as well as scanning electron microscopy (SEM), catalytic propane dehydrogenation and ethene hydrogenation tests, Raman and Fourier transform infrared spectroscopy (FTIR), nitrogen physisorption, and elemental analysis by inductively coupled plasma mass spectrometry (ICP-MS) have been applied to characterize a set of different carbon-supported Pt catalysts.

2. Experimental

2.1 Materials and catalyst preparation

Catalysts were prepared with 5 different commercially available carbon supports: synthetic graphite (sample code is graphite) supplied by Sigma-Aldrich, platelet nanofibers (PlCNF) supplied by Chiron AS, VULCAN® XC-72R Carbon Black (sample code carbon black) supplied by Cabot Corporation, PR-25-XT-HHT graphitized conical platelet carbon nanofibers (CPCNF) supplied by Sigma-Aldrich, and multiwall carbon nanotubes (MWCNT)

supplied by Chengdu Organic Chemicals Co. Ltd. A description of those carbons is given in Table 1. Carbon-supported catalysts with nominal loading of 1.0 wt% platinum were prepared by a modified polyol method that was developed by Tsypkin et al. [12] and further described by Kvande et al. [13]. This procedure consists of two steps, first platinum nanoparticles are prepared in a suspension, before the particles are loaded on to the supports. Since platinum particles from the same colloid suspension can be deposited on different supports, this method is well suited to study the support effects.

In the first step, hexachloroplatinic acid hexahydrate (0.644 g, $H_2PtCl_6*6H_2O$, Sigma-Aldrich) was dissolved in ethylene glycol (288 ml, EG, Fluka), and 1.0 M solution of NaOH (Merck) in EG (32.0 ml) was added to the mixture. The mixture was first heated to 423 K for three hours to reduce platinum while stirred and purged with Argon (99.999%), and then cooled down to 298 K. In the second step, a part of the Pt/EG suspension (40 ml) was sonicated for 5 minutes, heated to 423 K while stirred and purged with Ar. Then the suspension was cooled down to 298 K. After cooling, the support material (3.00 g) and Ar purged ethanol (60 ml, 96%) have been added to the Pt/EG suspension and the mixture have been sonicated for approx. 10 minutes. Then pH was reduced with HCl solution (10.0 ml, 0.54 M, Merck) to 3.2 ± 0.1 and this mixture was sonicated again for 10 minutes. The deposition was done by allowing the suspension to stand at 333 K with Ar purge for 16 hours while stirred. Then the catalyst was extracted by centrifugation, washed with Milli-Q water and acetone, and then dried in air overnight at 343 K.

2.2 Catalyst characterization

Nitrogen (99.999%) physisorption measurements were performed at 77 K using a Micromeritics 3000 Tristar II instrument. Before measurement, samples were degassed at 473 K at a pressure below 250 mTorr for 18 hours. The surface area was calculated by the Brunauer-Emmet-Teller (BET) method. The microporosity was determined by the t-plot method while the total pore volume was determined by the Barrett-Joyner-Halenda (BJH) method. Elemental analysis was done by first burning catalyst samples (approx. 400 mg) in air at 1173 K to remove carbon, then the remaining ash was dissolved with freshly prepared aqua regia, a 1:3 mixture of HNO_3 (65%, Merck) and HCl (37%, Merck), and heated to boiling before dilution with Milli-Q water to 500 ml. The solution was analyzed for Pt, Ni, Fe, and Cu content using an ELEMENT2 High Resolution ICP-MS. Scanning electron microscopy (SEM) images (micrographs) were recorded on a Hitachi S-5500 electron microscope by scattered electrons (SE) at 30.0 kV in high vacuum mode. Samples were dispersed in ethanol (96%) and sonicated for approx. 5 minutes in an ultrasonic bath. The mixture was transferred to an aluminium sample holder and dried in air at room temperature. Transmission electron microscopy (TEM) micrographs were recorded using a JEOL JEM-2010 electron microscope. Samples were dispersed in isopropanol (99.9%, VWR) and sonicated for 5 minutes in an ultrasonic bath before deposited on holey carbon TEM grids and dried at room temperature. Average particle size and particle size distribution was obtained by measuring between 196 and 463 particles from 3-6 representative micrographs of each sample. The dispersion was calculated from the particle size using equation 1:

$$D = \frac{\sum_{i=1}^{n} \frac{1.13}{d_i}}{n} \qquad (1)$$

where D is platinum dispersion, d_i is particle size of particle i in nanometers, and n is the number of measured particles in a sample. To avoid an overestimation of dispersion for small particles, the dispersion value of 1 was used for particles with a measured size of less than 1.13 nm. This equation assumes spherical particles, as done by Aramendia et al. [14], and atom density on Pt surface of 1.24×10^{15} atoms/cm^2. This is the average atom density of (111), (100), and (110) crystal faces, as reported by Will [15]. Raman spectra were recorded on a Horiba Jobin Yvon LabRAM HR 800 in air at room temperature and with a 632.8 nm He-Ne laser with an effect of 30 mW as the excitation source. Diffuse reflectance infrared Fourier transform spectroscopy (DRIFTS) spectra were collected on a Nicolet iS50 FT-IR with 32 scans at 4 cm^{-1} resolution. Sample material was diluted by spectroscopy grade potassium bromide (KBr, Merk, for spectroscopy) and ground in an agate mortar. The background spectrum from pure KBr was subtracted. In addition, CO_2 and H_2O bands were removed by the OMNIC 9.2.86 software. Cyclic voltammetry (CV) experiments were done with a VersaSTAT MC potentiostat with VersaStudio software. Samples were dispersed in Milli-Q water and ethanol (3:2 water to ethanol ratio). The concentration of the sample in the suspension was 1.0 mg per ml suspension. The suspension was sonicated until homogenous and 90 µg of catalyst was deposited on a glassy carbon electrode and then dried in N_2 (99.999%) flow. After deposition and drying, 15 µl of Nafion® solution (0.5% in light alcohols diluted to 0.05% with ethanol) was deposited on a disk-type glassy carbon electrode and dried again. The electrochemical cell was filled with H_2SO_4 solution (150 ml, 0.5 M) as electrolyte. This electrolyte was purged with N_2 for approx. 30 minutes prior to measurement. The reversible H_2 electrode (RHE) which is a subtype of the standard hydrogen electrode (SHE) was used as reference electrode, a platinum wire was used as counter (auxiliary) electrode, and a glassy carbon electrode with deposited sample on was used as working electrode. The working electrode was electrochemically preconditioned from 0.05 to 1.20 V

first at a scan rate 0.100 V/s and then at a scan rate 0.010 V/s. After conditioning the potential was kept at 0.05 V, and CO (99.3%) gas was bubbled through the electrolyte for 5 minutes. Then nitrogen was bubbled through the electrolyte for 30 minutes at this potential to remove excess CO and adsorbed CO was stripped at scan rate 0.010 V/s. It was assumed that the charge density for oxidation of the monolayer value is 0.420 mC/cm^2, as commonly done in the literature [16,17,18] and this value was assumed to be independent of the particle dispersion. It was also assumed that double layer charging and oxide formation was similar with and without adsorbed CO. Therefore, the stripping area $Q_{CO\_oxidation}$ was obtained by subtracting the voltammogram obtained without CO adsorbed (second cycle) from the voltammogram obtained with CO (first cycle). Catalyst dispersion was calculated by first calculating number of active platinum atoms according to equation 2,

$$N_{activePt} = \frac{Q_{CO\_oxidation} \times \rho_{surface\_Pt}}{Q \times R} \tag{2}$$

where $Q_{CO\_oxidation}$ is the stripping area $\rho_{surface\_Pt}$, is atom density on Pt surface, Q is the charge density for oxidation of the CO monolayer and R is the stripping scan rate. Then, the dispersion was calculated using equation 3,

$$Disp = \frac{N_{activePt}}{N_A \dfrac{m_{Cat} X_{Pt}}{M_{Pt}}} \tag{3}$$

where N_A is Avogadro`s number, m_{Cat} is catalyst mass, X_{Pt} is catalyst loading, and M_{Pt} is the molar mass of platinum.

2.3 Catalytic testing

The catalytic tests were performed at atmospheric pressure in a tubular fixed bed quartz reactor were the catalyst powder was placed on a quartz frit (pore size 40-90 μm) and held in place with quartz wool. The reactor was heated by an electrical oven controlled using a thermocouple placed in the catalyst bed. Before the catalytic tests, catalyst samples were reduced in He (99.996%), H_2 (99.999%), and N_2 (99.999%) flow in 50:25:25 ratio with a total flow of 103 ± 3 ml/min while heated to 773 K. The heating time from 298 K to 773 K was 50 minutes. The gaseous products were analyzed by an Agilent 3000 Micro Gas Chromatograph with a TCD detector. Nitrogen was used as internal standard for the calculation of C_3H_8 conversion and selectivities to products. Selectivities are reported as C-based values. Dehydrogenation of propane was carried out at 773 K with feed gases H_2 (99.999%), C_3H_8 (99.3%), and N_2 (99.999%) in 0:28:78 and 4.4:28:70 ratios. Sample weight was 0.100 g, and catalyst bed was not diluted. Ethene hydrogenation experiments were done at 373 K. The catalyst (0.0050 g) was diluted by 1.0000 g of silicon carbide (Powder, particle size between 90 μm and 53 μm) loaded in the reactor and reduced the same way as for propane dehydrogenation. The feed composition for catalyst testing was H_2 (99.999%), C_2H_4 (99.95%), and N_2 (99.999%) in 15:10:75 ratio. Conversions were compared after 60 minutes on stream to allow the reaction temperature to stabilize. In order to compare with the chemical equilibrium, the simulation data for propane dehydrogenation were calculated with UniSim Design R400 software. The modeled reaction temperature was 773 K, and the reaction pressure was 1.0 atm. Only the propane dehydrogenation reaction to hydrogen and propene was considered. The Peng–Robinson equation of state and conditions of equilibrium reactor were used in the simulation.

3. Results and discussion

3.1. Catalyst support composition and structure

The elemental analysis has shown that all supports except for PlCNF did not contain a significant amount of typical growth catalyst metal as Ni, Cu or Fe, as presented in Table 1.

Table 1 Composition of catalysts and catalyst supports

Sample code	Support material	Ni wt%	Cu wt%	Fe wt%	Pt wt%
Pt/carbon black	VULCAN® XC-72R, Carbon black	<0.001	0.003	<0.002	0.82
Pt/MWCNT	TNGM7, Graphitized Multi-walled Carbon nanotubes	<0.001	0.002	<0.002	0.84
Pt/PlCNF	06-0170 Carbon, stacked graphene platelet nanofibers (acid washed)	0.31	0.11	<0.002	0.81
Pt/CPCNF	PR-25-XT-HHT, graphitized (iron-free), composed of conical platelets	<0.001	0.007	<0.004	0.77
Pt/graphite	Synthetic graphite powder, particle size <20 μm	<0.001	0.002	<0.004	0.78

The impurity of Ni and Cu in PlCNF sample originated from the growth catalyst used to produce this material. However, those impurities did not give any measurable catalytic activity in catalytic tests with carbon supports not loaded with platinum. The measured platinum loading for all catalysts was slightly lower than the nominal loading of 1.0% of platinum and was found to be in the range 0.77-0.84%. In the polyol method, the relation between the actual loading and the nominal loading is controlled by the pH [19]. In a basic suspension (containing glycolate anion and hydroxyl ion) the platinum particles are repelled from each other and from the support. At low pH, the repulsive forces become weaker, and

the actual loading on the support would get closer to the nominal, at the cost of particle dispersion. In this work, the pH at the Pt deposition step (pH 3.2 ± 0.1) gave high dispersion at the cost of some loading.

The BET surface area of high surface area supports (carbon black and PlCNF) was slightly reduced by the platinum deposition as seen in Table 2. The reduction of the surface area of those supports can be explained by clustering of support particles during drying.

Table 2 Surface area and porosity of catalysts and catalyst supports

Samples	BET surface area (m^2/g)	Pore Volume[1] (cm^3/g).	Micropores t-plot (cm^3/g)
Carbon black	230	0.18	0.037
Pt/carbon black	218	0.18	0.035
MWCNT	74	0.11	0.001
Pt/MWCNT	73	0.12	0.001
PlCNF	186	0.18	0.008
Pt/PlCNF	180	0.18	0.007
CPCNF	20	0.03	0.000
Pt/CPCNF	20	0.03	0.001
graphite	9	0.01	0.000
Pt/graphite	9	0.01	0.000

Note: 1. BJH Adsorption cumulative volume of pores between 17 Å and 3000 Å diameter (cm^3/g).

Figures 1 - 3 show TEM and SEM images of the samples. Fig. 1 shows the structures of the nanostructured catalysts. Pt/CPCNF presented well-defined carbon nanofibers with high aspect ratios (Fig. 1a) and the TEM image of the same sample (Fig. 1b) shows a hollow fiber with platinum particles deposited both on the inner and outer surfaces of the fiber. The SEM

image of Pt/PlCNF (Fig. 1c) shows poorly defined carbon nanofibers with low aspect ratios and the TEM image of the same sample (Fig. 1d) shows one such fiber with Pt particles deposited on. The SEM image of Pt/MWCNT (Fig. 1e) shows entangled carbon nanotubes and the TEM image of this sample (Fig. 1f) shows Pt particles deposited on those carbon nanotubes.

Similar images of not-nanostructured catalyst samples are shown in Figure 2. The SEM image of Pt/carbon black (Fig 2g) shows agglomerated carbon black particles and the TEM image of Pt/carbon black (Fig. 2h) shows Pt particles deposited on those carbon black particles. Similarly are the graphite particles in Pt/graphite shown in the SEM image in Fig. 2i, and the TEM image of the same sample (Fig. 2j) shows Pt particles deposited on those graphite particles.

Carbon black and PlCNF contained small particles with a low aspect ratio, as seen in Fig. 1 and Fig. 2, and therefore clustering of support particles in those samples has more significant effect on surface area than clustering of bigger particles (graphite) or clustering (entanglement) of fibers with high aspect ratio (MWCNT and CPCNF). The SEM images (Fig. 1) show that MWCNT and CPCNF have a regular shape with diameters of 20-50 nm and 100-200 nm respectively. On the other hand, PlCNF is irregular in shape and has a low aspect ratio.

The multiwall structure for carbon nanotubes was confirmed by TEM (Fig. 3) while both PlCNF and CPCNF have both crystalline and amorphous regions. The TEM images (Fig. 1d and Fig. 3) show that PlCNF consists of graphitic layers, but due to structural defects not all layers are perpendicular to the principal (fiber direction) axis. A large fraction of CPCNF fibers consisted of conical platelet fibers inside a MWCNT like structure, while the structure of walls of other CPCNF fibers was not as clear (Fig. 1b and Fig. 3).

FTIR results (Fig. 4) do not show any significant presence of oxygen-containing functional groups except for -OH. The typical oxygen-containing functional groups found on carbon surfaces are anhydrides, ketones, aldehydes, esters, quinones, carboxylic acids, ethers, lactones, and phenols. Anhydrides have been reported to give a band at 1880-1740 cm^{-1} by Shin et al. [20]. The stretching mode of ketonic C=O groups of ketones, aldehydes, and esters would appear at 1740 cm^{-1} if those groups are not conjugated with a double band or aryl group [21]. Conjugated ketones or quinones appear at 1670-1660 cm^{-1} [20,22,23]. Aromatic carboxyl acid group would give a band in 1700-1680 cm^{-1} region and are affected by different peripheral functional groups, and the non-aromatic carboxyl acid groups have been reported to give a band at 1712 cm^{-1} [20]. Ether type structures would give C-O stretching vibration bands at 1245 cm^{-1} and 1160 cm^{-1} [21]. Lactones have been reported to appear at 1740-1710 cm^{-1} and 1264-1260 cm^{-1} and the phenolic groups would appear in the 1200-1100 cm^{-1} region [20,21]. The oxygen-containing functional groups can be introduced by various oxidative treatments and can affect the metal dispersion and catalytic properties. Prado-Burguete et al. [24] have reported that the presence of heteroatoms (e.g. oxygen) on the surface of carbon supports can have a positive effect on Pt dispersion when an impregnation method is used, by anchoring metal particles to the surface and preventing them from agglomeration and by making the carbon surface less hydrophobic. However, other studies [18,25,26] reported that for the modified polyol method better dispersion can be achieved if carbon has a low content of acidic oxygen-containing functional groups. This is especially important if an anionic platinum precursor is used, as $[PtCl_6]^{2-}$, since it will be repelled from the negatively charged oxygen-containing functional groups on the carbon surface. The broad band at 3434 cm^{-1} can be assigned to hydroxyl stretching vibrations of the OH- groups and adsorbed water, as observed by Gomez-Serrano et al. [21] and Puziy et al. [27]. The width of this band indicates involvement of the hydroxyl groups in hydrogen bonding. Bands at 2955 cm^{-1}, 2921 cm^{-1}, and

2854 cm^{-1} can be assigned to CH_3 and CH_2 stretching vibrations as observed by Gomez-Serrano et al. [21], Puziy et al. [27] and Russo et al. [28]. Two very weak bands, at 1736 cm^{-1} and at 1702 cm^{-1}, have been observed for all supports, as seen in Fig. 4, however those bands are too weak to firmly identify them as ketone or carboxyl groups. The band at 1628 cm^{-1} can be assigned to adsorbed water on the KBr. Teng et al.[29] have observed this band at 1630 cm^{-1}. A small shoulder of this band can be observed at 1654 cm^{-1} and has been attributed to C=C stretching at terminal olefinic bonds [21]. The band at 1462 cm^{-1} can be attributed to the asymmetrical bending (scissor) mode of CH_3 and CH_2 groups and has been reported by Gomez-Serrano et al. [21] and Teng et al. [29]. The band at 1382 cm^{-1} can be assigned to CH_2 and CH_3 bending vibrations, as observed by Gomez-Serrano et al. [21] and Russo et al. [28]. Pt/carbon black and Pt/PlCNF background spectra are sloping down to lower wavenumbers. This could be due to scatter from sample particles causing deeper light penetration at the longer wavelengths (low wavenumbers). The presence of bending and stretching modes of C-H can be clearly observed for all samples indicating that all supports, including carbon nanotubes and fibers contain defects. The degree of disorder in carbon supports can be assessed from Raman spectra, presented in Fig. 5. The G band, which is observed in the range 1585-1572 cm^{-1}, reflects the structure of sp^2 hybridized carbon and is associated with the degree of graphitization order of the carbon. The D band is observed in the range 1328-1322 cm^{-1} and is associated with the disorder of carbon. The ratio of the intensity of the G band and the D band (I_G/I_D) is often assumed to be proportional to the crystallite size (L_a) and is commonly used to assess the extent of graphitization degree of carbon materials [30-34]. However, this value is only indicative since a simple I_G/I_D comparison has many uncertainties, including a nonlinear dependence on the crystallite size when the crystal size is below 2 nm [35].

Based on the I_G/I_D band ratio, we observe the following order with increasing graphitization degree:

Pt/PlCNF (0.55)>Pt/carbon black (0.78)>Pt/MWCNT (1.47)>Pt/graphite (2.37)>Pt/CPCNF (2.97)

A small shoulder of the G band is observed at 1616 cm^{-1} in Pt/MWCNT, but this band is also present in other samples. This band is called D' and is disorder related [36], but this band is difficult to observe because of an overlap with the much stronger G band**.** The lower I_G/I_D ratio of PlCNF compared to carbon black seemingly indicates that PlCNF is more disordered than carbon black, which is known for poor crystallinity. The TEM results (Fig. 3) show that PlCNF although having many defects, consists of graphitic layers on top of each other and therefore should contain a higher concentration of sixfold rings. For disordered carbons, the intensity of the D band becomes proportional to the probability of finding a sixfold ring in a given area while the G band does not require sixfold ring. Therefore, high D band in distorted carbons can indicate ordering, which is the opposite of what is observed for more graphitic carbons [37,38].

3.2. Dispersion of Platinum

The TEM results have shown that, as expected, the deposition of platinum particles on low surface area supports, graphite, and CPCNF, resulted in comparatively large average metal particle sizes of 3.1 nm and 2.4 nm respectively, as seen in Fig. 1 and Fig. 2. On the other hand, the supports with higher surface area MWCNT, PlCNF, and carbon black had a smaller average particle size of 1.5-1.6 nm, as seen in Fig. 1 and Fig. 2. This was expected since on low surface area supports deposited particles are in closer proximity to each other. The difference between the measured average particle sizes on the high-surface area supports is not significant and almost no particles with size above 6 nm have been observed on those

supports. For Pt/PlCNF, no particles below 0.5 nm have been observed, but this could be due to limited resolution, rather than the absence of those particles. Therefore, it is possible that the true average particle size for this catalyst is below 1.5 nm. No particles with sizes above 3.5 nm were observed in this sample, indicating a god dispersion of platinum. Larger average metal particle size on graphite and CPCNF support was caused by a small number of large particles, seen as a tail on the particle size distribution histogram above 6 nm. Since all catalyst samples were prepared from the same colloidal platinum suspension, it is reasonable to assume that large particles arise from agglomeration of smaller particles. For example for graphite, the increase in the number of particles in the range 1.5-2.0 nm also came at the expense of particles in the 0-1.5 nm range. This gives the size distribution histogram, a skewed shape and indicates particle agglomeration. On Pt/CPCNF, the majority of observed particles with size above 6 nm were observed on the outer surface of the fibers. On the other hand, a majority of the particles inside the hollow fibers were between 1.0 nm and 3.5 nm in diameter. This indicates that some effects inside the fibers had an influence on the particle size distribution. The graphite planes inside the fibers are in sharp angle to the longitudinal axis of the fiber, and expose plane edges. This provides more anchoring sites for metal particles than the outer surface of the fibers, which is dominated by basal planes, as seen in Fig. 3.

Fig. 6 shows a stripping scan for adsorbed CO on the Pt/MWCNT catalyst. Similar voltammograms were obtained for the other catalysts. The region A is caused by H_2 desorption from the platinum surface. This region was not present during CO stripping, indicating that the Pt surface was occupied by CO rather than H_2. Adsorbed CO was stripped for all catalysts in the range 0.85-0.90 V against RHE. Results of particle size and dispersion measurements from TEM and CV can be seen in Table 3.

Table 3 Results showing particle size and dispersion obtained by TEM and CV. Standard deviations are given in parenthesis

Samples	Results from TEM			Results from Cyclic voltammetry	
	Particle size (nm)	Dispersion (%)	Number of measured particles	Particle size (nm)	Dispersion (%)
Pt/carbon black	1.6 (0.3)	76 (11)	463	2.1 (0.3)	54 (6)
Pt/MWCNT	1.5 (0.1)	79 (2.3)	372	1.4	79
Pt/PlCNF	1.5 (0.2)	79 (4.7)	266	1.3	87
Pt/CPCNF	2.4 (0.2)	52(3.7)	258	2.3	50
Pt/graphite	3.1 (0.8)	46 (8.4)	196	6.3 (0.7)	18 (2)

The TEM and the CV methods show a good consistency when applied to determine metal particle sizes for Pt/PlCNF, Pt/CPCNF, and Pt/MWCNF. The metal particle size for Pt/PlCNF was 1.5 nm and 1.3 nm, for Pt/MWCNT was 1.5 nm and 1.4 nm, and for Pt/CPCNF 2.4 nm and 2.3 nm measured by TEM and CV methods respectively. The difference between average particle size values obtained by these two methods is not significant for those samples. On the other hand, the discrepancy for Pt/carbon black and Pt/graphite was more severe. The larger discrepancy between the CV results and the TEM results for Pt/carbon black could have been caused by the high microporosity of this support (Table 2). The micropores of Vulcan XC-72 carbon black can be inaccessible to Nafion® micelles (>40 nm in size), reducing the electrochemical activity of platinum particles in those pores [39], leading to an underestimation of dispersion. This problem can be especially noticeable when low loadings (as in this work) are applied since a large fraction of deposited metal particles can be inaccessible due to mass transfer limitations. The discrepancy between the CV and TEM results for Pt/graphite could have been caused by difficulties in determining the average

particle size in this sample with TEM. Pronounced particle sintering can lead to a wide particle size distribution, as seen in Fig. 2. Therefore, some of the largest Pt agglomerates may not be present in the selected TEM images. In contrast to TEM, CV gives an estimate of the average particle size in the entire sample. A similar discrepancy has been reported by Vidacović et al. [16] when comparing TEM and CV methods for determining the average particle size of an unsupported platinum catalyst.

However, both methods gave the same order of the average metal particle size, as seen from Table 3:

Pt/graphite > Pt/CPCNF > Pt/carbon black > Pt/MWCNT ≈ Pt/PlCNF

3.3 Catalytic experiments

3.3.1 Ethene hydrogenation experiments

Ethene hydrogenation is a structure insensitive reaction [40,41], i.e. independent of the type of Pt crystal faces exposed. Therefore, this reaction is only dependent on the surface area of the active metal and can be used to estimate catalyst dispersion. Due to the high exothermicity of this reaction, ΔH°_{rxn}= -136 kJ mol^{-1} [42], the temperature was allowed to stabilize at 373 K after 60 min time on stream (TOS). Control tests have shown that at those conditions, the contribution from gas phase reactions and the contribution of platinum-free carbon materials was negligible. This approach assumes that catalyst deactivation (by polymerization of ethene) affects the activity of all samples equally. The order of catalyst activity reported as conversion of ethene after 60 min was:

Pt/PlCNF(68%) ≈Pt/MWCNT(68%) >Pt/carbon black(43%) >Pt/CPCNF(35%) >Pt/graphite(16%)

This order is the same as seen for dispersion obtained from TEM and CV, presented in Table 3. While the TEM indicates that Pt/carbon black has similar or slightly lower dispersion than Pt/PlCNF and Pt/MWCNT, both the CV and ethene hydrogenation methods indicate that Pt was significantly better dispersed on MWCNT and PlCNF than on carbon black. This is in in contrast to the larger BET surface area of carbon black , as seen in Table 2, and can be explained by the larger microporosity of carbon black causing diffusion limitations [26].

3.3.2 Propane dehydrogenation experiments

Experiments with empty reactor have shown that the contribution from homogeneous reactions was negligible at relevant reaction conditions (with and without H_2 in the feed). Also, experiments with platinum-free carbon supports have shown a negligible conversion. This includes PlCNF support that contained 0.31 wt% Ni and indicates that the amount of chemically accessible Ni in this support was not enough to give a measurable effect on the catalytic activity. The catalytic tests without H_2 in the feed (not shown) gave negligible conversion for all catalyst except for Pt/carbon black, which gave 10% conversion at 10 min TOS. This conversion decreased to 0.6% after 40 min TOS due to deactivation. Addition of 4.3% H_2 to the feed improved the conversion for all samples, and the conversion levels are presented in Fig. 7, indicating that without hydrogen the samples were rapidly deactivated by coking. The effect of hydrogen slowing down the deactivation rate is well known and has been observed with other Pt-based catalysts by Qing Li et al. [43]. Introduction of hydrogen at this level reduced the equilibrium conversion from 30.5% to 24.3% However, this is still above the conversion achieved by the tested catalysts, thus allowing informative comparison of catalysts to be done. The main product of propane dehydrogenation was propene, as seen from the Table 4. However, some cracking products as ethene, ethane, and methane have also been observed. The Pt/carbon black catalyst had the highest selectivity to propene, 98% after 10 minutes TOS, and the selectivity was stable after 60 minutes TOS. On the other hand,

Pt/MWCNT, Pt/PlCNF, Pt/CPCNF, and Pt/graphite had propene selectivities of 91.4%, 91.1%, 92.7%, and 93.8% respectively after 10 min TOS. This selectivity increased by 1-3% after 60 minutes, probably due to deactivation of sites responsible for cracking.

Table 4 Selectivity for different products under propane dehydrogenation with H_2

Samples	C_3H_6		C_2H_6		C_2H_4		CH_4	
	10 min	60 min	10 min	60 min	10 min	60 min	10 min	60 min
Pt/carbon black	97.7%	97.9%	1.3%	0.9%	0.1%	0.3%	0.9%	0.9%
Pt/MWCNT	91.4%	93.7%	2.5%	1.4%	1.4%	1.2%	4.7%	3.7%
Pt/PlCNF	91.1%	93.3%	3.6%	2.0%	1.5%	1.4%	3.8%	3.3%
Pt/CPCNF	92.7%	95.7%	1.6%	0.7%	2.7%	1.5%	3.0%	2.1%
Pt/graphite	93.8%	95.3%	1.2%	0.5%	2.0%	1.2%	3.0%	3.0%

The highest conversion of Pt/carbon black both with and without H_2 comes in spite of lower dispersion (available Pt surface area) on this catalyst compared to Pt/MWCNT and Pt/PlCNF as shown by TEM, CV, and ethene hydrogenation experiments. The higher stability of conversion over Pt/carbon black demonstrates a clear difference from other catalysts. This difference could be due to an effect of metal support interaction causing phase reconstruction as observed by Muthuswamy et al. [18]. They reported that platinum nanoparticles deposited on platelet CNF by the modified polyol method undergoes changes in their geometry as opposed to particles deposited on carbon black. Unfortunately, determination of Pt morphology was not possible by the available TEM instrument due to limited resolution.

The turnover frequencies (TOF) for propane dehydrogenation with H_2 in the feed were calculated using the TEM and the CV results and are presented in Table 5.

Table 5 The TOF for the propane dehydrogenation reaction after 10 min time on stream, calculated from catalyst dispersion obtained from TEM and from CV

Samples	TOF (s^{-1}) from CV dispersion results	TOF (s^{-1}) from TEM dispersion results
Pt/carbon black	1.08	0.77
Pt/MWCNT	0.35	0.35
Pt/PlCNF	0.35	0.38
Pt/CPCNF	0.32	0.31
Pt/graphite	0.59	0.23

Both types of catalyst with carbon nanofibers (Pt/PlCNF and Pt/CPCNF) and carbon nanotubes (Pt/MWCNT) show very similar TOF calculated using dispersion data from both methods. This indicates that CV and TEM can give consistent results when applied to characterize this type of catalysts and that the activity is not depending on the carbon supports for this reaction. The TOF results for Pt/graphite are not consistent, due to inconsistency in the value of measured dispersion by the TEM and the CV methods. Also, the discrepancy between the two calculated TOF values for Pt/carbon black also originates from the discrepancy in values of dispersion determined by different methods. However, both methods indicate that the propane dehydrogenation reaction over Pt/carbon black had a higher TOF than the reaction over the other catalysts. This could be due to the structural difference of the supports. VULCAN® XC-72R is a commercial carbon black, and therefore this is the only support tested that is not composed of graphene layers. Platinum support interaction is dependent on the structure of the support, and a semi-crystalline support such as carbon black will result in a weaker interaction than a crystalline support. It is not clear if the observed difference in catalytic properties of tested catalysts is caused by merely electronic effects, or

by a possible phase restructuring of the platinum particles induced by the stronger interaction with the supports.

4. Conclusions

A set of different carbon-supported Pt catalysts was prepared by depositing metal particles from a common suspension of Pt nanoparticles onto a range of different carbon supports. After depositing the Pt particles on the support, the catalysts were characterized using a range of techniques. The results show that TEM and CO stripping by CV give consistent values for platinum dispersion for platinum catalysts supported by carbon nanofibers and carbon nanotubes. There were some discrepancies between the techniques for Pt/graphite and Pt/carbon black, probably due to issues with the mass transfer limitations, the particle size distributions, and TEM resolution. The hydrogenation of ethene, a facile reaction, was also used as a characterization tool, and the results confirmed the dispersion. In catalytic dehydrogenation of propane, the Pt/carbon black showed higher conversion and TOF value than catalysts prepared using carbon nanofibers, carbon nanotubes, and graphite as support. In addition to giving a higher TOF, the propane dehydrogenation reaction over Pt/carbon black was less susceptible to deactivation in experiments without hydrogen in the feed, indicating that the carbon black support either reduces the rate of coke formation or the toxicity of the coke formed. A possible reason can be a metal support interaction, causing changes in the electronic properties of platinum or a possible phase restructuring of the metal surface due to a strong interaction with the supports.

Acknowledgements

The authors gratefully acknowledge financial support from the Gas Technology Centre NTNU-SINTEF. The assistance from prof. James McGregor at the University of Sheffield, Dr. Liam McMillan, and prof. Lynn Gladden at the University of Cambridge, Department of Chemical Engineering and Biotechnology, as well as Dr. Navaneethan Muthuswamy from NTNU, Department of Chemical Engineering is gratefully appreciated.

References

1. Su DS, Perathoner S, Centi G (2012) Catal Today 186 (1):1-6
2. T.J. Bandosz (2009) Chapter 2 In: Serp P (ed), Figueiredo JL (ed) Carbon materials for catalysis, 1st ed. Wiley, Hoboken, New Jersey
3. Uribe-Godínez J, García-Montalvo V, Jiménez-Sandoval O (2014) Int J Hydrogen Energy 39(17):9121–9127
4. Auer E, Freund A, Pietsch J, Takke T (1998) Appl Catal A Gen, 173 (2):259–271
5. Battie Y, Jamon D, Lauret JS, Gu Q, Gicquel-Guézo M, Naciri AE, Loiseau A (2014) Thin Solid Films, 571:395–398
6. Z-j Sui, J-h Zhou, Y-c Dai, W-k Yuan (2005) Catal Today 106(1-4):90-94
7. Boczkowski J, Lanonea S (2012) Adv Drug Deliv Rev 64(15):1694-1699
8. Trogadas P, Fuller TF, Strasser P (2014) Carbon 75:5-42

9. Arunajatesan V, Chen B,Mobus K, Ostgard DJ,Tacke T, Wolf D (2009) Chapter 15 In: Serp P (ed), Figueiredo JL (ed) Carbon materials for catalysis, 1st ed. Wiley, Hoboken, New Jersey
10. Tsao C-S, Tzeng Y-R, Ming-Sheng, Wang C-Y, Tseng H-H, Chung T-Y, Wu H-C, Yamamoto T, Kaneko K, Chen S-H (2010) J Phys Chem Lett 1(7):1060-1063
11. Maillard F, Simonov PA, Savinova ER (2009) Chapter 12 In: Serp P (ed), Figueiredo JL (ed) Carbon materials for catalysis, 1st ed. Wiley, Hoboken, New Jersey
12. Tsypkin M, Briskeby ST, Kongstein OE, Børresen B, Tunold R (2005) The 8th Frumkin Symposium: ''Kinetics of Electrode Processes'', Russian Academy of Science, Moscow, p.165
13. Kvande I, Briskeby ST, Tsypkin M, Ronning M, Sunde S, Tunold R, Chen D (2007) Top Catal 45(1-4):81-85
14. Aramendia MA, Borau V, Jimenez C, Marinas JM, Moreno A (1996) Colloids Surfaces A: Physicochem Eng Aspects 106(2-3):161-165
15. Will FG (1965) J Electrochem Soc 112(4):451-455
16. Vidaković T, Christov M, Sundmacher K (2007) Electrochimi Acta 52(18):5606–5613
17. Chen D, Tao Q, Liao LW, Liu SX, Chen YX, Ye S (2011) Electrocatalysis 2(3):207-219
18. Muthuswamy N, Gomez de la Fuente JL, Ochal P, Giri R, Raaen S, Sunde S, Rønning M, Chen D (2013) Phys Chem Chem Phys 15(11):3803-3813
19. H-S Oh, J-G Oh, H Kim (2008) J Power Sources 183(2):600–603
20. Shin S, Jang J, Yoon SH, Mochida I (1997) Carbon 35(12):1739–1743
21. Gomez-Serrano V, Piriz-Almeida F, Duran-Valle CJ, Pastor-Villegas J (1999) Carbon 37(10):1517-1528

22. Moreno-Castilla C, Carrasco-Marin F, Maldonado-Hodar FJ, Rivera-Utrilla J (1998) Carbon 36(1):145–151
23. Moreno-Castilla C, Lopez-Ramon MV, Carrasco-Marın F (2000) Carbon 38(14):1995-2001
24. Prado-Burguete C, Linares-Solano A, Rodriguez-Reinoso F, Salinas-Martinez de Lecea C (1989) J Catal 115(1):98-106
25. Liu Z, Duan X, Cheng H, Zhou J, Zhou X, Yuan W (2015) Carbon (89):93–101
26. Kvande I, Zhu J, Zhao T-J, Hammer N, Rønning M, Raaen S, Walmsley JC, Chen D (2010) J Phys Chem C 114(4):1752–1762
27. Puziy AM, Poddubnaya OI, Martinez-Alonso A, Suarez-Garcia F, Tascon JMD (2002) Carbon, 40(9):1493-1505
28. Russo C, Stanzione F, Tregrossi A, Ciajolo A (2014) Carbon 74:127–138
29. Teng L-h, Tang T-d (2008) J Zhejiang Univ Sci 9(5):720-726
30. Tuinstra F, Koenig JL (1970) J Chem Phys 53(3):1126–1130
31. Knight DS, White WB (1989) J Mater Res 4(2):385-393
32. Kostecki R, Tran T, Song X, Kinoshita K, McLarnon F (1997) J Electrochem Soc, 144(9):3111-3117
33. Ungar T, Gubicza J, Ribarik G, Pantea C, Zerda TW (2002) Carbon 40(6):929-937
34. Jawhari T, Roid A, Casado J (1995) Carbon 33(11):1561–1565
35. Zickler GA, Smarsly B, Gierlinger N, Peterlik H, Paris O (2006) Carbon 44(15):3239–3246
36. Vollebregt S, Ishihara R, Tichelaar FD, Hou Y, Beenakker CIM (2012) Carbon 50(10):3542-3554
37. Ferrari AC, Robertson J (2000) Phys Rev B 61(20):14095-14107
38. Ferrari AC, Robertson J (2001) Phys Rev B 64(7):1-13

39. Park SK, Shao Y, Kou R, Viswanathan VV, Towne SA, Rieke PC, Liu J, Lin Y, Wang Y (2011) J Electrochem Soc 158(3):B297-B302

40. Zaera F, Somorjai GA (1984) J Am Chem Soc 106(8):2288-2293

41. Rioux RM, Komor R, Song H, Hoefelmeyer JD, Grass M, Niesz K, Yang P, Somorjai GA (2008) J Catal 254(1):1–11

42. Aylward G, Findlay T (2002) SI Chemical Data. 5th edition, Wiley, Australia

43. Li Q, Sui Z, Zhou X, Chen D (2011) Appl Catal A Gen 398(1-2):18-26

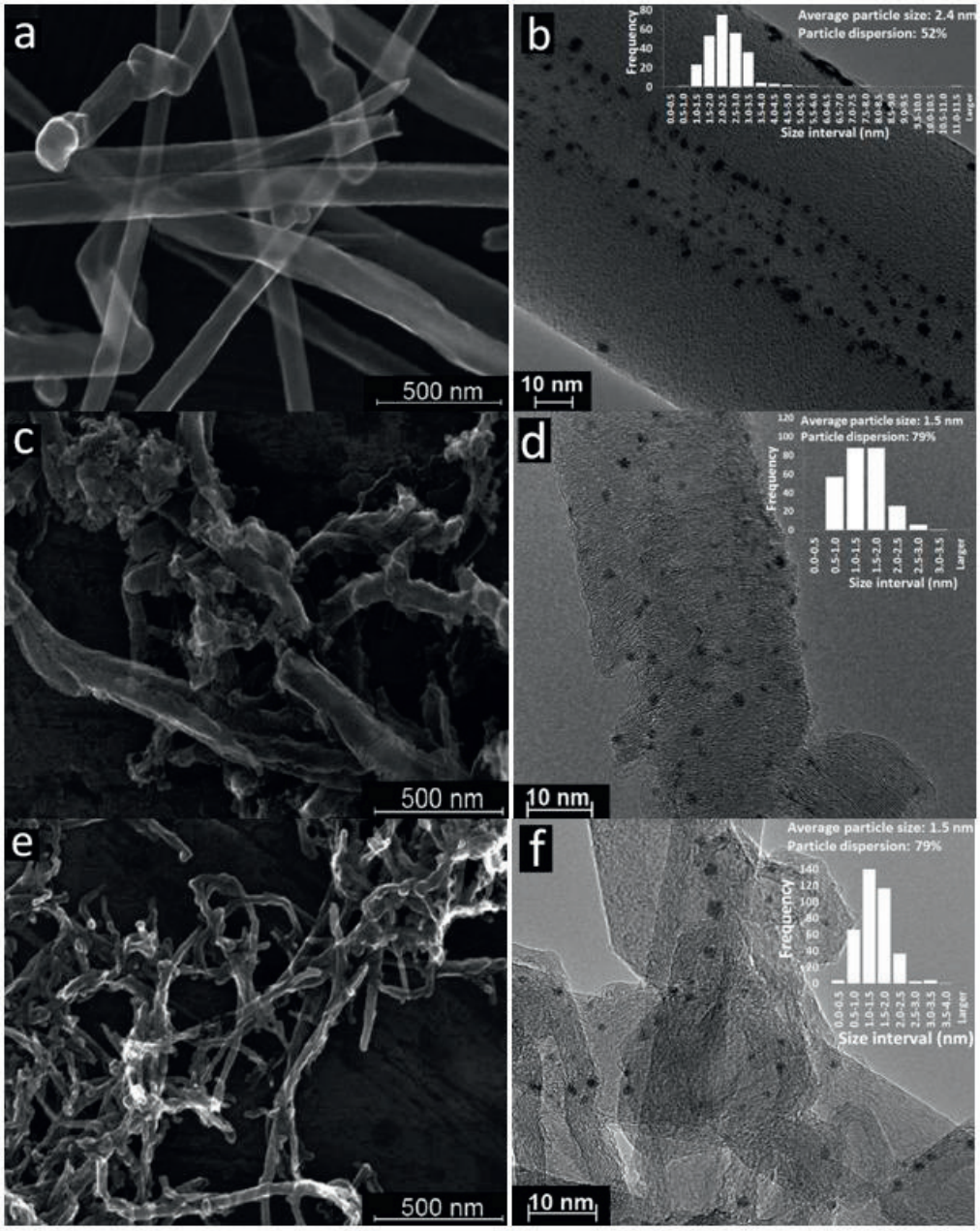

Figure 1 SEM images (left) and TEM images (right) of nanostructured catalysts with Pt particle size distributions presented in the upper right corner of the TEM images. a) and b): Pt/CPCNF c) and d): Pt/PlCNF e) and f): Pt/MWCNT.

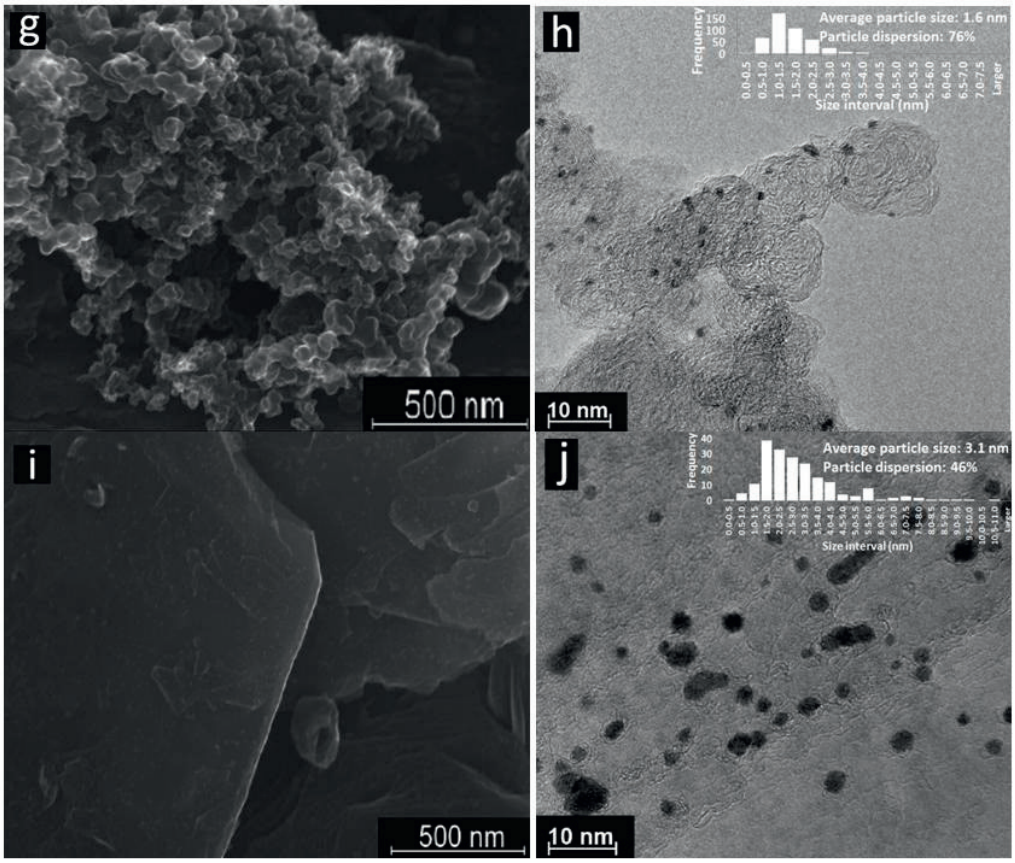

Figure 2 SEM images (left) and TEM images (right) of not-nanostructured catalysts with Pt particle size distributions presented in the upper right corner of the TEM images. g) and f): Pt/carbon black, i) and j): Pt/graphite.

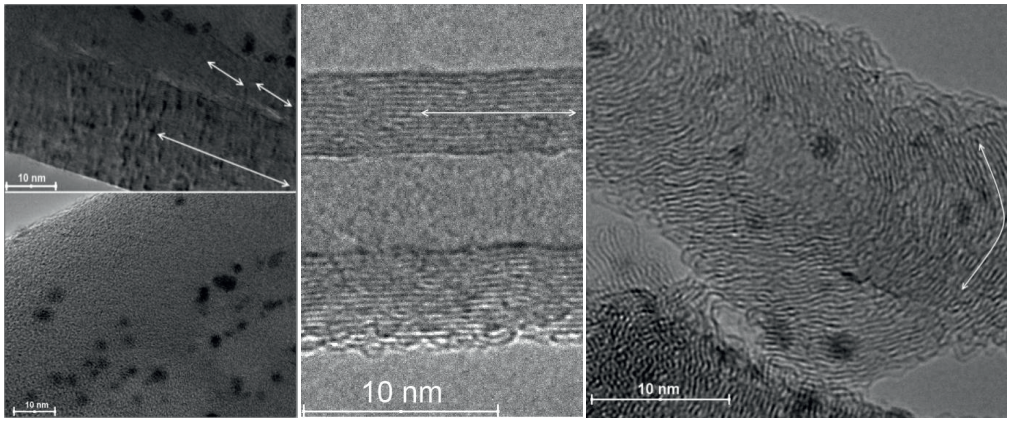

Fig. 3 TEM images showing the structure of Pt/CPCNF (left), Pt/MWCNT (middle) and Pt/PlCNF (right)

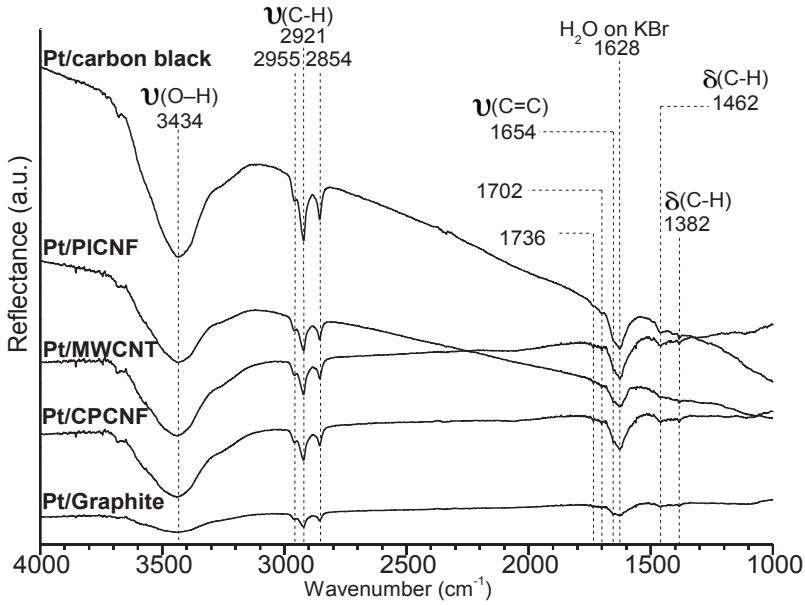

Fig. 4 FTIR spectra of catalysts. The reflectance axis has arbitrary units for each sample. Therefore the absorption peaks are for qualitative comparison. Letter υ denotes stretching modes and δ denotes in-plane bending modes

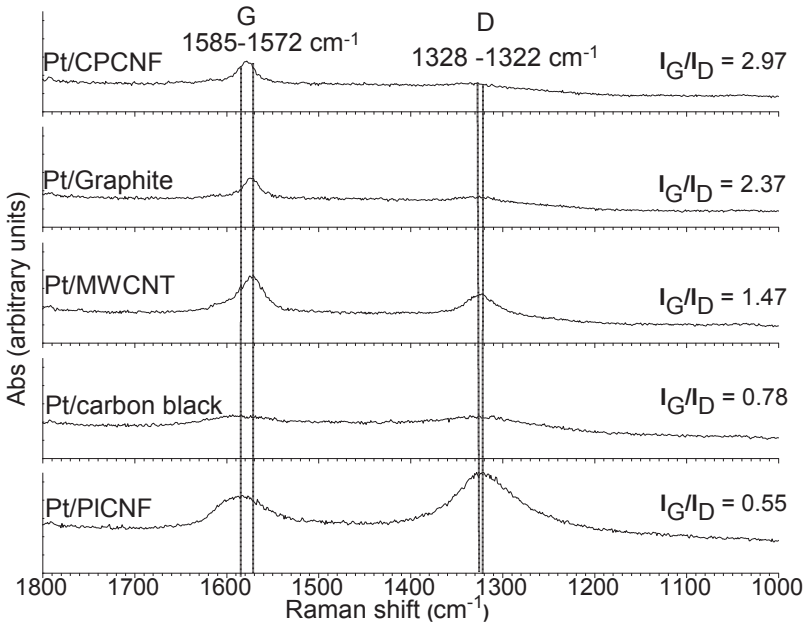

Fig. 5 Raman spectra of carbon supported catalysts.

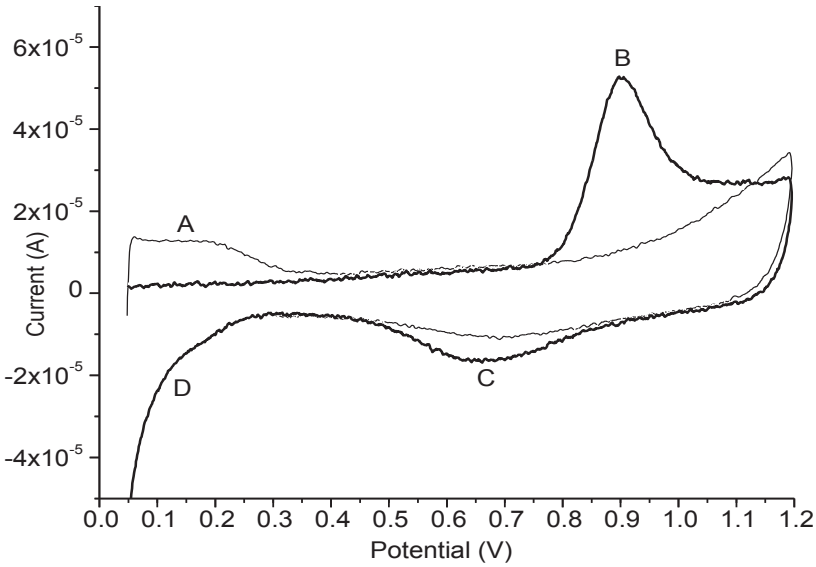

Fig. 6 Voltammogram for CO stripping of Pt/MWCNT. First stripping after CO adsorption (thick line) was done, then the second stripping (thin line) was done to obtain a voltammogram of CO-free catalyst. A is a region of H_2 desorption from platinum surface, B is a region of CO stripping, C is a region of Pt-O reduction, and D is a region of Pt-H formation

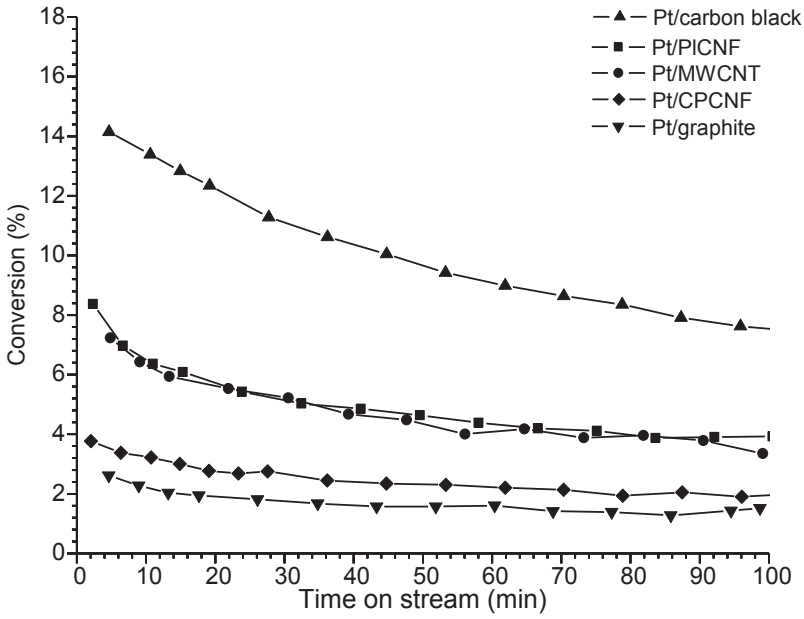

Fig. 7 Conversion results for propane dehydrogenation with 4.3% H_2 in the feed